NISTIR 4339

NEW NIST PUBLICATION
July 1990

RESEARCH FOR ELECTRIC ENERGY SYSTEMS - AN ANNUAL REPORT

R. J. Van Brunt, Editor

U.S. DEPARTMENT OF COMMERCE
National Institute of Standards
and Technology
Center for Electronics and Electrical
Engineering
Electricity Division
Gaithersburg, MD 20899

Prepared for
Department of Energy
Division of Electric Energy Systems
1000 Independence Avenue, SW
Washington, DC 20585

U.S. DEPARTMENT OF COMMERCE
Robert A. Mosbacher, Secretary
NATIONAL INSTITUTE OF STANDARDS
AND TECHNOLOGY
Dr. John W. Lyons, Director

NIST

NISTIR 4339

RESEARCH FOR ELECTRIC ENERGY SYSTEMS - AN ANNUAL REPORT

R. J. Van Brunt, Editor

U.S. DEPARTMENT OF COMMERCE
National Institute of Standards
and Technology
Center for Electronics and Electrical
Engineering
Electricity Division
Gaithersburg, MD 20899

Prepared for
Department of Energy
Division of Electric Energy Systems
1000 Independence Avenue, SW
Washington, DC 20585

December 1989

Issued June 1990

U.S. DEPARTMENT OF COMMERCE
Robert A. Mosbacher, Secretary
NATIONAL INSTITUTE OF STANDARDS
AND TECHNOLOGY
Dr. John W. Lyons, Director

Table of Contents

Foreword

This report summarizes the progress of four technical investigations conducted during CY 89. Although reasonable efforts have been made to ensure the reliability of the data presented, it must be emphasized that this is an interim progress report and that further experimentation and analysis may be performed before the conclusions from any of these investigations are formally published. It is therefore possible that some of the observations presented in this report will be modified, expanded, or clarified by our subsequent research.

Research for Electric Energy Systems – An Annual Report

R. J. Van Brunt, Editor

Abstract

This report documents the technical progress in the four investigations which make up the project "Support of Research Projects for Electrical Energy Systems", Department of Energy Task Order Number 137, funded by the U.S. Department of Energy and performed by the Electricity Division of the National Institute of Standards and Technology (NIST). The first investigation is concerned with an evaluation and critique of techniques for measurement of ambient magnetic fields in support of epidemiological and in vitro studies of biological field effects. General characteristics and theory of currently available measurement methods and instrumentation are reviewed. These include operation of air-core and magnetic-core coil probes. Procedures for use and calibration of these types of probes are recommended. Problems associated with the design of exposure facilities for in vitro studies of magnetic-field effects which use extremely low-frequency magnetic fields are discussed. Requirements for design of optimum experimental configurations are considered. The second investigation is concerned primarily with the decomposition of SF_6 in electrical discharges with emphasis on the chemistry of S_2F_{10}. The formation of S_2F_{10} in SF_6 is of particular concern because of its extremely high toxicity level. The mass spectrum of S_2F_{10} has been measured as a function of electron-impact energy and the problems associated with the use of mass spectrometry to detect trace levels of S_2F_{10} in gaseous SF_6 are revealed. A new method for S_2F_{10} detection which employs a gas chromatograph-mass spectrometer has been discovered which offers relatively high sensitivity for quantitative analysis of this species in SF_6 down to the sub-parts-per-million level. The new measurement method was employed to determine the rate of S_2F_{10} production in negative corona discharges operated at constant current in 200 kPa ($\sim$ 2 atm) SF_6. The results are found to be consistent with predictions of a chemical kinetics model of the discharge (discussed here) and indicate that S_2F_{10} can be produced from low-level discharges at a high rate. Surface catalyzed decomposition of S_2F_{10} has been observed to occur at room temperature on the walls of all types of gas sample cylinders, especially if they contain adsorbed H_2O. The effect of this surface chemistry on reliable sampling and quantitative analysis of SF_6 to determine S_2F_{10} content is discussed. The third investigation covered in this report is concerned with breakdown and prebreakdown phenomena in liquid dielectrics. Fast optical and electrical measurements have been made of microbubble formation associated with partial-discharge development around sharply pointed electrodes in n-hexane. Data from fast-frame photographs have been correlated with simultaneous partial discharge waveform data. The dynamical behavior of bubble formation and collapse at partial-discharge sites is revealed. Measurements were performed to quantify the statistics of breakdown streamers under uniform-field conditions in ultra-pure n-hexane. The morphological stages of anode streamer development are discussed. The results indicate electrode conditioning effects possibly due to polymerization of n-hexane breakdown products on the electrode surface during the breakdown process. The breakdown probability is found to depend on the occurrence, or lack thereof, of previous breakdown events, as well as on voltage waveform and particulate content of the liquid. The last investigation is concerned with the evaluation and improvement of methods for measuring fast transients in electrical power systems such as might be associated with an electromagnetic impulse. The focus of the activity reported here is on consideration of optical detector nonlinearities on the precision of electro-optical systems for measuring high-voltage impulses. The effect of these nonlinearities is clearly revealed in comparisons of calculated and measured Kerr cell responses for known impulse waveforms. The results of different measurements to test the degree of linearity in photomultiplier-tube response are reported. A “pulse-level-line” technique is introduced which gives greater precision than previously possible in peak voltage measurements using impulse voltage dividers and considerably reduces oscilloscope measurement uncertainties.

1 ELECTRIC FIELD MEASUREMENTS

Task 01
Martin Misakian
Electricity Division
National Institute of Standards and Technology

1.1 Introduction

The objectives of this project are to develop methods to evaluate and calibrate instruments which are used, or are being developed, to characterize the electrical parameters in the vicinity of power lines and in laboratory apparatus designed to simulate the power line environment. Electrical measurement support is also provided for Department of Energy-funded efforts to determine if there are biological effects due to ac fields and dc fields with ions.

The electrical parameters of interest include the electric field strength, magnetic flux density, ion current density, ion mobility, and ion species. Recent epidemiological studies have focused attention on the characterization of ambient power-frequency magnetic fields in homes. These ambient fields differ from fields near power lines in two important respects: (1) the magnitude of residential ambient fields can be much smaller than fields near power lines, and (2) ambient fields can contain significant levels of harmonics. Because of these and other differences, the existing IEEE/ANSI standard for measuring power frequency fields near power lines has certain shortcomings if used for guidance during measurements of residential magnetic fields. In this report, these shortcomings and methods for overcoming them are examined. A fuller account of this topic is provided in an IEEE Power Engineering Society working group paper that will be presented at the 1990 Summer Power Engineering Society Meeting [1]. Also examined in 1989 was the influence of geometrical design parameters on exposure conditions during in vitro studies using ELF magnetic fields. An optimum experimental configuration which can be used for many studies is briefly described in this report. A manuscript providing further details has been submitted to the journal Bioelectromagnetics [2]. Other NIST staff activities in 1989 included participation on advisory panels for the California Department of Health Services and the National Cancer Institute. Both panels are providing oversight for epidemiological studies that are considering the possibility of adverse health effects due to power frequency magnetic fields. A final working group draft standard for measuring dc electric fields and ion related parameters was prepared at NIST in collaboration with members of the DC Fields and Ions Working Group. As part of the approval process for the standard, NIST oversaw the successful balloting of the parent subcommittee, the Corona and Field Effects Subcommittee. NIST staff also participated in a magnetic field measurement field day at the Bonneville Power

Administration during which measurements with commercially available instruments were compared, made a site visit to the University of Rochester during which magnetic fields in biological exposure systems were characterized on behalf of DOE and EPRI, and presented two conference papers at the Sixth International Symposium on High Voltage Engineering.

1.2 Measurements of Ambient Magnetic Fields Away From Power Lines

Questions raised in the early 1970's regarding possible adverse environmental effects due to high-voltage ac transmission line fields [3–5] focused attention on the need for accurate measurements of power-frequency electric and magnetic fields near power lines. Due in part to these early concerns, an ANSI/IEEE standard which provides guidance for measuring 60-Hz electric and magnetic fields near power lines was developed by the late 1970's [6]. Recent epidemiological studies have focused attention on the characterization of ambient power-frequency magnetic fields in homes. These ambient fields differ from the fields near power lines in two important respects: (1) the magnitude of ambient fields is near 1×10^{-7} tesla [7], which is as much as two orders of magnitude smaller than the fields near some power lines, and (2) ambient fields can contain large percentages of harmonics, e.g., in excess of 30% [8]. In addition, while the geometry of power line magnetic fields is fairly well defined near the right-of-way, the geometry and magnitude of residential fields are typically more complicated and can depend on such factors as routing of distribution lines, number of local service drops, and type of ground return [7, 9].

The above remarks suggest that instrumentation used for characterizing ambient fields must have scales sensitive enough to measure fields of order 1×10^{-7} tesla and a frequency response that is appropriate for measuring the power-frequency harmonics. In addition, a calibration procedure that is not influenced by ambient magnetic fields should be used for the sensitive scales. The ANSI/IEEE standard noted above for measuring power line fields describes a calibration procedure using a coil system to produce a known field which is much larger than the ambient fields and therefore is not significantly perturbed by them. The standard also assumes that the harmonic content in the field is small, i.e., a few percent or less. Thus the standard has certain shortcomings if used as a guide for characterizing ambient magnetic fields. The purpose of this report is to provide information which can be used for some guidance during the measurement of ambient power-frequency magnetic fields. However, it is noted that measurement protocols for characterizing ambient magnetic fields are still under development. This report describes the instrumentation and calibration procedures that can be used for measurements in residential as well as occupational environments. Measurement techniques and examples of measurements in residential and occupational settings are provided in Reference [1].

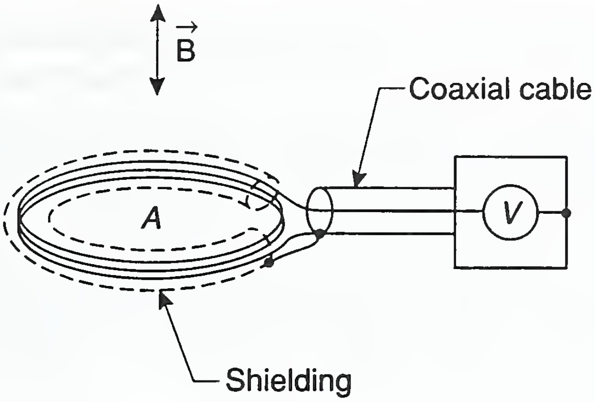

Figure 1. Schematic view of coil-type magnetic field meter used near power line.

1.2.1 *General Characteristics of Instrumentation*

Magnetic field meters used to measure power-frequency magnetic fields consist of two parts, the probe or field sensing element, and the detector which processes the signal from the probe. Magnetic field probes, consisting of electrically shielded coils of wire, have been used in combination with a voltmeter, as the detector, for survey type measurements of 60-Hz power line magnetic fields [6]. A schematic view of this kind of instrumentation, sometimes referred to as a survey meter, is shown in Figure 1. For measurements in a residential setting, where harmonic components in the magnetic field may not be negligible, an integrating amplifier is incorporated into the detector circuit in order to preserve the waveform of the magnetic field (see Section 1.3). During survey type measurements of the magnetic field, the probe can be held by hand without significant perturbation of the field due to the proximity of the observer. Proximity effects of nearby dielectrics and poor magnetic conductors are also insignificant. The rms field value is read from an analog or digital display. Typically, no provision is made for storage of data, although output connectors for commercially available recorders are sometimes provided.

For long term and more comprehensive measurement applications, the survey field meter can be replaced with a larger and sometimes less portable measurement system containing three orthogonally oriented coil probes for simultaneous, continuous, measurements of the three spatial components of the field, and a commercial data storage system which permits later analyses of the measurements [9]. It should be noted that in general, vectorially summing the rms values of the three orthogonal components will not yield the maximum value of the magnetic field because of phase differences between the spatial components. However, an upper limit to the maximum field value is provided by this summation. It is also interesting to note that the rms value of the total magnetic field is equal to the vector sum of the rms values of the spatial components [9].

The development in recent years of small magnetic field personal exposure meters, devices which can be worn to continuously measure and record the spatial components of magnetic flux density, has also led to the use of miniature coil probes containing ferromagnetic cores for increased sensitivity [10]. Other types of field meters with high permeability inductor probes, such as the fluxgate magnetometer [11], have been used for measuring low level dc magnetic fields in such applications as mineral prospecting and measurements in interplanetary space [12], but can be adapted for ac field measurements. It is noted, however, that the performance of fluxgate magnetometers, in the presence of ac and dc magnetic-fields of comparable magnitude, remains to be systematically tested.

Also available are magnetic field meters with Hall effect probes that can be used to measure magnetic flux densities from dc to several hundred hertz. However, Hall effect probes respond to the total magnetic field. Because of their low sensitivity and saturation problems due to the earth's magnetic field, they are not suited for residential or power line measurements. This report considers only instrumentation that employs pick-up coil probes, with and without magnetic cores.

To characterize the harmonic content in the magnetic field, the detector signal (which reflects the waveform of the magnetic field) can be examined using commercially available spectrum analyzers to obtain the amplitudes of the fundamental and harmonic components. An alternative approach, again using commercially available instrumentation, is to digitize the detector signal and use Fourier analyses to determine the amplitudes as well as phases of the fundamental and harmonic components.

1.2.2 Theory of Operation: Air Core Coil Probe

The principle of operation of the magnetic field meter shown in Figure 1 is based on Faraday's law which predicts that an electromotive force (emf) is produced at the ends of an open loop of wire placed in a changing magnetic field. Specifically, the emf is equal to the negative of the time-rate-of-change of the flux, Φ, through the loop,

$$\text{emf} = -d\Phi/dt = -d/dt[\int_A \vec{B} \cdot d\vec{A}], \tag{1}$$

where $\vec{B}$ is the magnetic flux density and $\vec{A}$ is a vector perpendicular to the plane of the loop. The magnitude of $\vec{A}$ equals the area of the loop. If the magnetic field is free of harmonics, e.g., $\vec{B} = \vec{B}_o \sin \omega t$, then

$$\text{emf} = -\omega B_o A \cos \omega t, \tag{2}$$

where ω is 2π times the frequency and it is assumed that $\vec{B}$ is perpendicular to the plane of the loop. For N turns of wire in the loop, the emf given by Eq. (2) will develop over each turn and the total emf will be $-N\omega B_o A\cos\omega t$. Eq. (2) shows that the sensitivity of the probe increases with cross-sectional area.

If there are harmonics in the field, there will be an additional term on the right side of Eq. (2) for each harmonic. Because of the differentiation operation in Eq. (1), each of the additional terms will be weighted by an associated harmonic number. For example, if there was 10% third harmonic in the field, the term, $-3 \times (0.1)\omega B_o A\cos 3\omega t$, would be added to the right side of Eq. (2). Because of the weighting of the harmonic term, the waveform of the signal will no longer reflect the waveform of the field. Consequently, the rms value indicated by the voltmeter-detector (Figure 1) will not accurately represent the rms value of the field. The waveform does reflect, to a good approximation, the voltage or current induced in some biological systems.

To recover the magnetic field waveform, it is necessary for the detector to perform the inverse mathematical operation, namely integration. This can be accomplished by introducing an integration stage in the detector. For example an integrating amplifier combined with a voltmeter could be used as the detector. The frequency response of the probe-integrating amplifier combination can be made flat for the power-frequency harmonics. It should be noted that this "corrective" action provided by the detector is essential to obtaining accurate rms values of the magnetic field as well as correct percentages of harmonics.

Neglected in the discussion so far is the frequency response of the probe. Because of the inherent inductance, resistance and capacitance of the probe, the relationship between the emf produced in the coil [Eq. (2)] and the voltage entering the detector should be considered as a function of frequency. A schematic view of the equivalent circuit for the coil probe is shown in Figure 2. The ratio, $|A|$, of probe voltage, v_p, to emf is given by [13]

$$|A| = |v_p/\text{emf}| = \{[(R+r)/R - \omega^2 LC]^2 + [\omega(L/R + Cr)]^2\}^{-1/2} \tag{3}$$

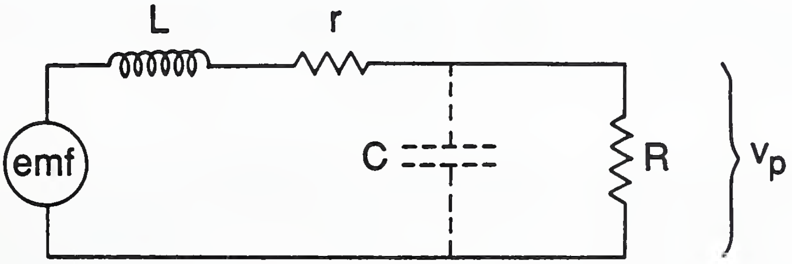

Figure 2. Equivalent circuit of coil-type magnetic field probe. R is the approximate input impedance of the detector.

where L and r are the inductance and resistance of the coil and its leads, C is the stray capacitance, and R is the approximate input impedance of the detector.

The value of $|A|$ should remain close to unity and not peak before falling off with increasing frequency. Higher values of R cause peaking and a sharp fall-off in $|A|$, a possible cause of oscillation in some circumstances. Lower values of R permit the value of $|A|$ to roll off gently with increasing frequency. Too low a value, however, causes unnecessary reduction in frequency response [8]. Examples of plots using Eq. (3) for a coil probe and for different values of R are shown in Reference [8].

In the above discussion, it is assumed that the induced current in the coil probe, after it is connected to the detector, is sufficiently small that the opposing magnetic field produced by it is negligible.

Yet another consideration in the design of a detector is whether the detector indicates an "average rms" or true rms value of the field. If there are harmonics in the magnetic field, an average-sensing rms detector will be in error, the magnitude of which will depend in part on the magnitude and phase relations of the harmonics to the fundamental [6, 14] (see Section 1.2.4).

To minimize fluctuations of the field meter reading on the more sensitive scales due to movement of the probe in the earth's magnetic field, a low frequency cut-off (i.e., $\lesssim 40\,\mathrm{Hz}$) can be incorporated into the detector circuit. However, such a feature could prevent accurate measurements of magnetic fields due to some electrical equipment which operate at lower frequencies, e.g., electric streetcars.

Another option which is available for characterizing a magnetic field containing harmonics is to use a measurement system consisting of a detector without an integrating stage. The detector, however, is combined with instrumentation to digitize the signal waveform (which is proportional to the derivative of the magnetic field). By using Fourier analysis, the amplitude-enhanced harmonic components can be determined, and by dividing the harmonic component amplitudes by the harmonic number (using computer software), the correct harmonic percentages and their phase relations can be determined. This measurement approach allows for the recovery of higher order harmonics (e.g., > 9th harmonic) which may be lost, due to signal-to-noise problems, using an integrating amplifier.

1.2.3 Theory of Operation: Magnetic-Core Coil Probe

As noted earlier, the use of miniature coil probes in exposure meters has led to the use of cylindrical ferromagnetic cores to increase the flux density through the coil, thereby increasing the sensitivity of the probe. The emf from the coil is still predicted by Faraday's law. Further, the discussion in Section 1.3 regarding the use of an integrating amplifier and probe frequency response is again applicable. In this section, the influence of the core permeability and core shape on probe characteristics

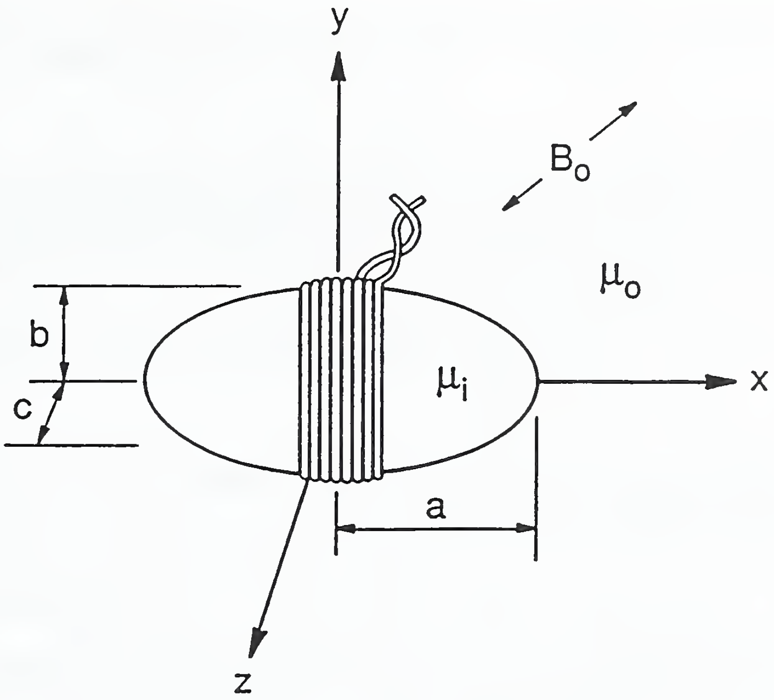

Figure 3. Geometry for coil-type probe with prolate ellipsoidal core of magnetic material. For clarity, the electrical shielding for the coil is not shown.

are examined briefly. For purposes of discussion, the coil probe with a cylindrical core in a uniform power-frequency magnetic field, $\vec{B}_o$, is simulated by replacing the cylinder with a prolate ellipsoid as shown in Figure 3. While, unlike the cylinder, use of an ellipsoid leads to a uniform B field inside the core, the general conclusions indicated below are still valid.

Expressions for the components of the magnetic flux density inside a prolate ellipsoid can be derived from an expression for the magnetic potential provided by Stratton [15]. The magnetic field components in Cartesian coordinates are

$$B_{xi} = B_{ox}/[\alpha + \beta(1-\alpha)A_1], \tag{4}$$

$$B_{yi} = B_{oy}/[\alpha + \beta(1-\alpha)A_2], \tag{5}$$

$$B_{zi} = B_{oz}/[\alpha + \beta(1-\alpha)A_3], \tag{6}$$

where $\alpha = \mu_o/\mu_i, \mu_o$ is the permeability of vacuum, μ_i is the initial permeability of the core, $\beta = abc/2$, a is the semi-major axis of the prolate ellipsoid, b and c are equal and are the semi-minor axes. A_1, A_2 and A_3 are elliptic integrals of the second kind and are given by

$$A_1 = \int_o^\infty ds/(s+a^2)[(s+a^2)(s+b^2)(s+c^2)]^{1/2}, \tag{7}$$

$$A_2 = \int_o^\infty ds/(s+b^2)[(s+a^2)(s+b^2)(s+c^2)]^{1/2}, \tag{8}$$

and

$$A_3 = \int_0^\infty ds/(s+c^2)[(s+a^2)(s+b^2)s+c^2)]^{1/2} = A_2. \tag{9}$$

The sinusoidal time dependance of the magnetic field in Eqs. (4)–(6) has been suppressed. As anticipated, Eqs. (4)–(6) show that the magnetic field in the ellipsoid is uniform, and in addition, generally not in the same direction as the external field. It is readily shown that as the ellipsoid is rotated in space, the flux density along the major axis, B_{xi}, obeys the cosine law.

From Eqs. (4)–(6), the following observations, which may have relevance when designing a probe, can be made:

> For a given core geometry, the flux density through the core and coil increases with permeability, as expected.
>
> As the ratio $a : b$ increases, the flux density along the major axis and through the coil increases for constant permeability. As the ratio $a : b$ decreases, the flux density along the major axis and through the coil becomes less sensitive to changes in permeability. For example, with μ_i equal to $250\,\mu_\circ$ and $a : b$ equal to 4, a decrease in μ_i of 10 % results in a decrease in flux density along the major axis of 0.52 %. If $a : b$ were equal to 8, the corresponding decrease in flux density would be 1.34 %.
>
> For a given core geometry, changes in large values of permeability have proportionately less effect on the flux density along the major axis and through the coil than changes in low values of permeability.
>
> For a spherical core, $a = b = c$ and $A_1 = A_2 = A_3$, the field in the core will be parallel to the external field and is given by
>
> $$B_i = 3B_\circ/[1 + (2\mu_\circ/\mu_i)]. \tag{10}$$

Eqs. (4)–(10) have been derived assuming that the ellipsoid material is isotropic, homogeneous, free of residual magnetism and has a constant permeability. These assumptions are approximately satisfied by soft magnetic materials near room temperature in ambient fields, with normal handling. However, the following general information should be remembered when core materials are considered.

> The core material should have a low coercive field to minimize the possibility of permanently magnetizing the core and changing the permeability if exposed to strong magnetic fields, i.e., the material should be magnetically soft.
>
> Vibrations and the mechanical shock of dropping the core material can change the boundaries of magnetic domains and decrease the permeability, particularly if the initial permeability is high.

For sheet and strip material, the permeability decreases as the inverse-square-root ($f^{-1/2}$) above a critical frequency, f_c. For **sheet** material, f_c is given by [16]

$$f_c = 4\rho/\pi\mu_i D^2 \tag{11}$$

where ρ is the resistivity, μ_i is the initial permeability (i.e. the permeability at very low magnetic field strength) and D is the thickness of the sheet. The apparent decrease in permeability is due to opposing fields in the material caused by eddy currents. Thus, while high initial permeability is desirable for increasing the probe sensitivity, it reduces the value of f_c. Because of their high resistivities, ferrites can have very high values for f_c.

The initial permeability depends on many factors including chemical composition as well as mechanical and thermal treatment. For example, adding a few percent of silicon to soft iron increases the permeability, decreases the coercive field, increases the resistivity and improves the stability of the magnetic characteristics [17].

The permeability of magnetic materials varies with temperature and the temperature coefficient depends on magnetic field strength as well as type of magnetic material [18].

The interested reader is encouraged to read texts by Heck [16] and Bozorth [19] for more in-depth discussions of the properties of magnetic materials. Tables indicating trade names of magnetic materials and manufacturers in the U.S., Europe, and Japan are given in reference [16].

1.2.4 Calibration

The recommended procedure for calibrating magnetic field meters used near ac power lines is to introduce the probe into a nearly uniform magnetic field of known magnitude and direction [6]. Helmholtz coils have frequently been employed to generate such fields but the more simply constructed single loop of many turns of wire with rectangular geometry can also be used. The simplicity in construction is at the expense of reduced uniformity, but sufficient accuracy is readily obtained for single probes used with survey meters [20]. The uniformity of the field in the central volume of a 1 m × 1 m loop is described in References [6] and [20], and is normally adequate for probes with diameters less than 10 cm. Therefore, the existing recommended procedures can be used for calibrating the higher ranges (i.e., $\sim 0.1\times10^{-4}$ to 1×10^{-4} tesla) of survey meters which are to be used for measuring ambient fields.

By varying the frequency of the current through the loop, the frequency response of the field meter can be determined for the power-frequency harmonics. For nearly constant $|A|$ [Eq.(3)] and a suitably designed integrating amplifier, a field meter with an air core probe should indicate a nearly constant rms value as the frequency is varied. A similar result should be obtained with a probe that contains a core of soft ferromagnetic material, if the change in permeability as a function of frequency is negligible. It is noted that while a flat frequency response may be observed with average-sensing rms detectors and true rms detectors, the response of the average sensing rms detector to a complex magnetic field waveform consisting of the fundamental and one or more harmonics may still be in error [14].

Establishing a known magnetic field for calibrating the more sensitive scales (i.e., $\sim 0.10 \times 10^{-7}$ to 0.1×10^{-4} tesla) is made difficult by the presence of ambient fields of order 1×10^{-7} tesla. This problem can be overcome by using an alternative calibration technique, that of voltage injection. From Eqs. (2) and (3), it is seen that, the probe voltage, v_p, is a linear function of B, for constant $|A|$ using an air core probe. Therefore, the ratio $v_p : B$ can be determined with a known B-field at field levels not significantly affected by ambient fields, and known voltages at frequencies of interest can be injected into the detector to calibrate the more sensitive scales. The ratio $v_p : B$ is determined with the probe connected to the detector. A voltage divider can be used to produce the typically small voltages necessary to calibrate the more sensitive scales. Adequate electric field shielding should be provided when calibrating the sensitive scales. The voltage injection technique can be used with probes containing soft ferromagnetic cores assuming the change in permeability as a function of flux density is negligible. Some materials with constant permeabilities at low field values are identified in Reference [16]. Further details of the voltage injection calibration technique can be found in Reference [8].

Air core probes in large measurement systems with more than one probe can be calibrated individually following the procedures for survey meters. This assumes that the electronic circuits associated with the detectors and data storage do not generate significant levels of noise which can be sensed by the detectors, particularly on the more sensitive scales.

If the probes contain magnetic cores and are in close proximity, as in the case of some miniaturized exposure meters, the field sensed by one probe may be significantly perturbed by the core material of an adjacent probe. Therefore, when the higher scales are calibrated with a known field to determine the ratio $v_p : B$, the entire instrument, appropriately aligned, should be placed in the field as each probe and associated detector is calibrated.

The close proximity of the probe, detector, and data storage circuits can make the problem of electrical noise pick-up more serious in small exposure meters than in larger measurement systems. The electrical noise can create a “noise floor” which prevents magnetic field measurements below a certain level. The minimum detectable field can be estimated by comparing measurements obtained with an exposure meter and a survey meter at locations where the ambient fields are unusually low. A more efficient approach would be to establish a very low ac magnetic field environment using magnetic shielding and make comparative measurements in this "zero" field. Reconfiguring circuit elements and adding magnetic shielding to circuit boards are possible steps to minimize the coupling of electrical noise to the probes as well as detector circuits.

1.2.5 Measurement Techniques In Different Environments

As noted earlier, there are no established protocols at this time for characterizing ambient magnetic fields in environments away from power lines. The more comprehensive the measurement goals are away from the power lines, however, the greater will be the measurement requirements. For example, the amount of information provided by a spot measurement of the rms value of the magnetic field at one location in a residential or occupational setting is rather limited. No information is gained regarding the temporal variation of the magnetic field over periods of a day, a week, or across seasons. No information is obtained regarding the harmonic content in the magnetic field. The spatial variation of the field in the vicinity of the measurement point is also unknown and difficult to predict.

The goals of magnetic field measurements can be divided into two catagories, one that focuses on personal exposure and one that focuses on source characterization. Measurement techniques associated with each goal as well as examples of measurements are described in Reference [1].

1.3 An Optimum Design For In Vitro Studies Using ELF Magnetic Fields

There have been many laboratory studies since the mid 1970's examining the possibility of biological effects to cells in vitro due to extremely low frequency (ELF) magnetic fields. These studies typically have used Helmholtz coils to generate approximately uniform magnetic fields for exposure purposes. Significantly, the enclosures containing the cells and liquid growth medium have varied in shape and size. While the magnetic field will be uniform throughout the liquid, regardless of the shape and size of the enclosure, the same cannot be said for the electric fields and associated currents that are induced in the liquid as a result of the time-varying magnetic field. In general, the magnitudes (and directions) of the induced current and electric field that the cells experience will depend on their location in the liquid. In addition, the complexity of the equations that predict the values of the induced electric field and current at a point in the liquid will depend on the shape of the liquid volume and the direction of the magnetic field. If an attempt is made to replicate the results of an earlier in vitro study employing ELF magnetic fields, and there exist differences in the geometry, i.e., differences in shape or size of the liquid volume, or direction of the magnetic field relative to the volume of liquid, the exposure conditions could be significantly different even if the magnetic field has the same frequency and magnitude. Expressed more simply, a true replication of the earlier experiment would not have been performed. Some of the above observations have been made previously or are implied in the paper by McLeod et al. [21].

What is described here is a geometry and enclosure shape which can be adapted for many in vitro studies employing uniform, single phase ELF magnetic fields (the direction and magnitude of any dc magnetic field, whether ambient or applied, may be of significance if tests of a resonance model are being conducted; such models are not considered here). The experimental arrangement consists of one or more enclosures, cylindrical in shape, and oriented with the cylinder axis parallel to the ELF magnetic field. This arrangement can simplify the interpretation of experiments and optimize the amount of information regarding the degree of exposure that cells experience due to the magnetic field and due to the current and electric field induced in the liquid growth medium by the magnetic field. It is acknowledged, however, that because of the multitude of parameters associated with in vitro studies with cells, it may not be practical in some instances to implement the experimental design being advanced here.

The exposure geometry and the design of an enclosure that would be suitable for short term studies with cells in suspension are shown in Figure 4. The cylindrical enclosure, which can be made of plastic or glass, has circular walls that partition the cylindrical volume into several sections. As indicated above, the axis of the enclosure is aligned with the magnetic field. While the cylindrical volume in Figure 4, has been partitioned into three sections, more or fewer sections could be used. A glass version of the enclosure can be readily fabricated by a glass blower. For more extended periods of exposure, lasting as long as six or seven days, the enclosure can be fitted with a cap and "sealed" with commercially available laboratory film which prevents significant evaporation but allows adequate air exchange [22].

Exposure studies with cells that are cultured in agar may be possible by introducing a layer of agar at the bottom of the enclosure as shown in Figure 4. If a layer of agar is used, it is desirable that its electrical conductivity be approximately equal to that of the liquid medium so that the two media are electrically equivalent. The agar provides for a more quantifiable exposure of the cells (top and underside) to the induced currents and electric fields compared with the exposure of cells in contact with glass or plastic.

However, researchers should note that the use of agar may have unforeseen biological consequences in some cases, as demonstrated by a recent study by Cohen et al. [23] which showed increased "...frequency of chromosome breakage, sister-chromatid exchange and decreased cloning efficiency..." for cells cultured in agar as compared to cells grown on a plastic substrate.

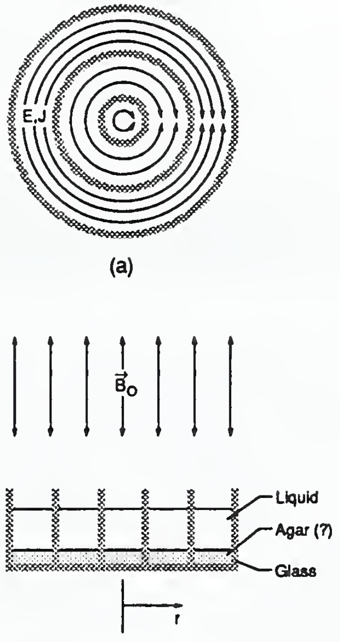

(a)

(b)

Figure 4. Geometry of uniform magnetic field-cell enclosure combination (a) top view. Directions of E and J are schematically indicated (b) cross sectional view of enclosure containing agar and liquid medium. The use of agar is discussed in the text. For short term studies with cells in suspension, circular walls partition enclosure into regions of different exposure conditions.

If the circular walls shown in Figure 4 introduce an impediment for cells plated directly on the (plastic/glass) enclosure floor, the walls can be replaced with painted concentric circles on the underside of the enclosure floor. Other techniques for characterizing the radial positions of the cells in the cylindrical enclosure include growing the cells on a glass cover slip placed in the enclosure (the cover slip can be removed later for measurements with a compass and rule) or indicating the annular regions on a flat surface upon which the enclosure is placed. Vertical stacking of the enclosures is one approach for increasing the number of cells that are exposed during an experimental run. The motivation for characterizing the radial positions of the cells during exposure to ELF magnetic fields is made clear below.

The directions of the induced current and electric field in the recommended experimental arrangement are circular, as schematically indicated in Figure 4a. For a sinusoidal ELF magnetic field, $B_p \sin \omega t$, where B_p is the peak value of the magnetic field and ω is 2π times the frequency, f, the magnitudes of the peak current density and associated electric field can be written simply as [2, 21]

$$J_p = \sigma \pi f B_p r \tag{12}$$

and

$$E_p = \pi f B_p r \tag{13}$$

where σ is the conductivity of the liquid and r is the radial distance from the cylinder axis. It is noted that the root-mean-square (rms) values of J and E can be found from Eqs. (12) and (13) by replacing B_p with its rms value, i.e., $B_p/\sqrt{2}$. It is also noteworthy that J_p and E_p are independent of the liquid or agar depth.

Eqs. (12) and (13) show that the induced current density and electric field vanish on the cylinder axis and increase linearly to their maximum values along the outer perimeter of the cylindrical enclosure. The range of current density and electric field values in a circular section is determined from Eqs. (12) and (13), and the radii that define the section. As noted earlier, the magnetic field is essentially uniform throughout the liquid volume. Thus, cells placed in different circular regions of the enclosure will be exposed to different but quantifiable levels of electric field and current density. At the same time, all of the cells will be exposed to the same level of magnetic field.

The geometry and cylindrical enclosure design described above are being suggested as an optimum experimental configuration because the direction and spatial dependence of B_p, J, and E are readily visualized, the equations for calculating J and E are very simple and independent of liquid depth, the amount of information pertaining to dose-response during a single experimental run can be maximized, and the suggested configuration allows one to distinguish between a magnetic field bioeffect and a bioeffect that involves the electric field or electric field-magnetic field combination. Further, *when possible*, use of a common experimental configuration by researchers would also be helpful when attempts are made to replicate the results of bioeffects studies in different laboratories.

2 GASEOUS DIELECTRICS RESEARCH

Task 02

Richard J. Van Brunt and James K. Olthoff
Electricity Division

John T. Herron
Chemical Kinetics Division
National Institute of Standards and Technology

2.1 Introduction

The objectives of this project are the development of measurement capabilities and the providing of fundamental data as part of the Department of Energy's basic research concerned with the development and evaluation of advanced compressed-gas-insulation technology.

To reduce space requirements and improve the efficiency of high-voltage transmission systems, the electric power industry has turned toward more extensive use of compressed-gas insulation. To design meaningful tests of system performance and establish specifications for the quality of materials used in such systems, more information is needed about the fundamental physical and chemical processes which lead to insulation deterioration and electrical breakdown. The research includes applications of gas chromatography-mass spectrometry to characterize corona discharge by-products; and the acquisition of fundamental data, such as, reaction-rate coefficients, corona-inception voltages, production rates of corona by-products, the effects of contaminants on discharge initiation, and the rates of discharge-induced decomposition of the gas.

This report highlights work conducted at NIST during the past year on the detection and production of disulfur decafluoride (S_2F_{10}) in SF_6. Some of this work was carried out in collaboration with scientists at the Oak Ridge National Laboratory and selected results have already been reported in one archival [24] and three conference papers [25–27].

The production of S_2F_{10} in SF_6 during electrical discharges is of concern because of its known high level of toxicity [28, 29]. The ceiling limit for human exposure is recommended by the American Conference of Governmental and Industrial Hygienists [30] to be 10 parts per billion, making this chemical 300 times more toxic than other known gaseous by-products of SF_6 decomposition in electrical discharges [28, 31]. There are previous reports of S_2F_{10} formation under various electrical discharge conditions which include spark [32–35], corona [33] and arc [36, 37] discharges. Much of this earlier work, however, only yielded qualitative results, i.e.,

S_2F_{10} was simply identified as a discharge by-product and no information was given about its absolute concentration or production rate. This is especially true in the case of S_2F_{10} production from corona discharges [33].

This report includes not only results on absolute S_2F_{10} yields from negative corona discharges in SF_6, but also discusses the problems associated with making a reliable quantitative analysis of SF_6 to determine the absolute concentration of S_2F_{10} at low levels. A new sensitive technique for direct analysis of SF_6 for S_2F_{10} content is introduced and problems of S_2F_{10} decomposition on surfaces at room temperature in reference sample cyclinders is discussed. The experimental results on S_2F_{10} production from corona discharges are compared with predictions from a chemical kinetics model of the discharge.

2.2 Detection Methods

In this section we consider first the problems associated with using a mass-spectrometer equipped with an electron-impact ion source to detect S_2F_{10} in the presence of SF_6. Results are presented on the electron-impact energy dependence of the S_2F_{10} positive-ion mass spectrum. We then discuss a new method employing a gas chromatograph-mass spectrometer (GC/MS) with a membrane separator that offers relatively high sensitivity for SF_6 detection. Our results on the S_2F_{10} mass spectrum are also covered in Ref. [24], and the GC/MS method of analysis is briefly discussed in Ref's [25] and [27].

2.2.1 Detection of S_2F_{10} Using Mass Spectrometry

Evidence was presented in a recent paper by Farber and coworkers [38] for formation of the ions $S_2F_{10}^+$ and $S_2F_9^+$ from direct electron-impact ionization of S_2F_{10} at an electron energy of 20 eV in a mass spectrometer. If these ions are indeed derived from S_2F_{10}, then this offers the possibility of using mass spectrometry for sensitive detection of S_2F_{10} in SF_6, since these ions do not appear in the mass spectrum for SF_6. The gas samples used by these authors were prepared by subjecting SF_6 to an electrical discharge in which the S_2F_{10} was presumed to be formed. Other than the appearance of ions at mass-to-charge ratios (m/e) of 254 and 235, which were surmised to be formed from S_2F_{10}, there was no other evidence presented for the presence of S_2F_{10}. No corresponding tests were reported using reference gas samples known to contain S_2F_{10}.

In the present work, mass spectrometric measurements were performed using gas samples known to contain 1500 ppm_v of S_2F_{10} in either Ar or N_2 buffer gas. The gas mixtures were prepared using pure S_2F_{10} as previously discussed [39]. The mass spectra were measured using a differentially pumped rf-quadrupole mass spectrometer

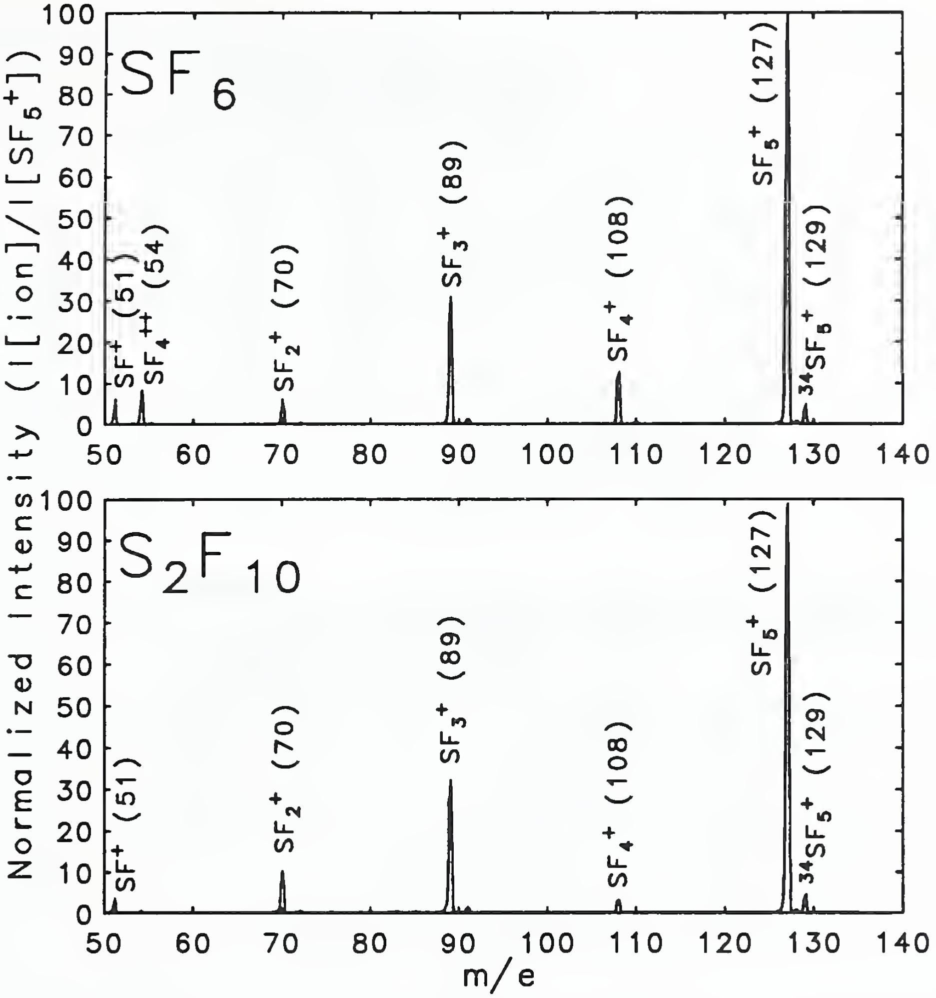

Figure 5. Observed mass spectra of SF_6 and S_2F_{10} at an electron-impact energy of 70 eV.

with a mass range from m/e = 2 to m/e = 2000. The instrument was equipped with an electron-impact ionizer which allowed electron energies from 11 to 70 eV to be selected with an estimated energy spread between 1 and 2 eV. The electron energy scale was calibrated by the previously established method [40] using the ionization potential for Ar of 15.76 eV.

Examples of mass spectra obtained from SF_6 and S_2F_{10} at 70 eV are shown in Figure 5 for m/e $\geq$ 50. The corresponding relative abundances of the different ions from these molecules at 70 eV are given in Table 1 in comparison with the "standard" SF_6 mass spectrum [41] and with results previously published by Cohen and MacDiarmid [42] for S_2F_{10}. These abundances are expressed in percent as obtained by computing areas under the peaks shown in Figure 5 and normalizing to the peak area for the most abundant ion, namely SF_5^+ at m/e = 127. The relative abundances obtained from the present measurements are seen to be in acceptable agreement with those

Table 1. Percent relative abundances of ions from SF_6 and S_2F_{10} at 70 eV for $m/e \geq 51$

		Relative abundances (percent)			
		SF_6		S_2F_{10}	
Ion	m/e	a	b	a	c
SF_5^+	127	100	100	100	100
SF_4^+	108	12.4	8.9	3.3	<3.1
SF_3^+	89	30.7	26.3	33.0	36.0
SF_2^+	70	5.2	5.3	10.3	14.0
SF_4^{++}	54	6.7	7.4	0.4	<3.1
SF^+	51	5.2	7.6	2.6	5.9

a–present work
b–Cornu and Massot
c–Cohen and MacDiarmid

Table 2. Ratios of relative S_2F_{10} peak intensities to corresponding relative SF_6 peak intensities at different electron-impact energies (20 eV to 70 eV)

		$I(\text{ion}, S_2F_{10})/I(\text{ion}, SF_6)$			
Ion	m/e	70 eV	50 eV	35 eV	20 eV
SF_5^+	127	1.0	1.0	1.0	1.0
SF_4^+	108	0.27	0.29	0.28	0.70
SF_3^+	89	1.09	1.12	1.09	57.0
SF_2^+	70	1.99	1.75	2.34	26.0
SF_4^{++}	54	0.05	0.05	*	*
SF^+	51	0.50	0.45	1.92	*

*–ion not present for one or both species.

previously published. The differences are undoubtedly due in part to differences in relative mass discrimination associated with the different instruments used. For the quadrupole mass spectrometer used in this work, the relative mass discrimination depended significantly on the operating conditions which were not always adjusted to minimize discrimination over the mass range of interest. Consistent with previous work [41, 42], no ions from either SF_6 or S_2F_{10} were observed above $m/e = 129$ corresponding to $^{34}SF_5^+$.

Table 2 shows ratios of relative S_2F_{10} ion fragment intensities to corresponding SF_6 ion fragment intensities, e.g., $I(SF_3^+, S_2F_{10})/I(SF_3^+, SF_6)$, where the numerator and denominator are respectively the normalized SF_3^+ peak areas from the S_2F_{10} and SF_6 spectra at the same electron energy. The ratio $I(SF_5^+, S_2F_{10})/I(SF_5^+, SF_6)$ is always equal to 1.0 because the SF_5^+ peak is always the largest peak in both spectra. These ratios were found to be insensitive to relative mass discrimination associated with different operating conditions for the instrument, and give a quantitative indication of the extent to which the mass spectra for these two molecules differ.

The data shown in Figure 5 and Tables 1–2 indicate that at 70 eV the mass spectra of SF_6 and S_2F_{10} are quite similar. With the possible exception of SF_4^{++} at m/e = 54, all of the significant ion peaks that appear in the SF_6 spectrum also appear in the S_2F_{10} spectrum. However, at lower electron energies, particularly at 20 eV, the mass spectra of these two species exhibit considerable differences. In particular, the relative intensities of the SF_3^+ and SF_2^+ ions in the S_2F_{10} spectrum are seen to be much higher than the corresponding relative intensities of these ions in the SF_6 spectrum at 20 eV. This is due in part to the fact that the appearance potentials of these ions are significantly lower for S_2F_{10} than for SF_6.

The appearance potentials for the ions SF_5^+ and SF_3^+ from S_2F_{10} were measured by the usual method [40, 43] and found to be 13.2 and 13.3 eV, respectively. The corresponding appearance potential values for these ions from SF_6 were found to be 15.7 and 19.7 eV, respectively, in favorable agreement with values previously reported [44].

There was no evidence for formation of either $S_2F_{10}^+$ or $S_2F_9^+$ at electron energies in the range of 11 to 70 eV and for ion source pressures from 1×10^{-6} torr to 8×10^{-5} torr. From a consideration of the measured detection sensitivity, we estimate that the maximum allowable relative abundance, $I(\text{ion})/I(SF_5^+)$, for the ions at masses 254 and 235 to be about 0.07%. To insure that ions at these masses could have been observed, the instrument response was checked up to m/e = 502 using perfluorotributylamine [45]. The present observations, therefore, do not lend support to the assignment of S_2F_{10} to the observed peaks at m/e = 254 and m/e = 235 made by Farber and co-workers [38] from their analysis of SF_6 decomposed in an arc discharge. It should be noted that the arc discharge cell which they used was made of a polymeric material (Teflon) [48]. There is evidence from the measurements of Gilbert and co-workers [46] that polymers can significantly degrade when exposed to electrical discharges in SF_6 giving rise to volatile compounds of relatively large mass such as $CF_3\text{-}S_x\text{-}CF_3$, $x \geq 2$. It is conceivable that the high-mass ions reported by Farber and coworkers are associated with molecular species resulting from polymer degradation. Certainly the ion intensity ratio of m/e = 254 to m/e = 256, apparent from the data of Farber and coworkers (their Figure 1), is not in agreement with the known ^{34}S to ^{32}S isotope abundance ratio of 0.0443. Since the correct isotope ratio was not obtained, this suggests that the observed ions were not derived from the same sulfur-containing compound.

The present results demonstrate that $S_2F_{10}^+$ and $S_2F_9^+$ ions are not likely to be formed from S_2F_{10} and therefore cannot be used as indicators for the presence of this species in SF_6 using electron-impact mass spectrometry. It is clear from the similarity of the SF_6 and S_2F_{10} mass spectra at 70 eV that it would be very difficult to unambiguously detect the presence of small quantities of S_2F_{10} in SF_6 using a mass spectrometer operated at this energy. Because of the rather large differences in appearance potentials for the ions SF_5^+, SF_3^+, and SF_2^+ observed from SF_6 and S_2F_{10}, it may be possible to use a lower electron-impact energy (20 eV or lower) to detect

S_2F_{10} in SF_6. However, the level of detection sensitivity by this method is yet to be determined.

2.2.2 GC/MS Method of Detection

As discussed in the next section, experimental evidence has been obtained indicating that S_2F_{10} reacts on surfaces containing adsorbed H_2O to form gaseous SOF_2, SF_6, and HF. Under some conditions the reaction can be quite rapid even at room temperature (~ 20 °C). This same process was found to occur in a heated inlet tube between the gas chromatograph and mass spectrometer of the GC/MS instrument used for S_2F_{10} detection. During analysis of S_2F_{10} samples, this decomposition causes features to appear in the GC/MS chromatograms at retention times corresponding to S_2F_{10} molecules but at ion masses corresponding to the molecular decomposition products SOF_2 and HF. Figure 6 shows these features at several different ion masses for a 400 ppm_v S_2F_{10} sample in argon.

The SO^+ and SOF_2^+ ions are the result of electron-impact ionization of SOF_2 in the mass spectrometer, and the mass 20 signal is likely due to the ionization of HF. The fact that the signal occurs at retention times corresponding to S_2F_{10} indicates that the conversion takes place after the S_2F_{10} elutes from the GC column. The mass 127 ions can be due to ionization of either S_2F_{10} or SF_6 while the F^+ ions may be formed by the ionization of any of the product molecules. The fact that ions 19 and 127 may be produced from either S_2F_{10} or the conversion products, makes it difficult to estimate the conversion efficiency at this time.

Because S_2F_{10} and SF_6 have nearly identical mass spectra [13], the GC/MS technique is normally not very sensitive when $[SF_6] >> [S_2F_{10}]$. Even though SF_6 and S_2F_{10} have significantly different retention times (typically more than 1 minute), the tail of the extremely large SF_6 signal completely obscures the much smaller S_2F_{10} signal at concentrations much below 50 ppm_v. This is illustrated by the mass 19 data in Figure 7.

The conversion of S_2F_{10} into SOF_2 on the surface of the heated mass spectrometer inlet tube provides a means of improving the detection sensitivity of S_2F_{10} in SF_6 because the mass spectrum of SOF_2 contains several ion masses (i.e. 86, 67, and 48) which do not appear in the SF_6 mass spectrum. Thus for masses 86, 67, and 48 there is no signal due to the ionization of SF_6 and thus no interference with the S_2F_{10} peak.

Figure 7 also shows the differences in S_2F_{10} detection sensitivities for mass 19, 48, and 86 ions in the presence of SF_6. The mass 19 signal has no observable S_2F_{10} feature due to the large sloping background signal from SF_6. However the mass 48 and 86 signals exhibit no background from SF_6 and have clearly defined S_2F_{10} features. The detection limit of S_2F_{10} in SF_6 by this technique is on the order of 1 ppm_v using the present, un-modified GC/MS instrument. Although there is reason to suspect that it

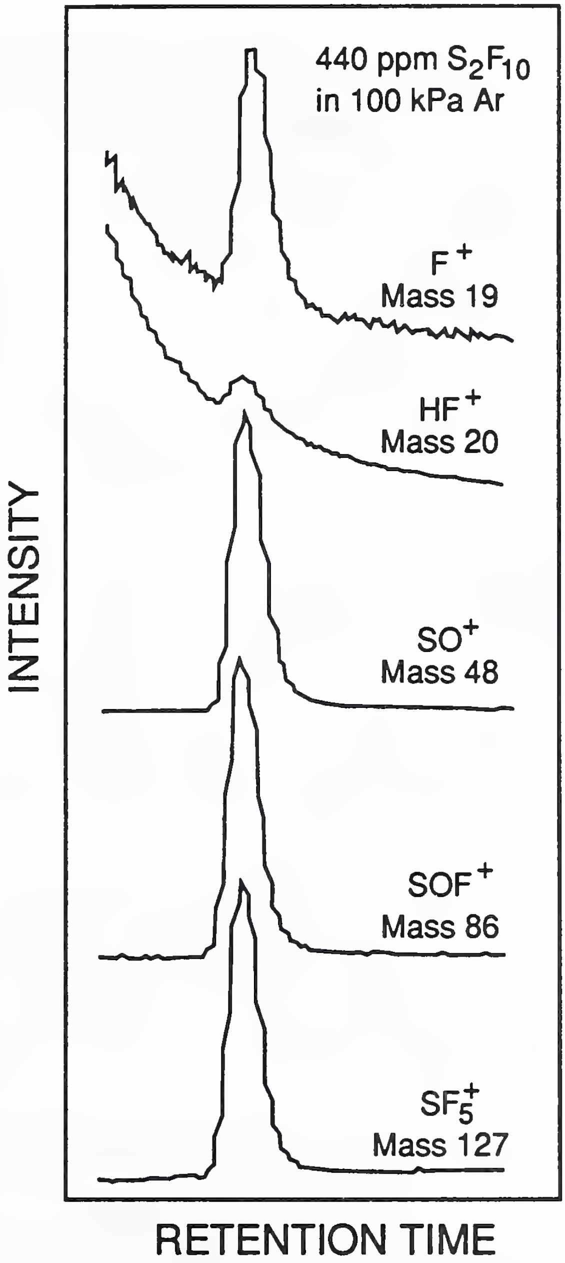

Figure 6. S_2F_{10} features observed using a GC/MS with a silicon-rubber membrane separator. For masses 19 and 20 there is a large sloping background from doubly charged argon ions.

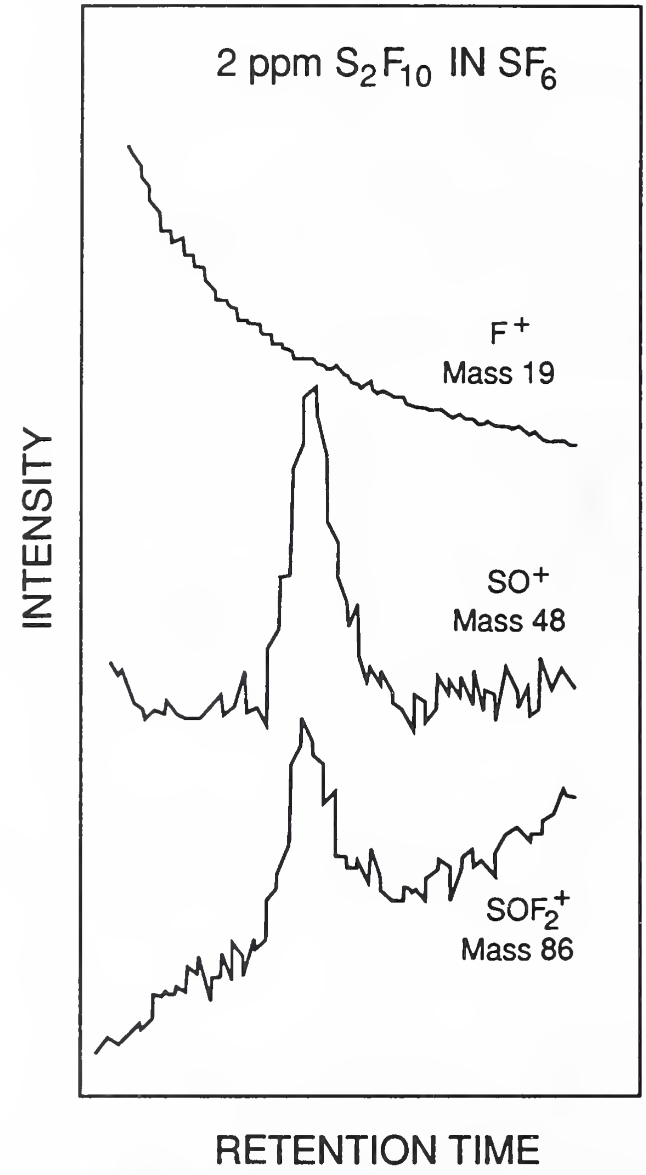

Figure 7. S_2F_{10} features observed using a GC/MS with a silicon-rubber membrane separator to analyze a very dilute (2 ppm_v) mixture of S_2F_{10} in SF_6.

should be possible to achieve a higher detection sensitivity by modifying the GC/MS configuration and operating conditions, there was no attempt to do this since the instrument had adequate sensitivity for the experiments and tests described in the following sections.

The GC column employed for S_2F_{10} detection was a 24′ × 1/8" Teflon tube containing 30% SP-2100 (Supelco) on 80/100 chromosorb WAW [47]. The column was operated using helium as a carrier gas with a GC oven temperature between 25 °C and 50 °C and a carrier gas flow rate in the range 20–30 ml/min. The membrane between the GC and MS consisted of a silicone-rubber material. The water content of the inlet tube was evidently maintained by the gas flow at a sufficient level for the S_2F_{10} conversion. No attempt was made to dry the carrier gas before it entered the column.

It should be noted that a similar type of conversion of SOF_4 into SO_2F_2 for the same GC/MS configuration was reported in the earlier work of Van Brunt [31]. In this case the conversion also involves water via the hydrolysis [49]

$$SOF_4 + H_2O \longrightarrow SO_2F_2 + 2HF,$$

but offers no advantage for SOF_4 detection. It should also be noted that the Porapak Q column previously used to detect the oxyfluorides SOF_2, SO_2F_2, and SOF_4 in SF_6 will not pass S_2F_{10}. The reason why one column passes S_2F_{10} and the other does not presently remains obscure.

2.3 Surface Catalyzed Decomposition of S_2F_{10}

Preliminary work conducted in our laboratory [27] has indicated that S_2F_{10} may be unstable and decomposes into SOF_2, SF_6, and other by-products when stored in stainless steel gas-sampling cylinders at room temperature. This instability brings into question the reliability of gas sampling procedures used for S_2F_{10} analysis. It also raises questions about maintenance of reliable reference samples containing known amounts of S_2F_{10} that are necessary for calibration of analytical equipment.

Since the half-life for gas-phase unimolecular decay of S_2F_{10} at room temperature is extremely long ($\sim 10^7$ years) [50], it is speculated that the observed decomposition of S_2F_{10} inside sample cylinders must be due to unknown catalytic processes occurring on surfaces. We report results of a study to investigate these surface reactions. Possible reaction mechanisms for surface decomposition of S_2F_{10} are proposed and approximate rates of decay have been determined. Additionally, conditions which affect the decay rates have also been studied. The findings of these experiments provide a basis for preliminary recommendations on S_2F_{10} sampling, storage, and testing procedures.

The experimental method for the study of S_2F_{10} decomposition on surfaces was straightforward. Gas sampling cylinders of various sizes and materials (primarily stainless steel) were conditioned so that for each test all cylinders began with surface conditions that were as similar as possible. Each cylinder was then filled with a known mixture of S_2F_{10} and argon. Argon was used as a buffer gas because of its chemical inertness and because its presence did not interfere with either the detection of S_2F_{10} or its decomposition products. In other buffer gases, such as N_2 and SF_6, S_2F_{10} exhibited similar decomposition properties. The concentrations of S_2F_{10} and the primary decomposition products, such as SOF_2 and SF_6, were then monitored as a function of time to determine the rate of decomposition.

The GC/MS technique described in the previous section was used to detect S_2F_{10}. The absolute quantities of S_2F_{10} and its decomposition products were determined by making direct comparisons of the observed GC/MS responses with those from reference gas samples containing known quantities of S_2F_{10}, SF_6, SOF_2, and Ar.

Figure 8 shows the decomposition curves for S_2F_{10} and the related production curves for the two main observable gas-phase products, SF_6 and SOF_2, in two experiments with different experimental conditions (see figure caption).

Note that the S_2F_{10} sample in the experiment shown in Figure 8a took approximately 75 days to decompose, while the sample from Figure 8b took only 75 hours to disappear. This large variation in decay times indicates the importance of understanding the mechanisms of the S_2F_{10} decomposition in order to minimize the effects on experiments and sample storage. Interestingly, despite the differences in decay times and experimental conditions, the curves in Figures 8a and 8b are very similar in shape and magnitude and the fraction of S_2F_{10} which ultimately formed SF_6 is about the same in both cases. The most significant difference between these two experiments is in the amount of water contamination that was present (see the caption for Figure 8).

The approximate rate coefficients corresponding to the S_2F_{10} decay curves in Figures 8a and 8b may be calculated as approximately $7 \times 10^{-7}\mathrm{s}^{-1}$ and $2 \times 10^{-5}\mathrm{s}^{-1}$, respectively. While both coefficients are fairly small and differ by more than an order of magnitude from each other, both values are significantly below the estimated gas-phase unimolecular decay rate coefficient of S_2F_{10} at room temperature. The thermal unimolecular decomposition rate at temperature T [50] is given by:

$$k = 5.8 \times 10^{18} \exp(-45700/\mathrm{R}T) \tag{14}$$

based on the reaction data [51] obtained in the temperature range 435–454.5 K where RT is given in calories and k in s^{-1}. At $T = 300\,\mathrm{K}$ (room temperature), Eq. (14) gives a half-life for S_2F_{10} of 10^7 years. The gas-phase hydrolysis is also reported to be very low [52], i.e., S_2F_{10} essentially does not react with water vapor at room temperature. It therefore appears that the decomposition of S_2F_{10} occurs preferentially on the surface of the stainless steel cylinders. The facts that the decomposition rate goes up with H_2O contamination and that SOF_2 and SF_6 are initially the primary products suggests that water plays a major role in the decomposition, and that at least a

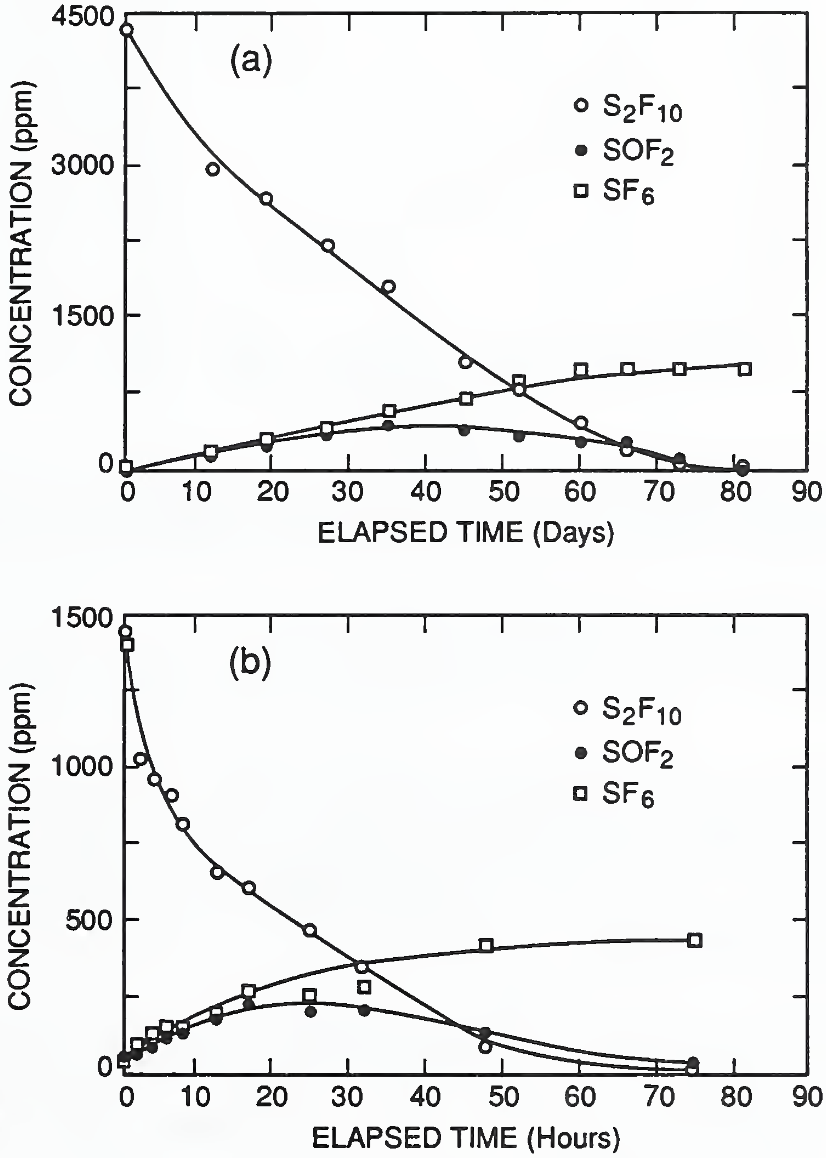

Figure 8. Decomposition of S_2F_{10} and corresponding production of SOF_2 and SF_6 with time for two experiments with the following conditions: (a) 78 ml stainless steel cylinder; 2.1 cm^{-1} surface-to-volume ratio; Argon buffer gas; Pressure = 1 atm; 4500 ppm_v starting concentration; Temperature = 25 °C; no water added; (b) 24 ml stainless steel cylinder; 2.5 cm^{-1} surface-to-volume ratio; Argon buffer gas; Pressure = 1 atm; 1500 ppm_v starting concentration; Temperature = 25 °C; 1 μl liquid water added.

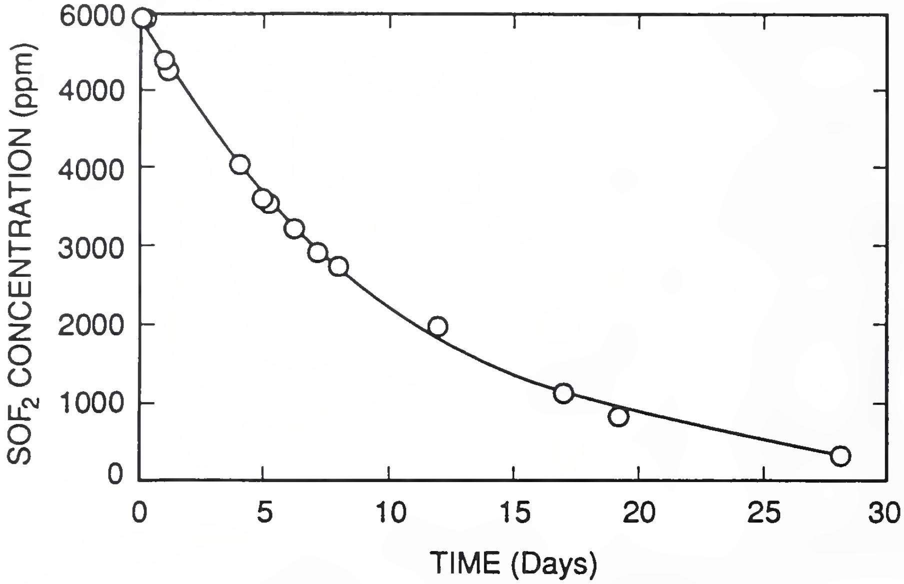

Figure 9. Decomposition of SOF_2 with time under the following experimental conditions: 32 ml stainless steel cylinder; 2.6 cm^{-1} surface-to-volume ratio, Argon buffer gas; Pressure = 1 atm; 6000 ppm_v starting concentration; Temperature = 25°C; and no water added.

portion of the S_2F_{10} decomposes via a reaction such as

$$S_2F_{10} + H_2O \xrightarrow{\text{surface}} SOF_2 + SF_6 + 2HF. \tag{15}$$

Although HF is detected in the sample cylinder as the S_2F_{10} decomposes, the amounts are difficult to quantify and therefore not shown in Figure 8. The exact nature of reaction (2) has not been determined. It may correspond to direct hydrolysis of S_2F_{10} on the surface, or perhaps a disproportionation reaction into $SF_6 + SF_4$ followed by hydrolysis of the SF_4 product.

Surface hydrolysis of other sulfur-fluoride compounds has been previously [8] observed but is not fully understood. Note that SOF_2 also decomposes in stainless steel cylinders as is evident by the eventual decrease in the SOF_2 concentration shown in Figure 9. This decomposition cannot be due to gas-phase hydrolysis because the rate [49] for the gas-phase reaction

$$SOF_2 + H_2O \longrightarrow SO_2 + 2HF, \tag{16}$$

is much too slow to account for the observed loss of SOF_2 and because SO_2 was detected as only a minor product in the experiments shown in Figure 8. Therefore the SOF_2 decomposition is probably due to surface catalyzed reactions similar to that observed for S_2F_{10}.

Were reaction Eq. (15) the sole mechanism for S_2F_{10} decomposition, then the amount of decomposed S_2F_{10} should equal the amount of SOF_2 and SF_6 produced. However

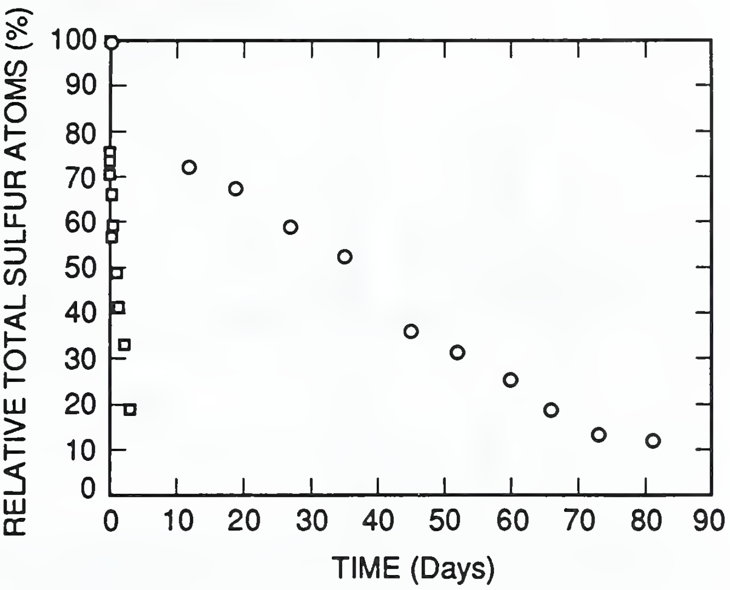

Figure 10. Total normalized sulfur content in identifiable gas-phase molecules as a function of time for the two decomposition experiments described in (○) Figure 8a and (□) Figure 8b.

it is obvious from the sum of the absolute concentrations of all the identified gas-phase sulfur-containing compounds (S_2F_{10}, SF_6, SOF_2) in the cylinder, that all of the sulfur initially present in the cylinder as S_2F_{10} cannot be accounted for by the observed gaseous products (see Figure 10).

While the decomposition of SOF_2 is obviously a contributing factor to the overall loss of sulfur atoms, it cannot account for the entire effect since even at very short times the amount of detectable sulfur in gas-phase molecules is less than that present when the sample was prepared. Additionally, if reaction (15) were the only mechanism for S_2F_{10} decomposition and the hydrolysis of SOF_2 were the only source of the loss of sulfur, then at long times (i.e. after all the S_2F_{10} has decomposed) the concentration of SF_6 should equal the initial concentration of S_2F_{10} since, as expected, SF_6 does not exhibit any decomposition. However, it is obvious from Figures 8 and 10 that the final concentrations of SF_6 are only about 20–30% of the initial S_2F_{10} concentrations and account for only 10–15% of the available sulfur. Thus it appears that some of the end products of S_2F_{10} decomposition adhere to the surfaces or are gaseous species that have yet to be identified. An electron-impact mass spectrum of a decomposed S_2F_{10} sample in argon from a stainless steel container (Figure 11a) provides evidence to support the latter speculation.

Only the labeled peaks in Figure 11a are identifiable as ions from S_2F_{10} or ions from sulfur-containing decomposition products. The other peaks represent unidentified gaseous products from the decomposition of S_2F_{10} in stainless steel cylinders. The GC/MS analysis indicates that the mass 47, 81, and 96 peaks correspond to ions that are most likely from the same compound. Although a positive identification of the

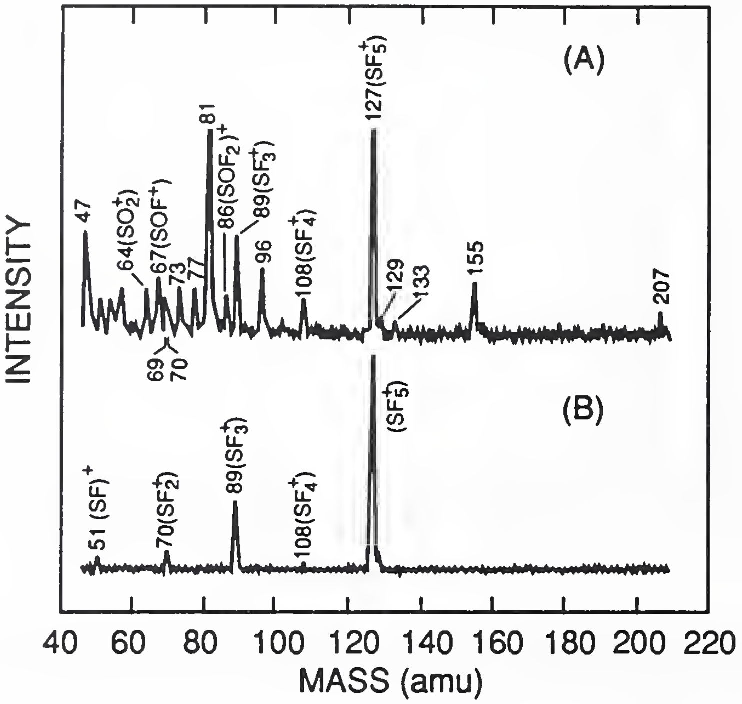

Figure 11. (a) Electron impact mass spectra of an S_2F_{10} in Ar sample stored in a 75 ml stainless steel cylinder for 35 days. Only 100 ppm_v of an original 5000 ppm_v of S_2F_{10} remains. (b) Mass spectrum of an undecomposed 3000 ppm_v S_2F_{10} sample in Ar.

species with a mass spectrum containing these ions has not been made, the 15 amu difference between mass 96 and 81 (possibly due to a CH_3 fragment) suggests that the compound contains carbon, thus indicating reactions with the container walls. It is significant that this species does not appear in glass or Teflon containers and appears in stainless steel even when only SOF_2 is initially present. Interestingly, S_2F_{10} samples in N_2 buffer gas produce products with mass spectra that differ considerably from Figure 11a. Evidence exists of unidentified products containing nitrogen, thus indicating that N_2 can play an active role in the catalytic process.

While the observed decomposition processes discussed in the preceding paragraphs are not fully understood, many of the implications of the decomposition processes are clear. Under the most extreme conditions, S_2F_{10} samples decompose significantly within a matter of hours (Figure 8b). This could affect the accuracy and sensitivity of tests used to determine concentrations of S_2F_{10} in gas-insulated equipment if appropriate sampling guidelines are not determined and followed. Even if the decomposition rate of a particular S_2F_{10} sample is not as great as that shown in Figure 8b, the long-term decomposition of S_2F_{10} reference samples makes careful quantification of S_2F_{10} concentrations and production rates more difficult and significantly more uncertain. Thus, in a very practical way, a more complete understanding of the parameters which affect the decomposition rate of S_2F_{10} samples

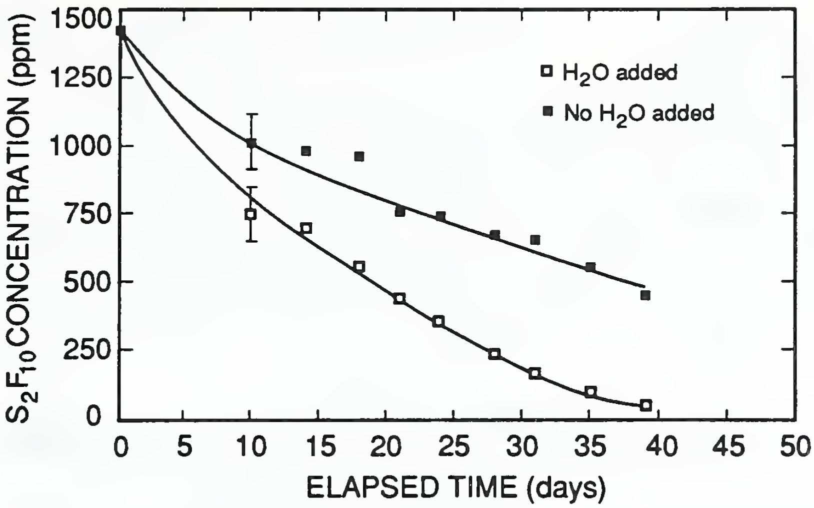

Figure 12. Decomposition of S_2F_{10} as a function of time for two 1400 ppm$_v$ S_2F_{10} samples in 1 atm Ar in 150 ml stainless steel cylinders. For one sample (□), 1 μl of liquid water was injected into the cylinder prior to filling with gas.

is essential in the ongoing research to investigate S_2F_{10} production in SF_6-insulated equipment.

As indicated by the above discussion, water appears to be an essential ingredient in the decomposition of S_2F_{10}. The possible influence of water was examined further by preparing two identical S_2F_{10} samples (1400 ppm$_v$ S_2F_{10} in 1 atm Ar in 150 ml stainless steel cylinders) with 1 μl of liquid water added to one of the samples. No attempt was made to remove all of the initial moisture on the walls of the cylinders beyond initially evacuating the cylinder to $\sim 2 \times 10^{-2}$ torr before preparing the samples. The S_2F_{10} concentrations were then monitored as a function of time and the results are shown in Figure 12.

Consistent with the results in Figure 8, the sample with added water decomposed significantly faster than the sample exposed to only residual moisture in the cylinder, again confirming that water plays a significant role.

Temperature has also been identified as a factor in the rate of S_2F_{10} decomposition in stainless steel cylinders. Figure 13 shows the results of an experiment where three S_2F_{10} samples (500 ppm$_v$ in 1 atm Ar in 150 ml stainless steel cylinders) were allowed to decompose at different temperatures.

The rate of decomposition increased dramatically as the sample temperature increased. Calculations using Eq. (14) show that the gas-phase unimolecular decay rate increases significantly from 25° C to 50° C, but is still many orders of magnitude lower than required to account for the decomposition of S_2F_{10} observed here. Thus the temperature of the sample (and/or the surface) clearly affects the rates of the reactions occurring on the surface of the sample cylinders.

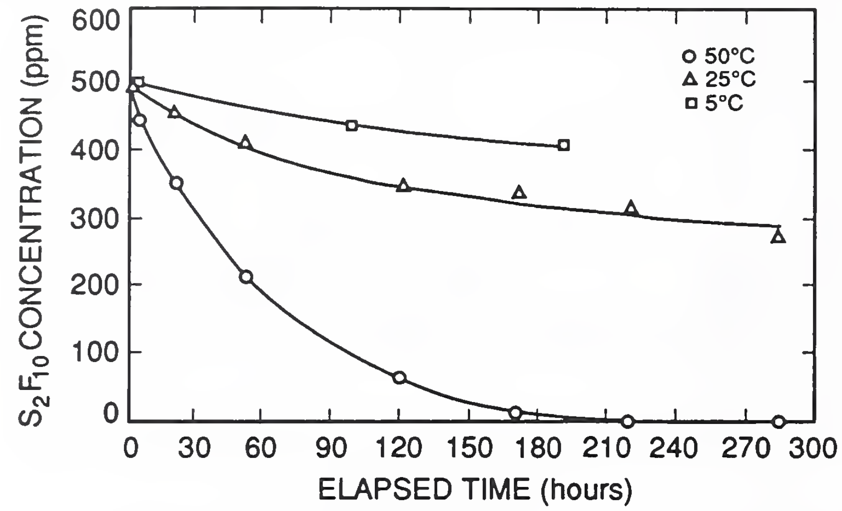

Figure 13. Decomposition of S_2F_{10} as a function of time at different temperatures. Samples were 500 ppm$_v$ S_2F_{10} in 1 atm Ar in 150 ml stainless steel cylinders.

While storing samples of S_2F_{10} in our laboratories for long periods of time, it became evident that samples at lower pressure often decayed more rapidly than those at higher pressures. More careful studies of this pressure dependence indicate that at pressures below approximately 100 kPa (~ 1 atm), lower-pressure samples decompose faster than higher-pressure samples. However, above 100 kPa little or no difference was observed in decomposition rates for samples at different pressures. Since this type of pressure dependence is not expected from simple gas-kinetic considerations [53], it is speculated that the surface conditions upon which S_2F_{10} decomposition depends could be affected by the gas pressure.

From chemical kinetics theory [53], it is expected that the reaction rate for decomposition of S_2F_{10} on a surface will be proportional to surface area. This behavior is supported by a large body of evidence from our work indicating that S_2F_{10} samples decompose more rapidly as sample cylinder surface-to-volume ratio increases. However, a direct proportionality of S_2F_{10} decay rate to cylinder surface-to-volume ratio has not yet been verified.

The data shown in Figures 8–13 apply only to 304 stainless steel sample cylinders. It is important to determine if the use of cylinders made of other materials would significantly affect the observed S_2F_{10} decomposition rates. Preliminary comparative experiments using stainless-steel, Monel, Teflon, and glass cylinders indicate that under reasonably dry conditions [54] all decay rates were within approximately 20 % of each other. Apparently, the presence of water is a more significant factor than the type of surface material. Results from a series of experiments using the same cylinders under "wetter" conditions, currently in progress, indicate that the rate of decomposition is fastest in Monel, followed by stainless steel and Teflon.

While additional investigation of the mechanisms of S_2F_{10} decomposition need to be performed, preliminary guidelines for S_2F_{10} sample storage are suggested from the results of this study. To minimize the rate of decomposition, gas samples containing S_2F_{10} should be prepared under conditions that are as dry as possible in cylinders that are as large as possible and stored at low temperatures. However, it must be noted that in this study, even the samples which were stored under the most favorable conditions exhibited significant decomposition over sufficiently long periods of time. Thus continued research needs to be pursued in order to develop better methods for maintaining standard-reference S_2F_{10} samples and for assessing sample stability.

2.4 Production of S_2F_{10} in SF_6 Corona Discharges

The rates of S_2F_{10} production from negative point-plane, dc glow-type corona discharges in SF_6 at a pressure of 200 kPa ($\sim$ 2 atm) were measured at different discharge current levels. The negative glow corona was chosen for this initial investigation into S_2F_{10} production from SF_6 because it is easily controlled and amenable to theoretical modelling as discussed in the next section. Although S_2F_{10} can also be generated by positive corona and spark discharges in SF_6, these types of discharges are, because of their transient nature, more difficult to control and characterize. Also, unlike spark-type discharges, the negative glow corona is a "cold" discharge in which the electron temperature greatly exceeds the gas temperature. It is therefore easier to model this discharge because it is possible to use rates for electron-collision processes that apply at room temperature.

If the measurements are performed at a constant discharge current i, then it is convenient to express the rate of S_2F_{10} production in units of charge, where the charge rate-of-production $d[S_2F_{10}]/dQ$ is related to the time rate-of-production $d[S_2F_{10}]/dt$ by

$$d[S_2F_{10}]/dQ = i^{-1}d[S_2F_{10}]/dt. \tag{17}$$

Here Q is the net charge transported as given by $Q = it$. The slope of the measure $[S_2F_{10}]$-versus-Q curve therefore yields a production rate as defined by Eq. (17).

The measurements of S_2F_{10} production were carried out in a manner similar to that previously used to measure the rates for oxyflouride production from SF_6 [31, 55]. The corona discharge was generated in 3.7-liter chamber using stainless-steel electrodes with a point-to-plane gap spacing of 1.0 cm and a point radius-of-curvature of about 0.08 mm. The discharge chamber was maintained at room temperature ($\sim$ 300 K). Periodic quantitative analyses of the gas subjected to corona discharge were performed approximately once every hour during operation of the discharge. The absolute quantity of S_2F_{10} present at any time in the discharge cell was determined quantitatively by making direct comparisons of the observed GC/MS response with that obtained using a reference gas sample containing a known concentration of S_2F_{10}

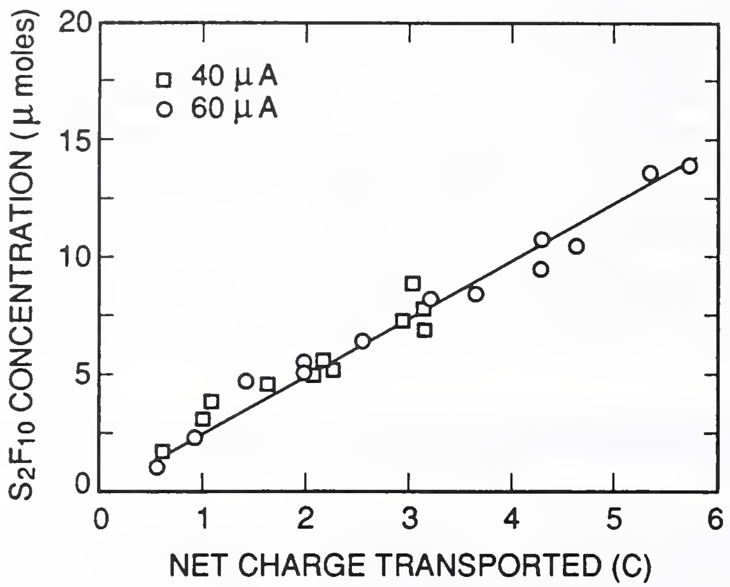

Figure 14. Measured absolute yields of S_2F_{10} versus net charge transport from negative corona in SF_6 for two discharge current levels of 40 and 60 μA

in SF_6. The method of S_2F_{10} detection is the same as described in the previous two sections.

Examples of results on absolute S_2F_{10} yields versus net charge transported are shown in Figure 14 for two different

discharge currents of 40 and 60 μA. These results apply to initially "pure" SF_6 at an absolute pressure of 200 kPa. It is significant to note that the results for both discharge currents exhibit the same constant charge rate-of-production of about 2.4 μmoles/coulomb as determined by the slope of the straight line fit to the data shown in the figure. This is a result which is expected from theoretical calculations discussed in the next section and indicates from Eq. (17) that the time rate-of-production for S_2F_{10} is proportional to the discharge current. The fact that the production appears to be linear suggests [31, 56] that secondary S_2F_{10} production and destruction processes are relatively unimportant.

It should be noted that the measured S_2F_{10} production rate at 60 μA is lower than the rate obtained from our previous preliminary measurements [25]. Our previous results at this current were in error due to the fact that the reference S_2F_{10} gas sample had significantly decomposed (see Figure 2 of Ref. [25]). Due to the problems discussed in the previous section, we were unable to properly correct for the loss of S_2F_{10} and thus overestimated the amount present in the reference sample. An overestimation of the S_2F_{10} concentration will necessarily lead to an overestimation of the production rate.

The production rate for S_2F_{10} reported here is also lower by at least a factor of 0.5 than the rates measured by Sauers [25] under somewhat similar conditions. Sauers reported difficulties in obtaining reproducible results that have yet to be resolved (see Figure 5 of Ref. [25]). Results given here, however, were found to be quite reproducible provided a reliable reference sample was used for the quantitative analysis of S_2F_{10}.

The implication from results such as shown in Figure 14 is that S_2F_{10} is readily formed from SF_6 in corona discharges and its production rate in enclosed SF_6-insulated systems can greatly exceed its destruction rate due, for example, to surface reactions discussed in the previous section. Were corona discharges to occur continuously in a system containing SF_6, it is possible that S_2F_{10} could build up to dangerously high levels within relatively short times.

2.5 Model for Corona Discharge-Induced Decomposition of SF_6

In this section we discuss a chemical-kinetics model for oxidation of SF_6 in negative glow-type corona discharges and apply the model to prediction of production rates for the gaseous by-products SOF_2, SOF_4, SO_2F_2, SO_2, and S_2F_{10} which can be compared with experimental results such as those reported in the previous section for S_2F_{10}. The model considers the influence of the common gaseous contaminants O_2 and H_2O on the various by-product yields.

2.5.1 Summary of Observations for Which the Model Must Account

A theoretical chemical kinetics model for SF_6 decomposition in point-plane negative glow-type corona discharges must be consistent with a set of observed trends. These include: 1) The yields for SOF_2, SO_2F_2, and S_2F_{10} versus time (or equivalently versus charge transported Q) are linear [31], [55–59]; 2) The yields for SOF_4 can exhibit nonlinearities that suggest a destruction process for this species with a rate proportional to the amount of SOF_4 present in the gas at any given time [56]; 3) The charge rates-of-production, $d[X]/dQ$, where $[X]$ is the concentration of any of the species SOF_2, SO_2F_2, SOF_4, or S_2F_{10}, are not significantly dependent on the discharge current for currents in the range of 10 to 100 μA [31]; 4) Most (greater than 90%) of the SF_6 molecules that dissociate in the discharge region by electron collisions lead to fragments that recombine to form SF_6 [59], i.e., less than 10% of the dissociated SF_6 molecules result in oxidation by-product formation; 5) The production rates for SOF_2, SO_2F_2, and SOF_4 are relatively insensitive to water vapor content in the gas below about 0.2% [31, 60], whereas there is evidence that S_2F_{10} yield increases with increasing water vapor content [25]; 6) The production rates for SOF_2, SO_2F_2, and SOF_4 are insensitive to O_2 concentration for $[O_2] < 2\%$ [31, 55, 59]; 7) The yield of SO_2 is insignificant compared to the yields of the other gaseous by-products and

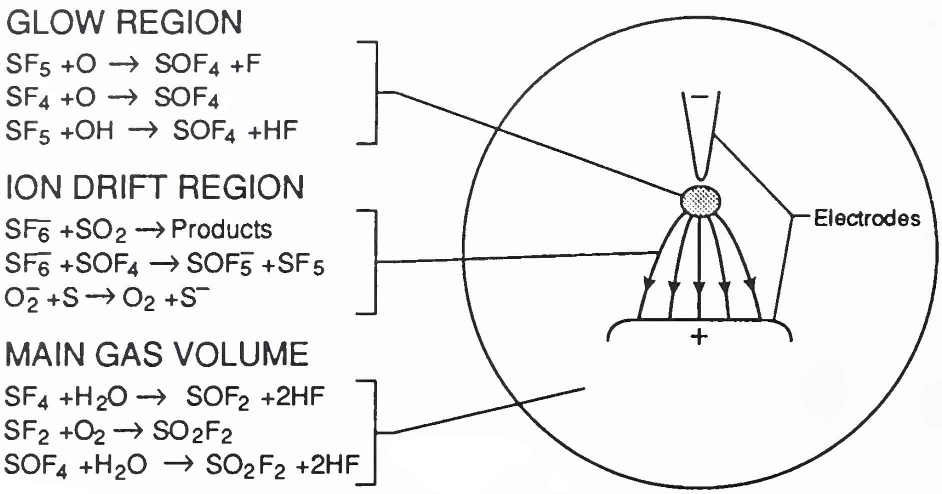

Figure 15. Regions of differing chemical activity associated with a three-zone model for SF_6 decomposition in negatives point-plane corona.

tends to decrease with increasing $[O_2]$ [31, 59]; 8) The oxyfluoride SOF_2 derives its oxygen predominantly from H_2O, whereas SO_2F_2 derives oxygen predominately from O_2 independent of oxygen content in the gas [55] 9) The oxyfluoride SOF_4 can derive oxygen from both H_2O and O_2, where O_2 makes an increasingly greater relative contribution to SOF_4 production as $[O_2]$ increases [55]; 10) At a discharge current of $40\,\mu A$, $d[SOF_4]/dQ > d[SOF_2]/dQ > d[SO_2F_2]/dQ > d[S_2F_{10}]/dQ$ [25, 31].

In the present work the previously proposed model for corona chemistry in SF_6 [61] has been extended to include the effect of O_2 in the gas, thus allowing prediction of the SO_2F_2 yields. The production rates for SOF_2, SO_2F_2, SOF_4, and S_2F_{10} are computed using the presently revised model for different discharge currents and different relative concentrations of H_2O and O_2 in the gas. The results are found to be reasonably consistent with the observed trends mentioned above. The extent to which the present model is also consistent with rates for known processes is discussed.

2.5.2 Model Description

The basic features and assumptions of the chemical kinetics model used for the present calculations are given by Van Brunt and coworkers [61]. As illustrated in Figure 15, the model considers three zones of differing chemical activity which are coupled by diffusion of species into or out of the different zones. The three zones are: 1) the active glow region near the point electrode where electron-collision processes occur and the chemistry predominantly involves fast reactions among highly reactive free radicals and ions; 2) the ion-drift region which corresponds to that part of the interelectrode gap outside of the glow region where the chemistry is dominated by ion-molecule reactions; and 3) the main gas volume which is much larger than either the glow or

Table 3. Reaction scheme for active corona glow region ($i = 40\mu$A)

1m.	$e + SF_6 \rightarrow SF_5 + F + e$	$k_1 = 240$ 1/s
2m.	$e + SF_6 \rightarrow SF_4 + 2F + e$	$k_2 = 1.7$ 1/s
3m.	$e + SF_6 \rightarrow SF_2 + 4F + e$	$k_3 = 1.4$ 1/s
4m.	$e + H_2O \rightarrow H + OH + e$	$k_4 = 500$ 1/s
5m.	$e + O_2 \rightarrow O + O + e$	$k_5 = 14$ 1/s
*6m.	$SF_4 \rightarrow SOF_2$	$k_6 = 377$ 1/s
*7m.	$SF_2 \rightarrow SO_2F_2$	$k_7 = 465$ 1/s
8m.	$SF_5 + F \rightarrow SF_6$	$k_8 = 2.2 \times 10^{-10}\,\mathrm{cm^3/s}$
9m.	$SF_5 + SF_5 \rightarrow S_2F_{10}$	$k_9 = 6.0 \times 10^{-13}\,\mathrm{cm^3/s}$
10m.	$SF_5 + SF_5 \rightarrow SF_4 + SF_6$	$k_{10} = 5.0 \times 10^{-13}\,\mathrm{cm^3/s}$
11m.	$SF_5 + OH \rightarrow SOF_4 + HF$	$k_{11} = 1.6 \times 10^{-12}\,\mathrm{cm^3/s}$
12m.	$SF_5 + O \rightarrow SOF_4 + F$	$k_{12} = 2.0 \times 10^{-11}\,\mathrm{cm^3/s}$
13m.	$SF_4 + OH \rightarrow SOF_3 + HF$	$k_{13} = 3.6 \times 10^{-15}\,\mathrm{cm^3/s}$
14m.	$SF_2 + O \rightarrow SOF + F$	$k_{14} = 1.1 \times 10^{-11}\,\mathrm{cm^3/s}$
15m.	$SOF + O \rightarrow SO_2F$	$k_{15} = 1.0 \times 10^{-10}\,\mathrm{cm^3/s}$
16m.	$SO_2F + F \rightarrow SO_2F_2$	$k_{16} = 1.0 \times 10^{-10}\,\mathrm{cm^3/s}$
17m.	$SOF + F \rightarrow SOF_2$	$k_{17} = 2.0 \times 10^{-12}\,\mathrm{cm^3/s}$
18m.	$SOF_3 + OH \rightarrow SO_2F_2 + HF$	$k_{18} = 1.0 \times 10^{-13}\,\mathrm{cm^3/s}$
19m.	$F + H_2O \rightarrow OH + HF$	$k_{19} = 1.1 \times 10^{-11}\,\mathrm{cm^3/s}$
20m.	$F + OH \rightarrow FOH$	$k_{20} = 5.0 \times 10^{-13}\,\mathrm{cm^3/s}$
21m.	$H + OH \rightarrow H_2O$	$k_{21} = 5.0 \times 10^{-13}\,\mathrm{cm^3/s}$
22m.	$F + H \rightarrow HF$	$k_{22} = 1.0 \times 10^{-13}\,\mathrm{cm^3/s}$
23m.	$F + F \rightarrow F_2$	$k_{23} = 2.0 \times 10^{-16}\,\mathrm{cm^3/s}$
24m.	$OH + OH \rightarrow H_2O + O$	$k_{24} = 2.0 \times 10^{-12}\,\mathrm{cm^3/s}$
25m.	$H + H \rightarrow H_2$	$k_{25} = 1.0 \times 10^{-15}\,\mathrm{cm^3/s}$
26m.	$F + SOF_3 \rightarrow SOF_4$	$k_{26} = 1.0 \times 10^{-10}\,\mathrm{cm^3/s}$
27m.	$O + SOF_3 \rightarrow SO_2F_2 + F$	$k_{27} = 5.0 \times 10^{-11}\,\mathrm{cm^3/s}$

* - diffusion controlled.

ion-drift regions and in which slow oxidation and hydrolysis processes among neutral species occur. The main difference between the present and previous models is the inclusion of more processes in the glow region which would be expected to occur when O_2 is added to the gas.

The reaction scheme for the discharge glow region used in the present model is shown in Table 3. The following assumptions were made in constructing this scheme: 1) the active glow region was assumed to be spherical with a radius determined from photographic observations of the uniform luminous discharge region near the point electrode; 2) consistent with observations, the size of the luminous region was assumed to be independent of discharge current and H_2O or O_2 content in SF_6; 3) the electric field-to-gas density ratio (E/N) in the active region was assumed to be that corresponding to the condition of electrical breakdown at which the ionization rate in the gas equals the electron attachment rate [62] as implied by theory [63] and recent observations [64]; 4) the concentrations of SF_6, O_2, and H_2O were assumed to be constant equal to their initial values as is justified by the condition of a small active region within a large relatively inactive gas volume, and by the fact that for the experiments with which the model is compared, only a small fraction, less than 0.05% of the gas actually decomposed; 5) only relatively fast reactions ($k > 10^{-15}\,\mathrm{cm^3/s}$) that have a good chance of going to completion in the glow region are permitted in order to satisfy the requirement that highly reactive species like SF_5, SOF, F, and O attain steady-state concentrations within times much shorter than typical observation intervals of 10 seconds or more; 6) the gas temperature is maintained at the ambient level of 300 K; 7) no surface reactions are included, which is justified by the highly confined nature of the active discharge region located at approximately the center of a gas cell that has a large volume-to-surface area ratio.

The electron-impact dissociation rates (Processes 1m–5m in Table 3) were estimated from dissociation coefficients calculated at the appropriate E/N by Phelps and Van Brunt [62] from numerical solutions of the Boltzmann transport equation for electron kinetic energy distributions. Processes 6m and 7m in Table 3 represent diffusion rates of SF_4 and SF_2 out of the glow region and into the main gas volume where they are assumed to convert to SOF_2 and SO_2F_2 respectively by the slow reactions

$$\mathrm{SF_4 + H_2O \longrightarrow SOF_2 + 2HF} \qquad (28\mathrm{m})$$

$$k_{28} = 2.0 \times 10^{-19}\,\mathrm{cm^3/s}$$

and

$$\mathrm{SF_2 + O_2 \longrightarrow SO_2F_2} \qquad (29\mathrm{m})$$

$$k_{29} < 5 \times 10^{-16}\,\mathrm{cm^3/s}.$$

The rate for reaction 28m was measured by Sauers and coworkers [65], and an upper limit for reaction 29m was determined by Plumb and Ryan [66]. The effective unimolecular rates given in the table for reactions (6m) and (7m) were estimated using the relationship [61]

$$k_j = 3D_j(1/R^2 + \lambda_j/R);$$

where

$$\lambda_j = (D_j/k_j'N')^{1/2}, j = \mathrm{6m, 7m},$$

D_j is the diffusion coefficient for either SF_4 or SF_2 in SF_6, R is the known radius of the glow region, k_j is the bimolecular reaction rate coefficient for either process 28m($j =$ 6m) or 29m($j =$ 7m), and N' is the density of either H_2O or O_2. Since $\lambda_j << 1/R$, k_j is approximately given by $3D_j/R^2$. Thus, the rate coefficients k'_j are not needed in this model, and the rates for conversion of SF_4 into SOF_2 and of SF_2 into SO_2F_2 are assumed to be diffusion controlled.

The concentrations of SOF_4 and SO_2F_2 in the main gas volume can also be affected by the slow reaction [49]

$$\mathrm{SOF_4 + H_2O \longrightarrow SO_2F_2 + 2HF} \tag{30m}$$

$$k_{30} = 1.0 \times 10^{-21}\mathrm{cm^3/s}.$$

In addition the production of SOF_4 can also be influenced by the F^- transfer reaction [56, 67, 68]

$$\mathrm{SOF_4 + SF_6^- \longrightarrow SOF_5^- + SF_5} \tag{31m}$$

$$k_{31} \simeq 2 \times 10^{-10}\mathrm{cm^3/s}.$$

which occurs in the ion-drift region. The present model does not include reactions 30m and 31m. Their effect is to sightly increase and decrease the rates of SO_2F_2 and SOF_4 formation respectively above and below the uniform rates predicted by the present model at long times.

In most cases the rates for the various reactions shown in Table 3 are quite comparable to those used previously [61], although some minor adjustments were made to improve agreement with measured yield curves. A direct electron-impact induced dissociation of SF_6 leading to SF_2 formation in a single step (reaction (3m)) has been added to the model. Evidence that such a process occurs is provided by the recent work of Ryan [69]. It is assumed here that less than 1% of the SF_6 dissociation events lead to SF_2. The relative contribution of this dissociation channel was adjusted to optimize the agreement with observed SO_2F_2 yields. Other fast reactions initiated by the presence of SF_2 (reactions (14m) – (17m) in Table 3) have also been included [66, 69, 70].

The calculations were performed using a chemical kinetics computer code described by Braun and coworkers [71].

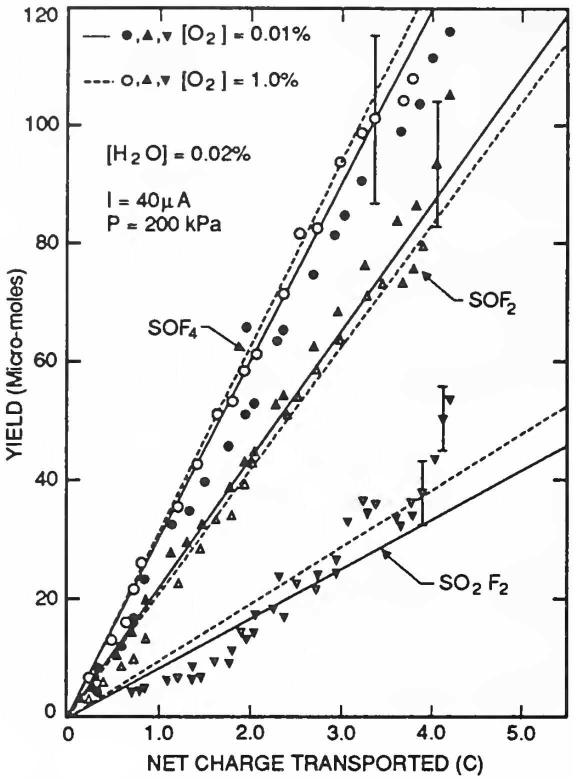

Figure 16. Calculated (lines) and measured (points) yields of oxyfluorides as a function of charge transported in the discharge at the indicated oxygen and water vapor concentrations in 200 kPa SF_6.

2.5.3 Results from Model Calculations

Using the model described in the previous section, yields versus net charge transported for the gaseous by-products SOF_4, SOF_2, SO_2F_2, and S_2F_{10} were calculated at two assumed relative O_2 concentrations $[O_2]/[SF_6] = 0.01\,\%$ and 1.0%, water vapor concentrations in the range of 50 to 400 $\mathrm{ppm_v}$, and corona discharge currents in the range of 5 to 80 μA. The results of these calculations are compared with experimental data on oxyfluoride and S_2F_{10} production in SF_6 negative corona discharges for a pressure of 200 kPa as reported by Van Brunt [31] and Sauers and coworkers [25]. Figure 16 shows a comparison between the measured and calculated oxyfluoride yields for a fixed discharge current and water vapor concentration and the two different indicated relative O_2 concentrations. As noted above, some adjustments were made in the rates of the processes indicated in Table 3 in order to achieve the reasonable agreement between the calculated and measured results seen in Figure 16. In particular, the rates for the electron-impact processes (2m) and (3m) were found to be critical in affecting SOF_2 and SO_2F_2 production respectively. At the present time no information exists about the relative contributions of the various different energetically allowed dissociation processes that can occur when SF_6 is excited by electron collisions. Therefore the rates given in Table 3 for processes (2m) and (3m) are simply those which are obtained with the present model when adjusted to give results consistent with experimental observations.

The calculated and measured oxyfluoride yields seen in Figure 16 do not depend significantly on O_2 content. This is expected for SOF_4 and SOF_2 because it is found [55] that when $[O_2] < 2\%$, both of these species derive their oxygen predominantly from H_2O thereby suggesting that SOF_4 is mainly formed by reaction (11m) in the glow region and SOF_2 by reaction (28m) in the main gas volume.

The model predicts that at low O_2 concentrations SO_2F_2 is primarily formed from SF_2 in the main gas volume by reactions (29m). As $[O_2]$ increases, an increasing fraction of SO_2F_2 can be formed from SF_2 via the reaction sequence (14m) through (16m). In either case SO_2F_2 yield is controlled by the SF_2 production rate and its formation primarily involves O_2 consistent with observations [55].

It should be noted that the present model does not include the fast reaction

$$SOF + O \longrightarrow SO_2 + F \tag{32m}$$

proposed by Plumb and Ryan [66]. If this reaction is included, it is found that the yield of SO_2 becomes comparable to that of the oxyfluorides which is not in agreement with observations for corona discharges which indicate very low SO_2 yields [31, 57, 59]. There is also no evidence of SO_2 production from SF_6/O_2 mixtures in rf glow discharges [72]. We speculate that under the discharge conditions considered here, SO_2F is more likely to be formed than SO_2 by the reaction of SOF with O (process 15m, in Table 3).

Figure 17 shows a comparison between measured and calculated discharge current dependencies of the charge rates-of-production for SOF_4, SOF_2, SO_2F_2, and S_2F_{10}. The calculated rates are consistent with the measured rates in two respects. Firstly, at all currents it is seen that

$$\frac{d[SOF_4]}{dQ} > \frac{d[SOF_2]}{dQ} > \frac{d[SO_2F_2]}{dQ}$$

and the rate of S_2F_{10} formation is below that of SO_2F_2 at 40 and 60 μA. Secondly, to within a factor of two, or within measurement uncertainties, there is no appreciable variation of the charge rates-of-production with current. In most cases the calculated rates fall below the measured values for all species. This may be due in part to the manner in which experimental data were analyzed to give "limiting rates" after a long time and in part to the assumption of a glow radius R that is slightly too small which thus has the effect of reducing the rates for the important rate-controlling electron-impact processes, reactions (1m)–(3m) [61].

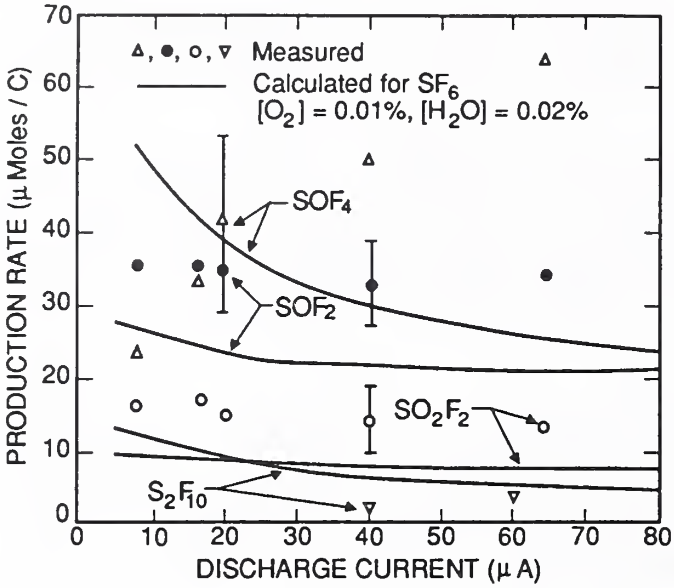

Figure 17. Calculated (lines) and measured (points) charge rates-of-production of oxyfluorides and S_2F_{10} as functions of discharge current for the indicated oxygen and water vapor concentrations in 200 kPa SF_6.

The dependencies of the production rates on water-vapor content are shown in Figure 18. It is seen that the production of both SOF_2 and SO_2F_2 are relatively insensitive to $[H_2O]$ as suggested by experimental observations [31, 60]. The increase in S_2F_{10} production with $[H_2O]$ is also consistent with observations [25]. The increase in SOF_4 production with $[H_2O]$, on the other hand, appears to be greater than previously suggested [31]. However, the measurement uncertainties for this species are generally quite large so that better experimental results on SOF_4 production may be needed before the dependence on $[H_2O]$ can be ascertained.

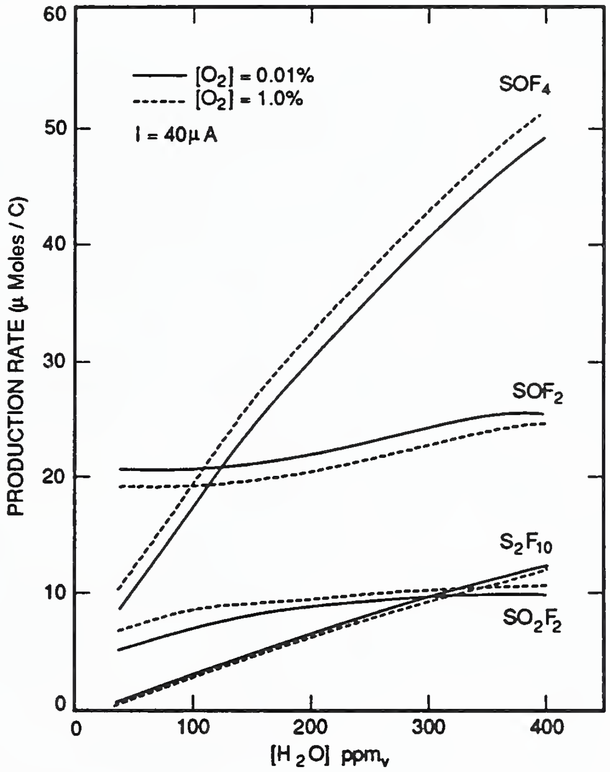

Figure 18. Calculated charge rates-of-production of the oxyfluorides and S_2F_{10} as functions of H_2O content in 200 kPa SF_6 for a 40 μA discharge and the different indicated O_2 concentrations.

3 LIQUID DIELECTRICS RESEARCH

Task 03

Kenneth L. Stricklett, Edward F. Kelley (Consulting Scientist),
H. Yamashita (Guest Scientist), and Charles Fenimore
Electricity Division
National Institute of Standards and Technology

3.1 Introduction

Liquid dielectrics are widely used within the power industry for their insulating and heat transfer properties. High-voltage apparatus must perform reliably under severe conditions: component materials are necessarily subjected to prolonged periods of high electrical-stress, high-voltage transients, and in the most extreme circumstances, exposure to electromagnetic pulses. Electrical breakdown within composite insulation systems often results in the catastrophic failure of high-voltage apparatus. This research seeks to improve our understanding of the initiation and growth of partial discharges and streamers in liquid dielectric materials, one component critical to the performance of composite insulation systems. Knowledge of the behavior of liquid dielectric materials under conditions of high electrical stress is essential in assessing the performance, safety, and reliability of existing facilities, as well as to the development of new high-voltage technologies.

Liquid dielectric breakdown is initiated by the propagation of a low density streamer in the liquid. Two areas of research are discussed in this report: A study of partial discharge behavior that addresses the initiation of streamers, and an investigation of the experimental conditions that influence propagation of prebreakdown streamers in liquid hydrocarbons. The results are obtained for n-hexane, a model system often used for the study of dielectric breakdown in liquid hydrocarbons.

In liquid hydrocarbons the early growth of the cathode streamer is distinct from that of the final stage. At inception, cathode streamer growth is internally limited and their propagation speeds are subsonic. Furthermore, cathode streamer growth is self regulating, that is, partial discharge activity may occur at voltages well below those required for complete breakdown. In the work discussed, temporal records of partial discharge current activity and frame photographs of the growth of a low density streamer in the liquid are obtained concurrently. Such data allow detailed description of the streamers at their inception.

Under uniform field conditions, two modes of electrical breakdown are observed in liquid n-hexane: breakdown may be initiated either by cathode or anode streamers. This observation suggests that two unique sets of phenomena lead to electrical breakdown. In the work described, high-speed photography is employed to obtain a record of each breakdown event thereby providing statistical information regarding the relative frequencies of anode and cathode processes. The degree to which the relative probability for either process is influenced by experimental conditions is discussed.

3.2 Partial Discharges in N-Hexane

The initiation of electrical discharges in liquids has received a great deal of attention in the last few years. However, despite this activity no clear consensus has been reached as to the mechanism for the initiation of the discharge. Several candidates have been proposed. Kattan, et al. [73] suggest that the initial discharge occurs as an avalanche in the liquid and that a bubble is created by energy deposited in the liquid. Korobejnikov and Yanshin [74] suggest that bubbles on the electrodes, microbubbles in the liquid, or bubbles generated due to Coulombic forces at the electrode surface may be significant to the initiation of partial discharges.

Based on experience in this laboratory, it seemed likely that particulate material may pay a role in the initiation of partial discharges. It was noted that partial discharge activity decreased if the liquid was filtered. Upon the addition of unfiltered liquid, or if the cell were vigorously shaken or the liquid circulated rapidly the partial-discharge activity was noted to increase. Furthermore, particulate material could be readily observed in the unfiltered liquid by the light scattered from a laser beam. These observations suggested that particles are significant to the initiation of partial discharges and, in part, motivated improvements to the optical system.

Earlier studies in n-hexane showed that during a partial discharge, injection of charge occurs in bursts of discrete pulses. The current pulses are clearly associated with the growth of a low density streamer in the liquid. The current pulses persist as long as the low density streamer is in contact with the needle. The current waveform at the initiation of the partial discharge is of particular relevance to the evaluation of models and had not been resolved in earlier studies.

The results discussed in this section are an extension of a study conducted in collaborative with the University of Tennessee [75, 76] (M. O. Pace, T. V. Blalock, A. L. Wintenburg, and I. Alexeff). Improvements in instrumentation have been made in two areas: in the amplifier used to detect partial discharge currents and in the optics used for the high speed photography.

3.2.1 Experimental Apparatus

A schematic of the experimental apparatus is shown in Figure 19. The test cell is constructed from brass and has provision for circulation and filtration of the liquid. The electrodes are enclosed within the cell and immersed in the liquid. The test

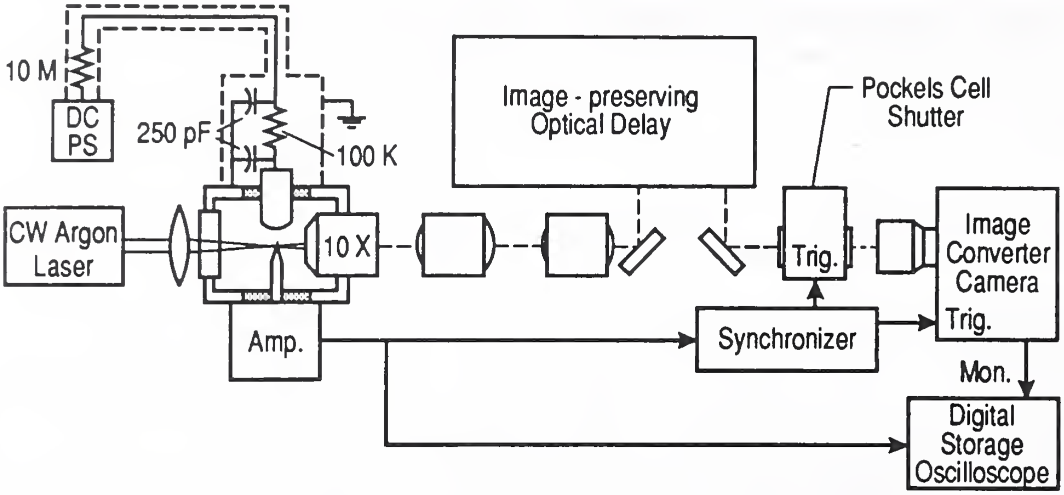

Figure 19. Experimental apparatus. The electrodes and the placement of the microscope objective are drawn approximately to scale.

gap consists of a steel needle and stainless steel rod separated by 3.2 mm. The rod electrode is 6.4 mm in diameter and has a 3.2 mm radius at the end. The radius of the needle tip is 1 μm; the apex angle is approximately 30° and the needle has a shank diameter of 1.0 mm. It is necessary to replace the needle periodically due to erosion of the tip.

The optical system is also shown in Figure 19. A continuous wave argon laser is used to illuminate the needle tip. A 10× microscope objective is mounted within the cell approximately 6 mm from the needle. The lenses following the objective recollimate the laser beam and place an image of the needle at the input to the image-preserving optical delay [75, 77]. A final image is produced just ahead of the Pockels-cell shutter. The remaining optics provide a 1× transfer of the image to the film plane of the camera. Due to the proximity of the objective to the needle, particulate material is gradually deposited on the lens surface, and it is necessary to clean the objective occasionally. The objective is carefully sealed to prevent the test liquid from entering the lens system. A scale drawing of the electrode gap and needle tip is shown in Figure 20. The framing sequence is also shown in the figure. The overall magnification is 200× and the optical resolution is $\leq 2\,\mu$m.

The current amplifier is connected directly to the needle electrode and is at ground potential. The output of the amplifier goes to a digital oscilloscope where the current waveform is recorded and to the synchronizer. The trigger level is set at the synchronizer, which in turn triggers the Pockels-cell shutter and image-converter camera. The amplifier has a bandwidth 70 MHz and an equivalent noise of 30 nA rms. The estimated charge sensitivity is less than 1 fC.

Knowledge of the temporal relationship between the frame photographs and the current waveform is essential to this study. The frame times are determined from the

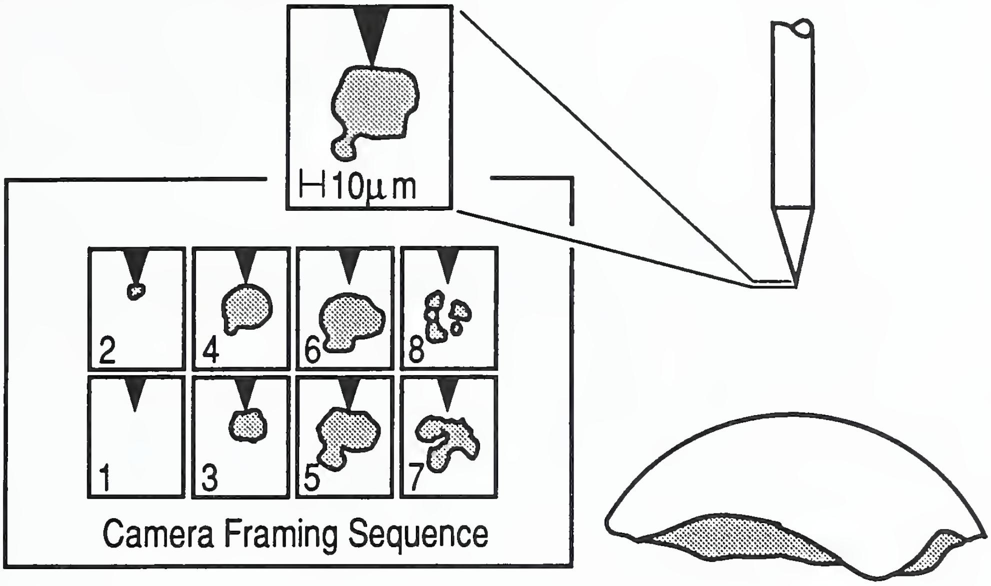

Figure 20. Electrode configuration. The region viewed by the image-converter camera is shown. A single frame is expanded to show the scale at 200× magnification. The frame sequence is also shown.

record of the camera monitor pulse and the frame interval. The frame intervals were carefully evaluated and found to be 512, 217 and 51 ns. Photographs are obtained at each of these intervals. Most of the photographs shown here, however, are obtained with the 512 ns frame interval. The useful laser power is limited to $< 2.5\,\mathrm{W}$ due to thermal blooming in the liquid. At these light levels the frame photographs at the faster frame intervals are under exposed and do not reproduce well.

A HV DC power supply is connected to the spherical electrode. A 10-MΩ resistor is put in series to limit the current in the event of a breakdown. The filter circuit shown between the electrode and power supply is provided to reduce noise pickup from the power supply. The filter capacitor must be large enough to ensure a constant voltage at the needle tip. The voltage required for detectable partial discharge activity is $\simeq 12\,\mathrm{kV}$. At these voltages the charge on the filter capacitor is of the order of μC. The total charge injected during a partial discharge is of the order of several pC, six orders of magnitude less than the available charge.

3.2.2 Partial Discharges as Bubble Phenomena

Examples of partial discharges are shown in Figures 21–23. The current waveform and the integrated charge are plotted in the upper two panels and the associated photograph is shown below. The circular interference rings in the photographs apparently arise at the camera image tube. To emphasize the temporal relationship between the current waveform and the photographic data the frame exposures are

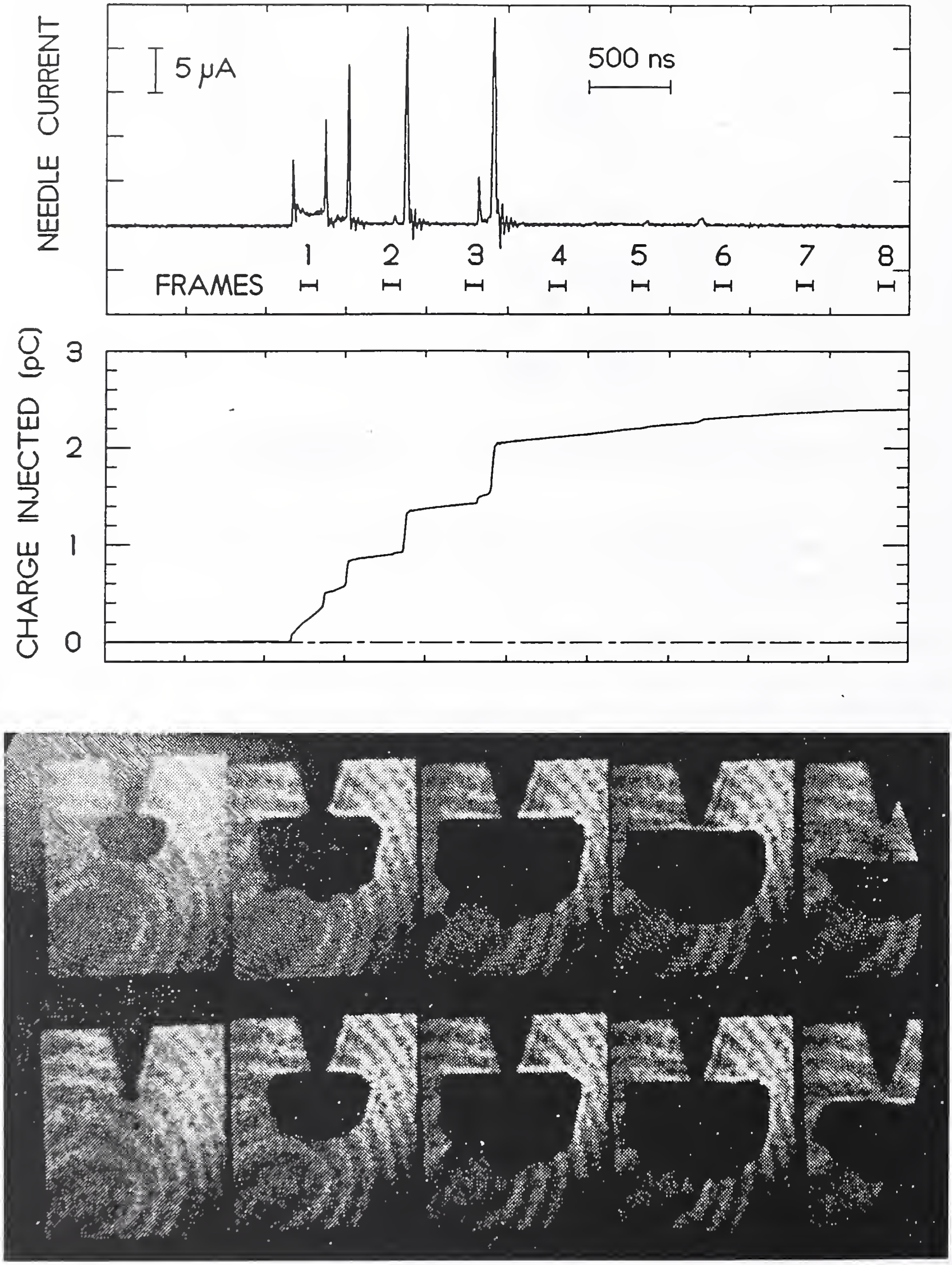

Figure 21. Partial discharge record with camera frame interval of 512 ns and needle voltage of 15.5 kV.

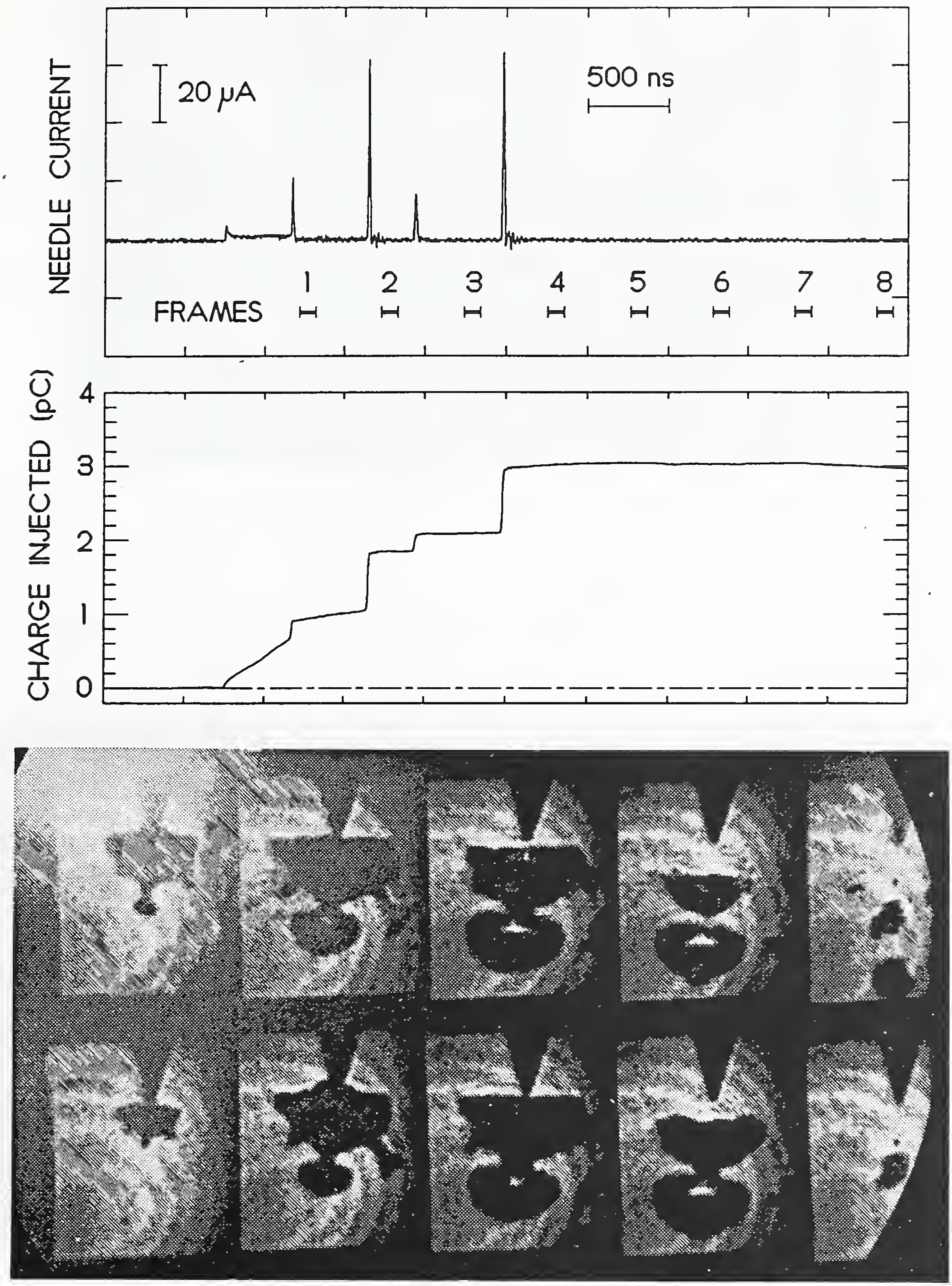

Figure 22. Partial discharge record with camera frame interval of 512 ns and needle voltage of 15.5 kV.

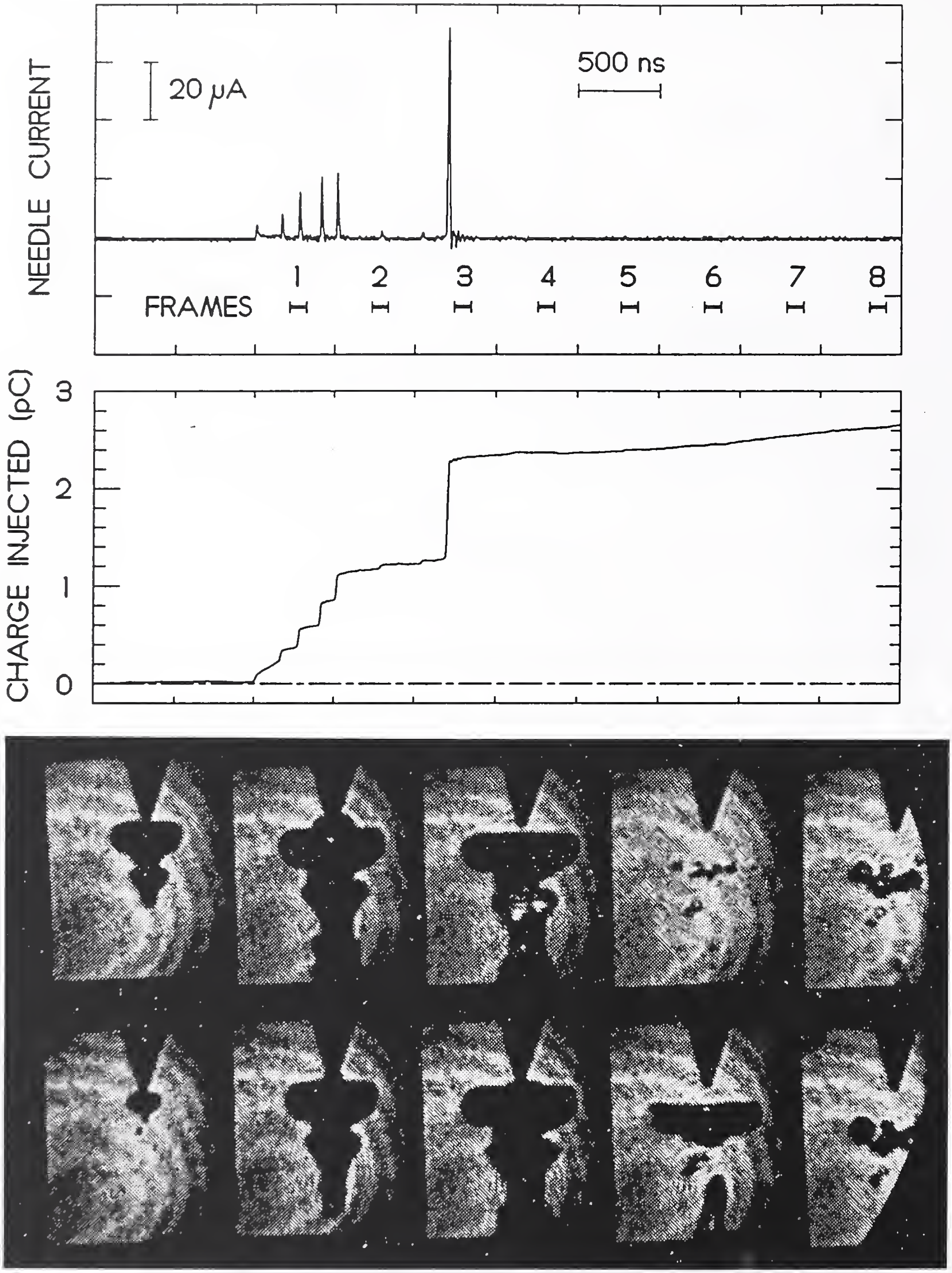

Figure 23. Partial discharge record with camera frame interval of 512 ns and needle voltage of 15.5 kV.

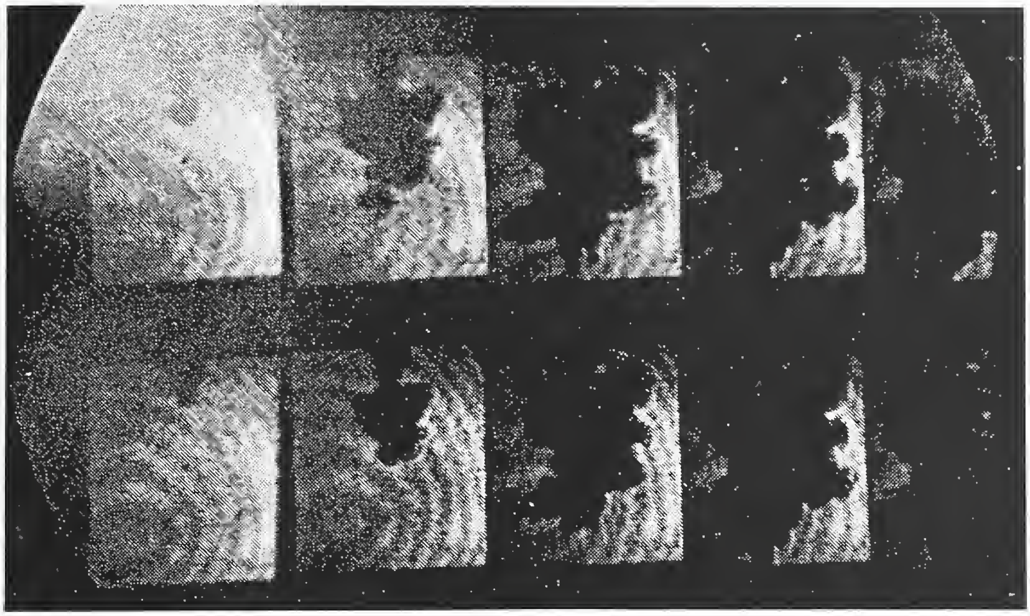

Figure 24. Frame sequence with 217 ns between each frame. The needle has a tip radius of approximately 3 μm. The applied voltage is 17.5 kV.

also shown in the upper panel. The frame interval is 512 ns and the exposure is 102 ns, and these data are obtained at a 15.5 kV potential.

In the photographs shown, the initial bubble is nearly hemispherical. Melcher shows field-induced liquid-liquid instabilities which have similar shapes [78]. The bubble detaches from the needle, breaks apart and collapses. The oscillation during their collapse is typical of cavitation [73, 80]. The collapsing bubble moves away from the tip at approximately 13 m/s. The dynamical behavior of these structures is particularly intriguing. In Figure 22 three instabilities are observed on the primary bubble surface. The center instability grows while the other instabilities are depressed, suggesting field grading due to the charge on the center bubble. Figure 23 shows a chain of bubbles and is a commonly seen structure. In general, the structure becomes irregular sooner and smaller bubbles are produced at higher applied voltages. An example is shown in Figure 24, and is obtained at a 17.5 kV potential.

At the third frame in Figure 21, 3 pC have been deposited within the structure. The radius of curvature of the structure is approximately 12 μm. Assuming the charge is uniformly deposited on a hemispherical surface, the surface charge density σ is 0.0033 C/m^2. The electric field at the surface E is σ/ϵ, where ϵ is the permittivity. Using $\epsilon = 2\epsilon_0$, yields $E = 187$ MV/m. The pressure at the surface due to the charge is σE. The conditions described yield 620 kPa or over six atmospheres. Clearly, sufficient charge is injected to drive the growth of a bubble. This result lends support to the model proposed by Alexeff, et al. [79] for the growth of a partial discharge.

The structure at the initiation of the current waveform had not been resolved in previous studies. In Figure 21, there is a non-zero current between the first and

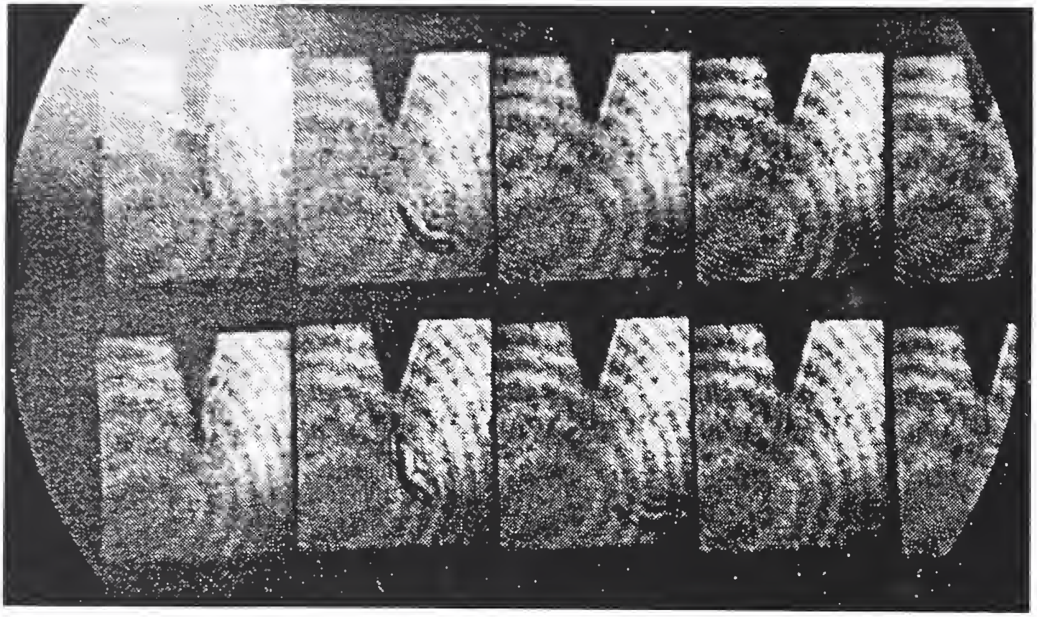

Figure 25. Particle touching the tip and moving away. The frame interval is 512 ns and the applied voltage was 13.5 kV.

second pulses. The current between the first two pulses appears in over 90% of the current traces. Indeed partial discharges are observed which consist of only the double-pulse structure. Occasionally a small series of pulses occurs at initiation. Single pulses are also observed, but no evidence of bubble growth could be seen in the associated photographs.

3.2.3 Search for Involvement of Particles

In general, particles were not visible at the inception of the partial discharge. Photographs are obtained which show particles touching the electrode, however, these did not typically lead to a partial discharge. A unique photograph showing a particle touching the needle and the growth of a bubble is given in Figure 25. However, the structure differs significantly from that described above. Furthermore, the total charge was approximately 100 fC, atypical of the partial discharges discussed above. However, the quality of the photographs obtained with the fast frame intervals is poor and it is difficult to rule out the possibility of particle initiation.

3.2.4 Conclusions

Highly resolved photographs of the initiation of partial discharges in liquid n-hexane have been obtained. Their bubble nature is clear, and the growth of the low density streamer due to electric pressure and the onset of surface instabilities is suggested.

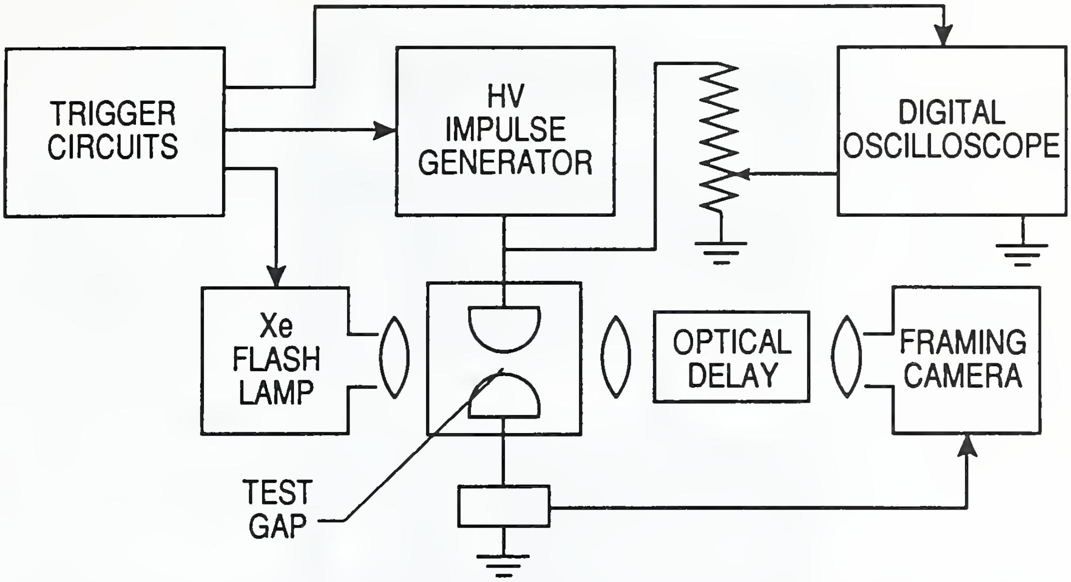

Figure 26. Schematic of the experimental apparatus.

No direct evidence for the initiation of a partial discharge by a particle is found and the role of particulates remains uncertain.

3.3 Streamer Statistics Under Uniform Field Conditions

Much progress has been made in describing the propagation of streamers in liquid dielectrics. The effect of differing materials, pressure and additives on electrical breakdown have received thorough investigation [82]. In liquid hydrocarbons, distinct modes of propagation are observed for both anode and cathode streamers [83]. The speed of propagation of the cathode streamer at its inception differs dramatically from that at its final stage of growth and suggests significantly different propagation mechanisms. Yet very little is known of the material or experimental conditions which are important to the transition to the fast propagation.

The methods employed in the present study allow a photographic record of the conditions which exist in the liquid prior to electrical breakdown to be obtained for each breakdown. Such data allow systematic investigation of dielectric breakdown.

3.3.1 Experimental Methods

The results discussed below are obtained for quasi-uniform fields. As shown in Figure 26, a high voltage impulse is applied to a test gap and a record of the voltage waveform and fast-framing photographs of the breakdown are obtained concurrently. The refractive index of prebreakdown streamers differs from that of the

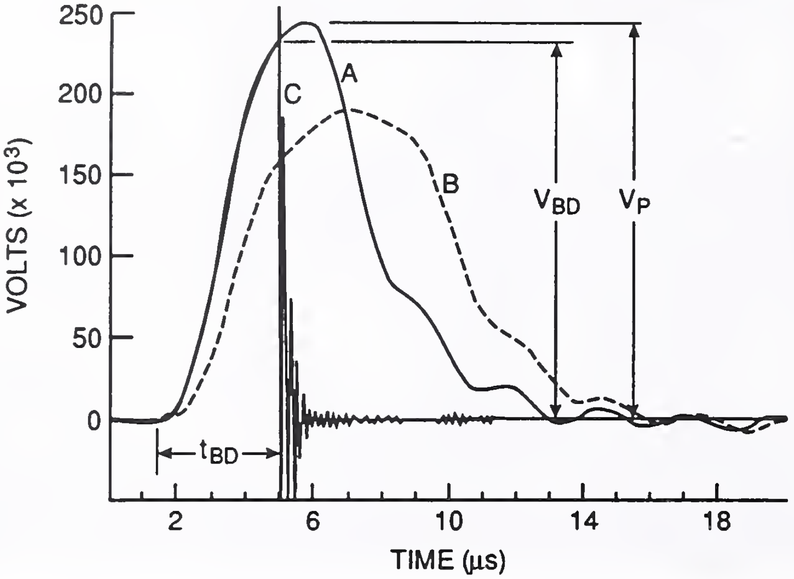

Figure 27. Representative voltage waveforms. The fast and slow impulse waveforms are plotted in curves (A) and (B), respectively. The peak voltage V_P, breakdown voltage V_{BD}, and breakdown time delay t_{BD} are also shown. A typical breakdown waveform is plotted in curve (C).

bulk liquid, thus allowing the shadow of the streamer to be recorded photographically. Frame photographs of the prebreakdown streamers provide a detailed record of their temporal development and are the basis for the assignment of the breakdown mode discussed below.

The test gap is composed of two stainless steel electrodes having 1.27 cm radius of curvature and spaced at 3.0 mm. The gap is enclosed within a cell filled with the liquid of interest. Windows are provided in the cell through which the test gap is photographed. A xenon flashlamp provides illumination during application of the HV impulse.

Ultra-pure n-hexane is employed in this study. The liquid is used as received without further degassing or purification. To prevent the accumulation of particulate material, the fluid is circulated and filtered through a 2 μm pore filter after each breakdown.

The impulse voltage is produced by a simulated transmission line and an impulse transformer. The peak voltage and the rate of rise are controlled by the configuration of the pulse forming network and by varying the charging voltage. Two voltage waveforms were employed for these studies and are shown in Figure 27. A fast impulse is shown in curve (A) and in curve (B) the slow impulse is plotted. The curves shown are obtained for the same charging voltage. A typical breakdown waveform is shown in curve (C). The breakdown time delay, t_{BD}, breakdown voltage, V_{BD}, and peak voltage, V_P, are measured by means of a resistive divider and digital oscilloscope.

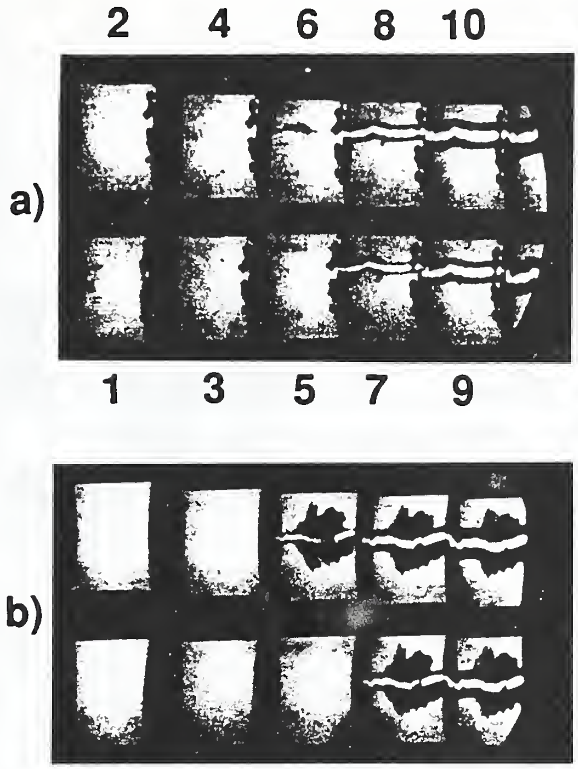

Figure 28. Frame photographs for cathode (a) and anode (b) mode breakdown. The frame sequence is indicated in (a). The frame interval and exposure times are 50 and 10 ns, respectively.

An image-preserving optical delay [75] is used in conjunction with the framing camera. As shown in Figure 26, the framing camera is triggered by the breakdown current; however, since the optical delay (~ 400 ns) is greater than the trigger delay of the camera (~ 105 ns), conditions within the gap which precede breakdown are photographed. Since the prebreakdown phenomena are photographed for every breakdown, a systematic examination of streamer development is possible.

3.3.2 Streamer Morphology

Examples of dielectric breakdown are shown in Figure 28. The photographs are obtained under identical experimental conditions. The nominal frame interval and exposure times are 50 and 10 ns, respectively, and the frame sequence is shown in photo (a). In all of the photos the anode surface is on the left.

Two distinct modes of breakdown are evident in the photographs. In Figure 28a breakdown follows soon after the propagation of a cathode streamer across the gap. The morphology of the cathode streamers observed here is similar to that reported for nonuniform fields [83]. During their early growth, cathode streamers

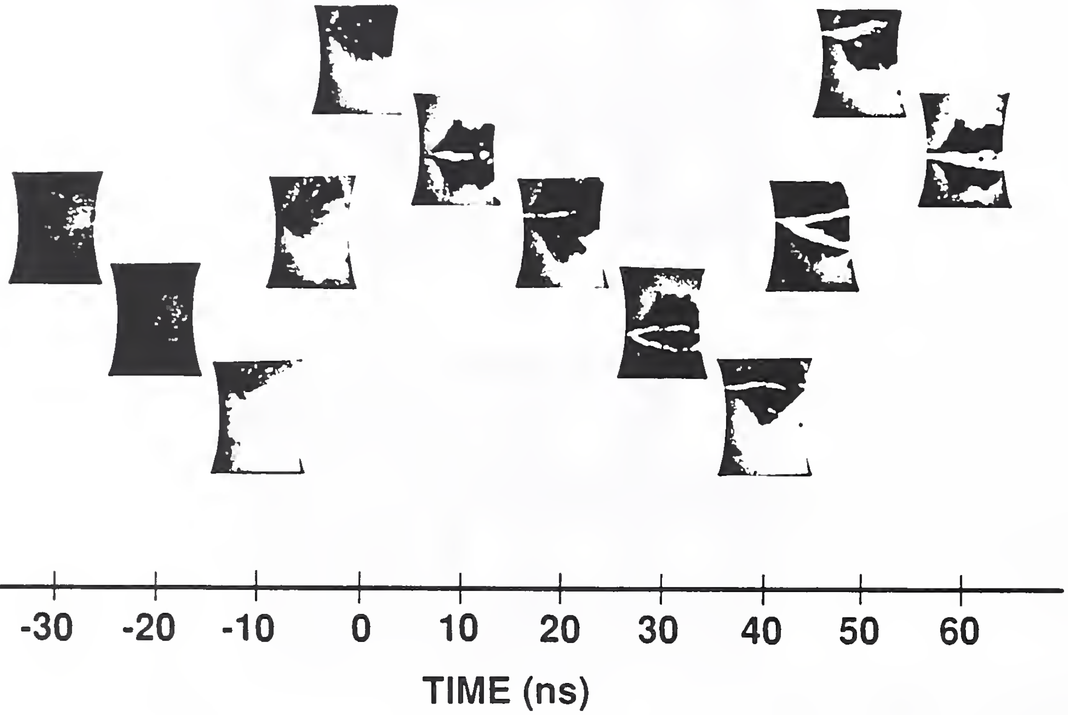

Figure 29. The temporal development of the anode streamer is shown. These photos are obtained by varying the camera delay by increments of 0, 5, 10, 20, 30, and 40 ns. Frames separated by 50 ns are from the same photograph. The time zero is by reference to the first evidence of a breakdown channel.

have a characteristic bush structure and propagate at subsonic speeds. Cathode bush structures are clearly evident at multiple sites along the electrode surface. The presence of the primary cathode bush is necessary to but not sufficient for breakdown by a cathode streamer. In the present experimental conditions breakdown is initiated by a fast growing, supersonic, secondary streamer which originates at one of the bush structures.

Although the temporal development of the prebreakdown streamer is not resolved in Figure 28b, the form of the disturbance surrounding the breakdown channel suggests that the initiating streamer originated at the anode. Under uniform field conditions anode streamer propagation is rapid and it is difficult to capture the temporal development of the prebreakdown streamer even at the fastest framing rates. However, a record of the anode streamer may be constructed by interleaving photographs obtained at differing camera time delays; such a record is shown in Figure 29 where the camera delay is increased by increments of 5, 10, 20, 30, and

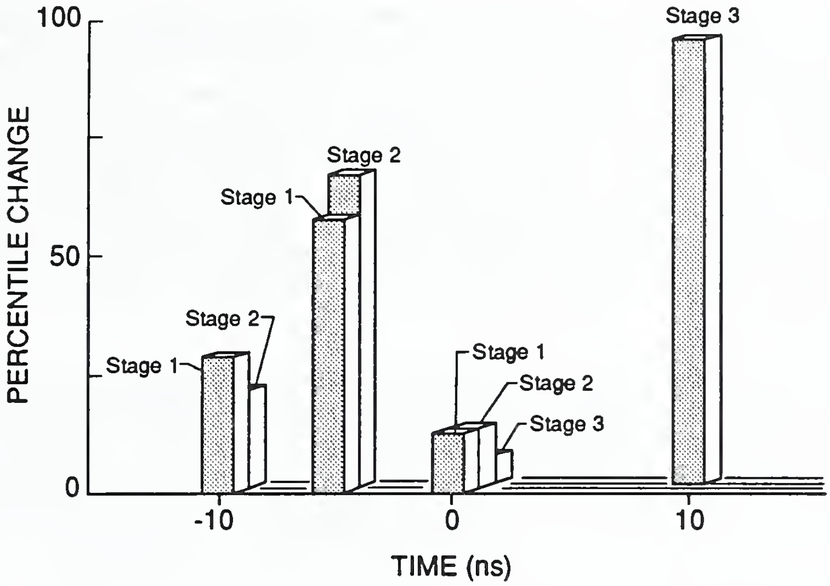

Figure 30. The percentile change in the incidence of anode stage 1, stage 2, and stage 3. The times indicated correspond to those in Figure 29.

40 ns. Frames shown in the figure separated by 50 ns are taken from the same photo.

The photographs shown in Figure 29 are obtained for the fast impulse voltage. The rise time of the impulse is 2.2 μs (10–90%) and the peak voltage is 250 kV. The breakdown probability determined from a sample consisting of 25 trial pulses at each time delay is 81%. The mean time delay and breakdown voltage are 4 μs and 194 kV, respectively. The time zero indicated in the figure is by reference to the first evidence of the main stroke.

The morphological stages evident in the anode streamer development are similar to those reported for nonuniform fields [83]. At the earliest times, a single linear streamer extends from the anode into the gap, stage 1. The single filament undergoes an abrupt transition to what appears to be densely packed nearly linear filamentary streamers, stage 2. The streamers in the second stage of growth lie within a roughly conical volume with its apex on the line of the initial streamer. The mean apparent length of the first stage streamer at the transition is 0.4 mm with $\sigma \simeq 0.1$. The conducting arc, stage 3, develops after the streamer has propagated across the gap.

The temporal development of the anode streamer is summarized in Figure 30 where the percentile change in the presence of each growth stage is plotted. The gap appears to be completely clear of anode streamers 30 ns before breakdown. The data at hand allow an estimate of the average speed of propagation and yield 1.0×10^7 cm/s.

Previous studies have shown the conductivity of the cathode streamers to be significantly higher than that of the bulk liquid [87]. This observation may have significance to the anode streamer propagation. If it is assumed that the anode streamer is a conductor of radius 20 μm projecting into the gap 0.4 mm, a numerical calculation [84] shows that the field at the streamer tip is enhanced by a factor of 18. The mean electric field within the gap just prior to breakdown is of the order of 650 kV/cm. Thus, the field at the tip of the anode streamer may reach levels sufficient for field assisted ionization processes to become significant, and suggests that the transition to the more densely packed streamers appearing in the second stage may be driven by such effects. It is noteworthy that the secondary cathode growth proceeds from a much shorter primary streamer and that the corresponding fields are much lower.

The temporal and spatial descriptions of the anode and cathode initiated breakdowns are distinct and the mode of breakdown may be readily determined from the photographs. We make reference here to each as the anode or cathode modes. In the remainder of this section, several tests undertaken to identify the experimental conditions which influence the relative probability for each mode are discussed.

3.3.3 Results and Discussion

The influence of the voltage waveform and peak voltage were examined first. Using the fast impulse, the peak voltage was varied from threshold to that sufficient for 100% breakdown. Within these limits, the incidence of the cathode-initiated breakdown is 2% and is independent of V_P. For the slow waveform the cathode mode fraction is found to be approximately 12%, significantly larger than for the fast pulse. However, the anode mode is predominant for both waveforms. This observation may be anticipated from results for n-hexane obtained in a nonuniform field which show breakdown strengths for a point anode to be less than those for a point cathode [85]. The initial stages of cathode streamer growth are, however, clearly evident in 66% of the photographs.

To date, the accumulation of breakdown byproducts within the liquid has been found to have the most dramatic effect on the breakdown mode. To test for the influence of byproducts, the liquid was not circulated or filtered and was subjected to numerous breakdowns. The results of these tests are summarized in Figure 31 where the breakdown probability and the cathode-mode fraction are plotted as functions of the number of breakdowns. Data obtained for both the fast impulse waveform and the slow impulse are shown.

The conditions which influence the transition to fast growing cathode streamers are not well understood. It has been suggested that the transition may be more likely at high overvoltages [86]. However, these results suggest that the probability for the formation of the secondary cathode streamer is more likely for the slow pulse at low peak voltage and that the cathode-mode fraction is increased by the presence of particulate material in the liquid. A dramatic increase in the breakdown probability with the accumulation of breakdown byproducts is also noted.

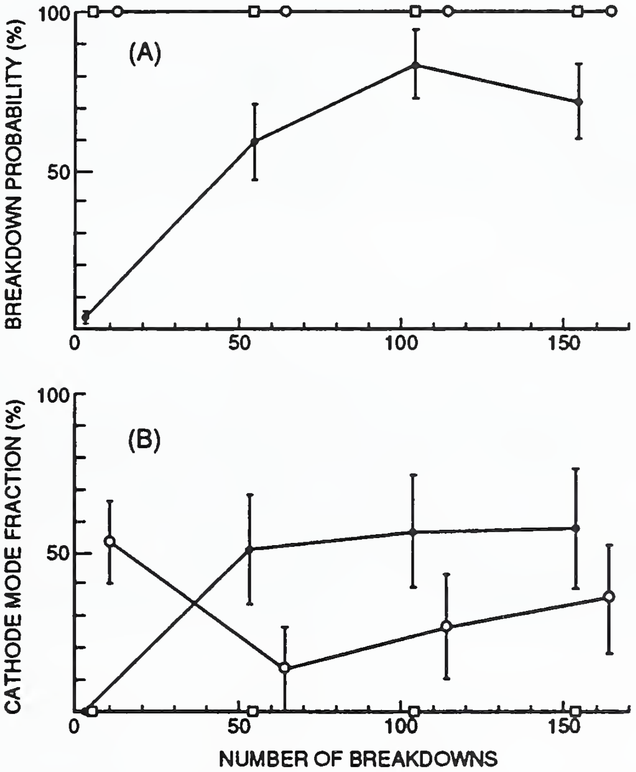

Figure 31. The breakdown probability and cathode mode fraction are plotted as functions of the total number of breakdowns. Data for the fast impulse □, peak voltage of 280 kV; and for the slow pulse, peak voltages of 220 kV ○ and 190 kV ● are plotted.

An observation made during the course of these tests may be relevant to the methods employed in dielectrics testing. It was noted that if the gap did not break for a given pulse, the probability that the next voltage impulse produced breakdown is significantly less than would be anticipated for statistically independent trials. One may test the hypothesis that breakdown occurs independently of the result of the previous pulse by comparing the observed and expected number of successive pairs: breakdown - no breakdown. A sequence of N independent trial pulses in which the probability of breakdown at each trial, P_{BD}, is fixed is described by a binomial distribution [88]. The sample summarized in Figures 28 and 29 consisted of $N = 150$ trial pulses and the expected number of such pairs is $N(1 - P_b)P_b \simeq 23$ with $\sigma \simeq 4$; however, 11 pairs are observed. The probability that this difference arises by chance is $< 1\%$; it is therefore unlikely that the sequence is random. It has been suggested that n-hexane polymerizes under electrical stress [89]. The formation of a polymer layer on the electrode surfaces would clearly contribute to the breakdown strength. The apparent nonrandom breakdown behavior observed in the present work may be consistent with such effects.

3.3.4 Conclusions

Methods has been developed which allow systematic study of prebreakdown streamers in liquid dielectrics. In uniform fields under impulse conditions, breakdown may be initiated by either anode or cathode streamers. The relative probability for each mode of breakdown depends on the voltage waveform and is highly dependent on the presence of particulate material in the liquid. The variability observed in previous breakdown studies can be understood, in part, as a consequence of this underlying mechanism of mode selection.

4 FAST TRANSIENT MEASUREMENTS

Task 04

Yi Xin Zhang (Guest Scientist), Edward F. Kelley (Consulting Scientist),
and Gerald J. FitzPatrick
Electricity Division
National Institute of Standards and Technology

4.1 Introduction

The objective of this task is to provide measurement support for the DOE research program on the effects of fast electrical transients on electric power equipment and systems. Facilities and techniques are developed and maintained to calibrate and evaluate devices used in the measurement of fast electrical pulses. These fast transients in electrical power systems occur during normal operation or are induced by lightning strikes and can result in equipment failures and power outages [90, 91]. Precise measurement of fast transient voltages is then critical in the evaluation of their effects on electrical power equipment and insulation in order to improve system reliability. For correct analysis of transient voltage effects on apparatus or dielectrics, the peak voltage and waveshape must be accurately known. In addition, accurate measurements of high voltage transients in pulse power machines are necessary for monitoring and maintenance of proper system operation [92].

This report documents the results of efforts to improve the measurement precision of two types of high voltage measuring devices: electro-optic Kerr cell systems and resistive high voltage dividers. These two types of systems rely on very different measurement technologies. The voltage divider samples a fraction of the input voltage that is easily measured with an oscilloscope or digital recorder. The divider must have a physical size large enough to withstand the full voltage yet must also have the wide bandwidth necessary to scale microsecond and submicrosecond high voltage transients without distortion. Additionally, the voltage recorder (oscilloscope or digital recorder) must have sufficient resolution to measure the fast waveforms. Kerr cells, on the other hand, are electro-optic transducers whose optical transmission properties are dependent on the applied voltage. They are inherently fast because their response primarily depends on the molecular reorientation times of their liquid dielectric, which is subnanosecond [93], but a limitation on the temporal response of the measurement system is imposed by the photodetector used to measure the transmitted light.

Improvements in both types of measurement techniques have been made. A study of the response of different types of photodetectors has been conducted to optimize the operating conditions of the detector that give the greatest measurement linearity. Secondly, an improved measurement method, known as the Pulse Level Line (PLL) technique, has been developed and tested with resistive dividers that

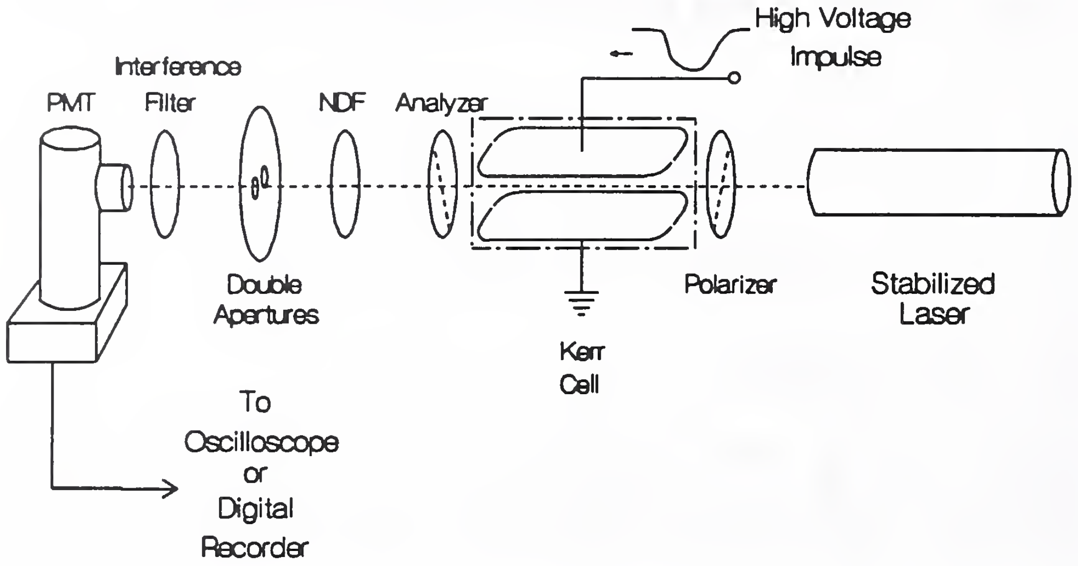

Figure 32. The Kerr Electro-Optic Measurement System. The basic system consists of a light source, crossed polarizers, Kerr cell, photodetector, and oscilloscope or digital recorder. The neutral density filter (NDF), interference filter, and double aperture screen are used for linearity tests described in the text.

reduces peak voltage measurement uncertainties to 0.1% or less. The results of the photodetector study are reported in the next section and the PLL technique is described subsequently.

4.2 Optical-Electrical Detector Linearity

A Kerr cell measurement system is an electro-optic transducer whose optical properties change with applied voltage. The Kerr cell and major components of the optical detection system are diagrammed in Figure 32. The double aperture element is used only for the linearity testing later described in section 4.2.4. The system consists of a light source, a Kerr cell with polarizers at its input and output, a light detector, and a voltage recorder. The Kerr cell is basically a parallel plate capacitor connected to the high voltage circuit at the point where the voltage is to be measured. It contains an optically active liquid such as nitrobenzene which becomes optically anisotropic when a voltage is applied to the plates. The electric field between the plates induces a difference between the indices of refraction (birefringence) along the axis parallel to the electric field between the plates and that perpendicular to it. The incident light first passes through a polarizer whose axis is oriented at 45° to the axis parallel to the field between the plates so that at the entrance to the Kerr cell the light is linearly polarized with components both perpendicular and parallel to the electric field between the plates. The birefringence introduces a phase delay

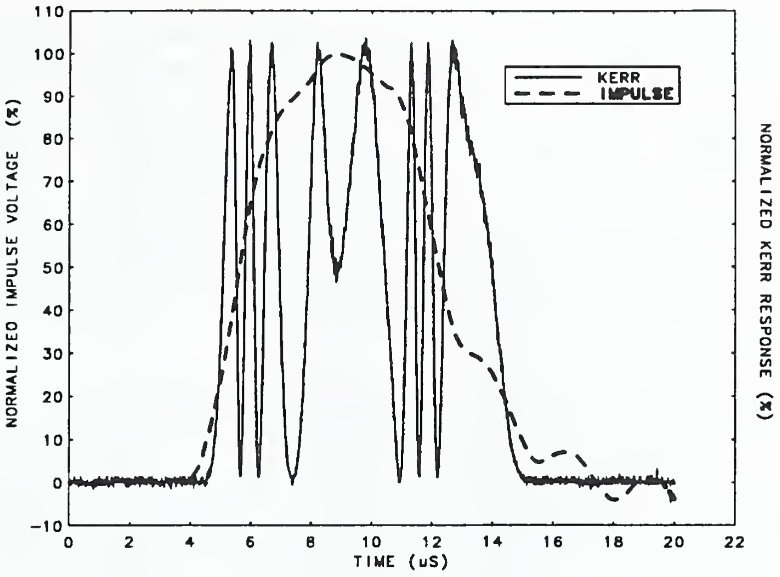

Figure 33. Kerr Measurement System Output Signal. The sinusoidal variation in light intensity produced by the Kerr cell and polarizers as measured by the photodetector and shown with the applied voltage measured by a precision high voltage divider for comparison.

between these components of the incident beam as they pass through the cell and the resultant polarization at the output of the cell is changed from that at the input. The optical axis of the second polarizer (analyzer) is oriented perpendicular to that of the first and in the absence of any applied voltage passes very little of the incident beam. As the applied voltage increases, the induced change in the polarization of the beam as it passes through the cell causes more and more of the beam to be passed by the analyzer until the transmission is maximized. Further increases in the applied voltage causes less and less light to be transmitted until minimum transmission is reached. As the voltage is increased even further, the light transmission increases again as the cycle is repeated.

The response of the photodetector to this variation in light intensity consists of a sinusoidal oscillations, as shown in Figure 33. The associated voltage trace is shown for comparison. The frequency of the oscillations in light intensity is determined by the rate of rise of the applied voltage and the Kerr cell constant, a parameter fixed by the cell geometry and Kerr electro-optic coefficient of the liquid. The relation of output light intensity to applied voltage for an ideal Kerr measurement system is given by

$$I/I_m = \sin^2(V/V_m)^2 \tag{18}$$

where I is the measured light intensity, I_m is the light intensity at maximum transmission, V is the applied voltage, and V_m is the Kerr cell constant [94]. The applied voltage waveform can be reconstructed from the measured light intensity by solving this equation for V.

The precision of the Kerr measurement depends upon several system parameters such as the dynamic response of the Kerr cell, the stability of the Kerr liquid, the response of the photodetector, and the bandwidth of the voltage recorder that measures the photodetector output. In general, the Kerr cell response is more than adequate for the measurement of submicrosecond transients as is the voltage recorder bandwidth of the oscilloscopes and digital recorders used. The Kerr liquid is reasonably stable and changes in the Kerr response due to variations in cell temperature are well-compensated. This report focuses on the work conducted in improving the response of the photodetector in order to improve the measurement precision.

To maximize the precision of a Kerr cell measurement system, the linearity of the optical-electrical detector must be calibrated and maintained within a precision of 1% or less. The effects of nonlinearity in the Kerr measurement are seen in Figure 34a which shows the response of the Kerr system to the voltage pulse shown in Figure 35a. The curve superimposed upon the measured curve is that calculated from the applied voltage measured by a precision standard voltage divider and using equation 18. The curves are normalized to emphasize the difference in their temporal responses. Figure 34b shows the difference between the normalized curves which is greatest near their maxima and minima where the photodetector has the greatest nonlinearity. The voltage curve reconstructed from the Kerr measurement is shown in Figure 35a compared with the measured voltage divider output. The distortion due to photodetector nonlinearity is evident in the difference of the reconstructed and measured voltage curves shown in Figure 35b.

Three test methods were investigated to optimize the operating condition for the photodetector in order to make the detector output more linear. These methods are described in the following sections.

4.2.1 Photomultiplier Tubes (PMT) and Linearity Tests

Because of secondary-emission multiplication, photomultiplier tubes (PMT's) are uniquely sensitive compared to other photosensitive devices currently used to detect radiant energy in the ultraviolet, visible, and near infrared regions. They have much higher amplification factors than photodiodes and also feature fast responses and low noise, which are critical for precise Kerr electro-optic measurements. PMT linearity depends upon such factors as the load resistance, supply voltage, and incident light intensity.

Since the output of a photomultiplier tube is a current signal and external circuits to which photomutiplier tubes are usually connected require voltage inputs, a load resistance is used to perform the current-to-voltage transformation. The theoretical equation for cutoff frequency f_c that limits the PMT response is:

$$f_c = \frac{1}{2\pi C_s R_L} \tag{19}$$

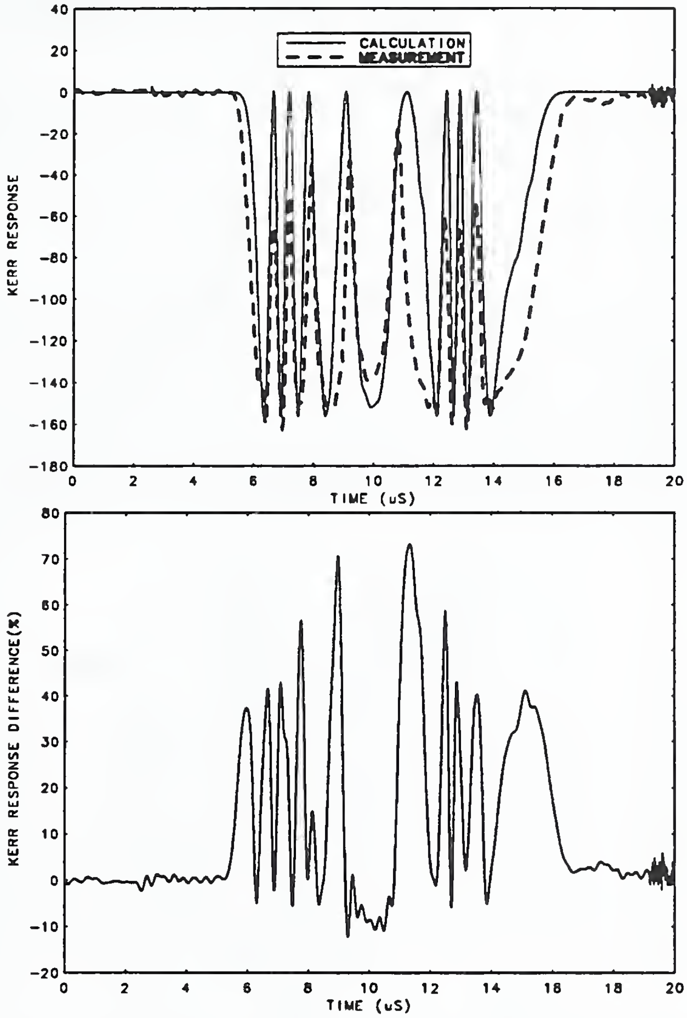

Figure 34. Ideal and Actual Kerr Measurement System Output Waveforms. (a) actual measured Kerr system waveform and ideal waveform calculated from Eq. 18 using the applied voltage measured by a precision high voltage divider. (b) difference of actual and ideal waveforms of (a).

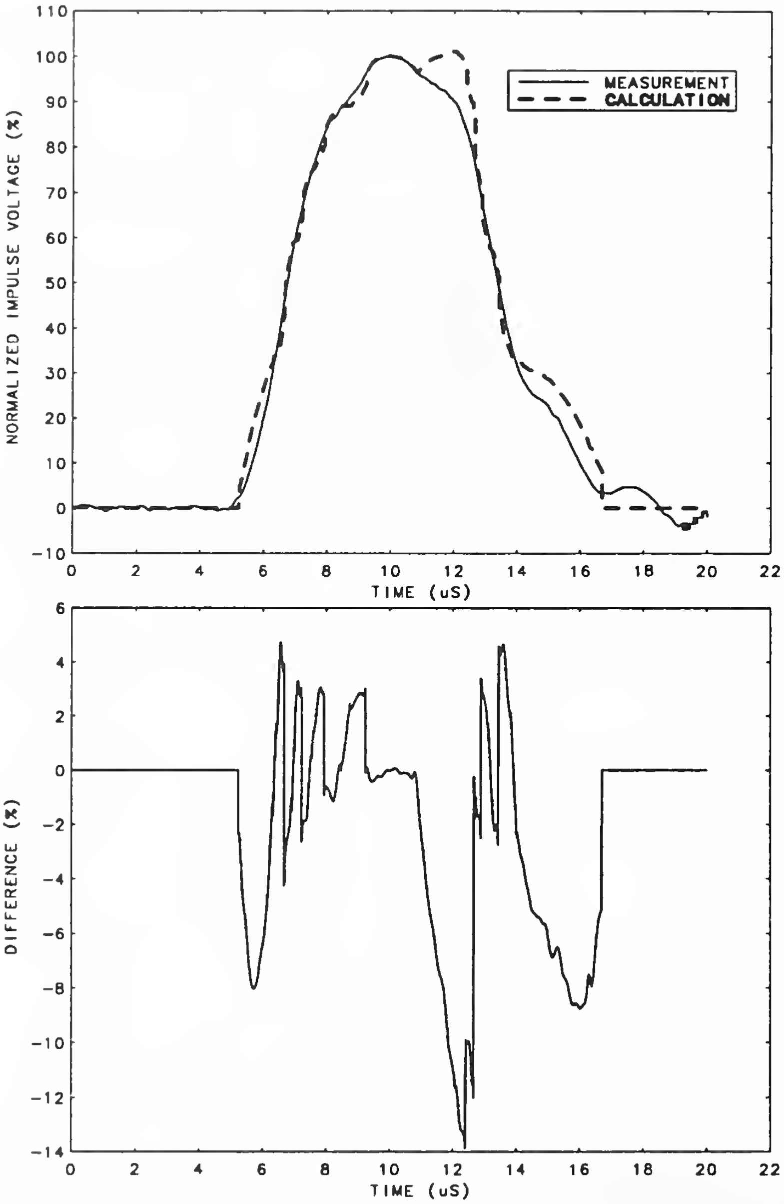

Figure 35. Measured and Calculated Voltage Waveshapes. (a) comparison of voltage waveshape measured by a precision high voltage divider and that calculated from measured Kerr system output. The waveforms are offset for clarity. (b) difference of actual and calculated waveforms of (a).

where C_s is the total capacitance of the photomutiplier anode to all other electrodes and includes such stray capacitance as wiring capacitance, and R_L, is the load resistance. The output linearity, which depends upon a relatively constant frequency response over the range of frequencies for which the input signal has significant components, is degraded if f_c is too low because of a large R_L. It can be seen that using very large values of load resistance degrades the frequency response and output linearity, even if the photomutiplier tube and amplifier have a very fast response.

If the load resistance is made large, the voltage drop across R_L also becomes large at high current levels. This lowers the efficiency of the anode in collecting electrons and, in effect, the output becomes saturated above a certain current level, resulting in a loss of linearity. For these tests, the load resistance, R_L, was $50\,\Omega$ and an external amplifier was connected to the photomultiplier to increase the signal amplitude.

Two types of photomultipliers were used in this study: one which had high stability and another having high sensitivity. The former had a very low dark current but the latter had a much higher anode luminous sensitivity. Three different test circuits and methods were used to examine the linearity of the photomultiplier tubes. The first two test techniques rely upon the linearity of the light source and accuracy of the attenuation factors of the optical elements while the third approach depends only upon the stability of the light source. The three methods are discussed in the following sections.

4.2.2 LED-PMT System

In the first test setup, a light-emitting diode (LED) was used as the light source to test the linearity of the PMT output for various input light intensities. The diagram of the test configuration for the LED-PMT system of Figure 36 shows the dc power supply connected to the LED by a mercury-wetted relay which is driven by a function generator. The closure time of the relay is a few nanoseconds. The response of the PMT to two different types of input waveforms signal sources contained significant distortions, as shown in Figures 37 and 38.

The difficulty with using this test configuration is that it does not clearly identify the cause of the distortion of the output waveform. Both the LED and PMT are nonlinear components of the system and the nonlinearity cannot be conclusively traced to either based solely upon the measured LED driver and PMT output waveforms. The effect of PMT supply voltage on response characteristic linearity (PMT output vs. maximum LED input voltage for a voltage step input) is seen in Figure 39, which indicates that this response characteristic becomes increasingly nonlinear with increasing PMT power supply voltage, but again, the nonlinearity may be in the LED as well. In order to more closely approximate actual operating conditions, a linearity test was performed in an actual Kerr measurement system configuration and is described in the next section.

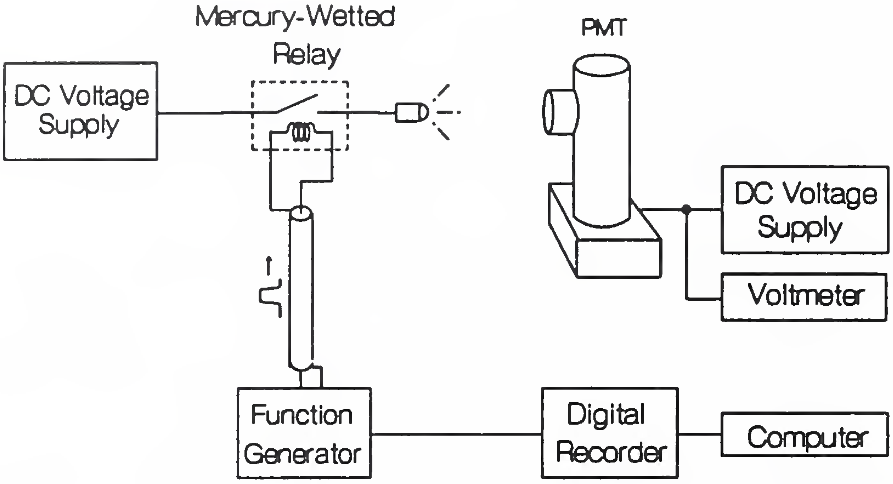

Figure 36. Test Configuration for Evaluation of PMT Linearity with LED. The function generator drives the mercury-wetted relay which connects the dc voltage supply to the LED. The system is used to produce light intensity variations of various amplitudes and durations.

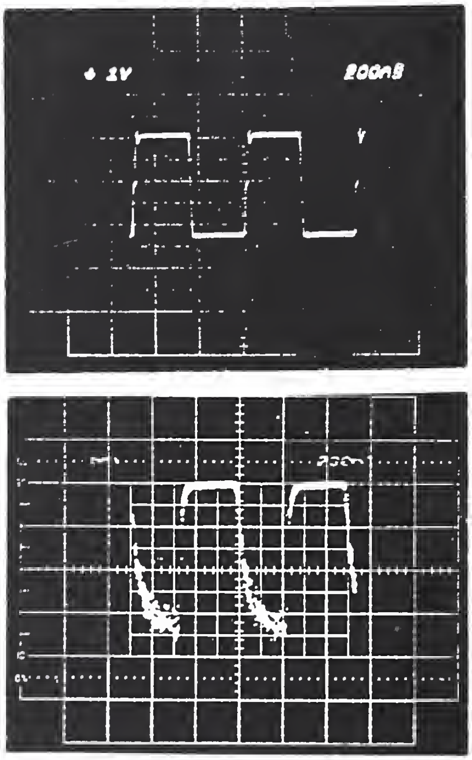

Figure 37. Response of LED-PMT System to Square-Wave Voltage Input. (a) LED input voltage. (b) PMT output.

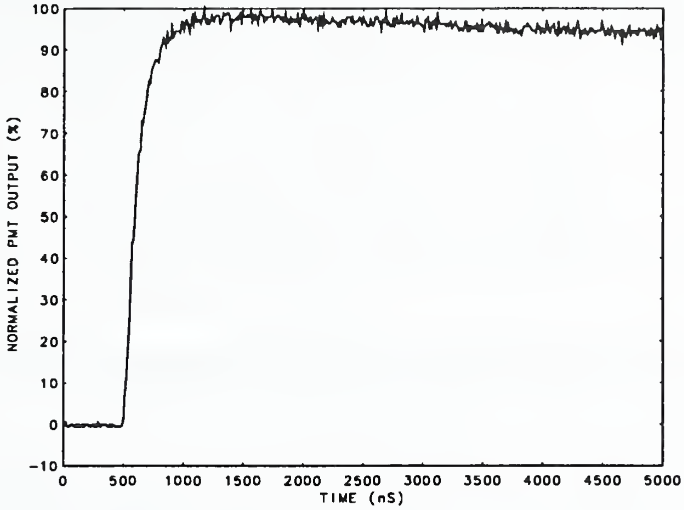

Figure 38. Response of LED-PMT System to Voltage-Step Input. The output of the PMT has relatively fast risetime followed by a very slow decay.

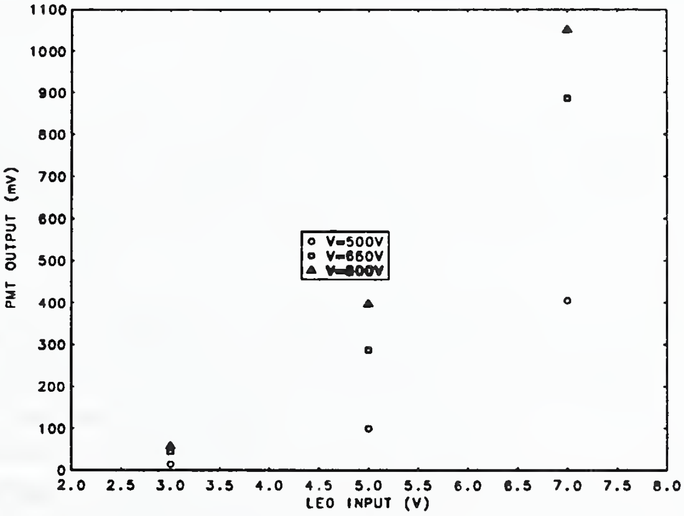

Figure 39. PMT Response for Different Supply Voltages. Dependence of PMT output on voltage input to LED. The source of the measurement nonlinearity (LED or PMT) is not clearly identified. Deviations from linearity increase at larger PMT supply voltages.

Table 4. Nonlinearity of PMT Tested with NDF's (%)

Neutral Density Filter Attenuation Factor (%)	Supply Voltage of PMT(V)				
	360	**375**	**400**	**500**	**600**
67.5	0.6	0.7	2.6	2.2	8.7
45.1	0.2	0.5	1.8	0.6	11.0
20.9	-0.5	0.2	0.7	2.4	6.5
7.9	-0.3	0.0	0.4	3.2	1.9

4.2.3 Linearity Determination of the Kerr Cell Optical System With Neutral Density Filters

To test the linearity of the Kerr cell system, the test circuit of Figure 32 was used. The laser beam is modulated by the Kerr cell and polarizers, to which a high voltage impulse of the type shown in Figure 35 was applied and neutral density optical filters were used to attenuate the light intensity incident upon the PMT to different levels. The nonlinearity, N, of the PMT was calculated as defined in the following expression:

$$N = (I_m - I_c)/I_0 \times 100\% \tag{20}$$

where I_m is the measured light intensity maximum of the modulated beam, I_0 is the light intensity measured without the NDF, and I_c is the light intensity calculated by multiplying I_0 by the attenuation factor of the NDF. A 15 mW argon ion laser and a 1 mW output stabilized Helium-Neon laser were used. It was found that the 15 mW laser could not be used for precision measurements with the Kerr cell system because variations in its output intensity did not provide a constant modulation envelope over the microsecond time windows necessary for impulse measurements; the highly-stabilized and lower power laser was necessary to obtain the constant-intensity light necessary for precision measurements with the Kerr cell system.

To further test PMT linearity, lower PMT supply voltages were used, but at these lower voltages and relatively low light intensities, the PMT output amplitude is too small to be directly measured by an oscilloscope. However, when the supply voltage level is increased above 500 V, the PMT output increases but the nonlinearity becomes significant. One solution is to use an external amplifier with the lower supply voltages, but using such an amplifier introduces noise and bandwidth limitations. An amplifier having a DC-250 MHz bandwidth and 5 dB gain was therefore used when the output signal was not large enough to be measured by oscilloscope. Table 4 shows the results of these tests performed at lower PMT supply voltages using nonlinearity as defined by Eq. 20.

The table indicates that the nonlinearity is greatest for the larger PMT supply voltages (400–600 V). The output of the PMT is lower for smaller supply voltages because the tube multiplication factor is lower, but care must also be taken not to saturate the anode, although it may be tempting to use greater light intensity to improve the PMT output amplitude when the lower supply voltages are used.

The disadvantages of relying upon the neutral density filters in this type of linearity test is that the accuracy of their attenuation factors has to be very high, stable, and uniform over a certain area of the filter. The NDF's were tested with a light power/energy meter and the measured attenuation factors were found to differ from their nominal attenuation factors by as much as 3% depending upon orientation with respect to the beam. The PMT results of the linearity tests described here used the measured attenuation factors of the NDF's.

The NDF's do not provide an easy way to determine PMT linearity because their attenuation factors must be determined empirically and have relatively large variation. A simple test method to determine linearity that uses NDF's for a range of light intensities but one that is independent of the NDF attenuation factor is described in the next section.

4.2.4 Kerr System and Double Apertures Calibration

According to the general definition of linearity, a system is considered to be linear when a relationship exists as shown below:

$$F(A+B)=F(A)+F(B) \tag{21}$$

or,

$$\frac{F(A)+F(B)}{F(A+B)}=1 \tag{22}$$

where A and B are two independent variables and F is a function of A and B. A method based on the above definition was used to calibrate the linearity of the PMT detector system using the test configuration as shown in Figure 32 with the double aperture element in place. The screen has two adjacent circular apertures and is placed between the output polarizer of the Kerr cell and the PMT. A narrow-band interference filter is placed at the input of the PMT to block all but the incident laser light. Initially, both apertures A and B are open to permit the laser beams to pass through both of them and its amplitude as modulated by the Kerr cell under impulse voltage conditions, i.e. $F(A+B)$, is measured. Aperture A is then shuttered and the modulated beam is measured to get $F(B)$. Finally, aperture B is shuttered, A is re-opened and a measurement is taken to get $F(A)$. It is not necessary to know the attenuation factors of the NDF's exactly, provided that the incident light intensities $F(A)$ and $F(B)$ are stable and the measurements are repeatable. Typical results are given in Table 5, where the nonlinearity N' is defined by

$$N'=(\frac{[A]+[B]}{[A+B]}-1)\times 100\% \tag{23}$$

Table 5. Nonlinearity of PMT Tested by Double Apertures Method (%)

Attenuation Factor of NDF (%)	Supply Voltage of PMT(V)		
	360	**380**	**420**
44.7	–	4.6	–
20.9	−0.5	−1.1	2.9
14.1	−0.1	–	–
8.9	0.1	–	–

The highly stable PMT with external amplifier had excellent linearity (N' less than 0.5%) over a range of light intensities when the supply voltage was 360 V. The tests indicated that the PMT linearity was improved by using the lower supply voltages.

4.2.5 Conclusions

Three test methods were performed to evaluate PMT linearity over a range of light intensities. The first two approaches utilized optical neutral density filters to attenuate the laser beam incident upon the PMT, but depended upon the orientation and uniformity of the filters. The uncertainties in attenuation factors of the NDF's contributed to errors in the linearity determination. The third method used two apertures to verify that the measured sum of individual beam intensities passed by each aperture when the other was shuttered equaled the total measured intensity passed when both apertures were open. Although the double aperture technique was tested with a set of NDF's to provide a range of intensities, the attenuation factors of the NDF's do not need to be known accurately to determine PMT linearity. The test is performed under actual operating conditions, where the Kerr cell system, in response to a high voltage impulse, modulates the light beam.

Experimental determination of PMT linearity over a range of light intensities for various PMT supply voltages indicated that there are conflicting restraints on the operating conditions of the measurement system. The first is that the supply voltage be large enough to provide a PMT output that can be amplified and measured without introducing significant noise and distortion. Secondly, it was found that the PMT's had better linearity at the lower supply voltages. In the present study, the optimum PMT supply voltage to provide maximum output signal amplitude and minimal distortion was 360 V for an incident light intensity of about 0.6 mW. The test techniques reported here can be used to easily determine the optimum operating PMT supply voltage and light intensity to maximize precision measurements with the Kerr electro-optic system. Improvements in peak voltage determinations for impulse voltage dividers are described in the next section.

4.3 Pulse Level Line Technique

The Pulse-Level-Line method (PLL) provides a means of measuring the peak voltage of a fast transient pulse with a 0.1% uncertainty or less using conventional analog oscilloscopes, which ordinarily have stated precisions of the order of 1%. The measurement of high voltage impulses with highly stable voltage dividers is consequently improved.

As previously mentioned, oscilloscope uncertainties in measuring the peak of microsecond impulses are typically of the order of 1%. A variety of methods are used to ensure or improve the precision with which the peak of an impulse can be measured. In one technique, known as a slideback measurement, an offset voltage is applied to the storage oscilloscope input and the peak of the impulse is measured relative to a known dc voltage level that is applied subsequent to the impulse. Because the dc level provides an independent voltage reference, it is possible to use a more sensitive vertical scale on the oscilloscope than would be required if a ground line was used as reference. Similarly, in another commonly used method the peak measurement is based upon two accurately known dc levels which are selected to be slightly above and below the peak of the impulse.

The precision of these methods relies upon the assumption that the oscilloscope amplifier circuits respond to the voltage impulse as they do to dc stimulus. If there are slight differences in how the oscilloscope amplifier acts with an impulse as compared to dc, then the above methods may not provide the best accuracy for the peak measurement. To more closely simulate the conditions under which impulse voltages are measured and to avoid any possible problems of amplifier response from dc to impulse, a method has been devised to provide the application of dc levels to the oscilloscope in the form of fast-rising voltage steps. Thus, the amplifier is stimulated by the calibration level lines in a manner similar to the application of the impulse to be measured.

The three traces (impulse voltage and two reference level lines) are recorded sequentially on the screen of the storage oscilloscope and a photographic record, depicted in Figure 40, is made on which the relative positions of the two level lines and impulse voltage peak are physically measured.

In the figure, V_1 and V_2 are the dc voltages associated with the level lines and h_1 and h_2 are their measured locations on the photograph, respectively. V_s is the value of the impulse peak to be determined and h_p is the measured location of the peak. The reference from which the location of the center of the lines h_1, h_2, and h_p are made is arbitrary since it is only the differences between such measurements which enters the expression for the impulse voltage peak V_s:

$$V_s = V_1 + (V_2 - V_1)(h_p - h_1)/(h_2 - h_1). \tag{24}$$

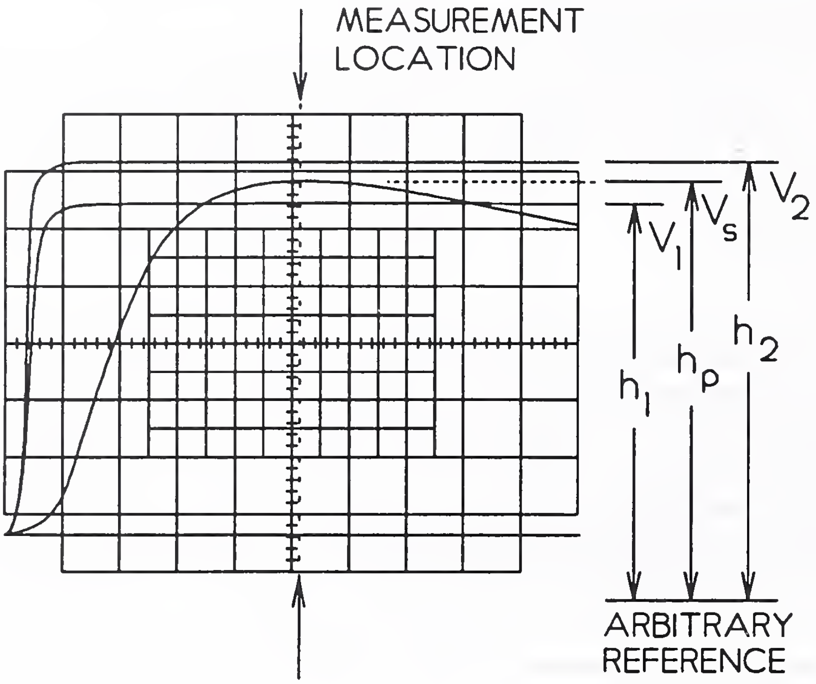

Figure 40. Simulated Photographic Record of the Storage Oscilloscope Screen. The three traces are shown: the impulse voltage measured by a precision high voltage divider, and two reference voltage level lines.

The measurements are made by fixing the photograph on a specially-adapted mount. Although a measuring low-power microscope would be ideal, it is a simple matter to adapt a vernier or dial caliper to perform the position measurements. A magnified crosshair mounted to the traveling arm of the caliper can provide sufficient accuracy since only the relative positions of the three traces is needed. The oscilloscope photograph is positioned so that the level lines are perpendicular to the direction of travel of the caliper arm. The photograph is illuminated along the direction of the level lines to avoid visualization errors associated with shadows from the crosshairs.

The accurate measurement of the position of the peak is often facilitated by using an oscilloscope sweep speed that is magnified by a factor of ten over that which would permit the entire voltage impulse to be measured. For example, if the voltage impulse is ten microseconds in duration on an oscilloscope having ten horizontal divisions, a time scale of one microsecond per division is required to capture all of the impulse waveform. A sweep speed of one hundred nanoseconds per division would be used with the PLL technique to allow the impulse peak to be more easily identified. Since the actual recorded voltage trace is not as thin as that shown in Figure 40, but rather has a finite thickness which is magnified for the measurement, the impulse peak position measurement, h_p (as well as the level line position measurements) is made to the center between the top and bottom edges of the line. If the horizontal width of the peak is too narrow, as it is for longer sweep speeds, it is difficult to determine the exact center of the line.

The oscilloscope settings are adjusted so that the peak and level lines do not overlap the graticule lines, as this makes accurate position measurements more difficult. Additionally, placement of the impulse peak at the corners of the oscilloscope screen is avoided since any screen distortion is usually greatest there. Placing the peak near the top (bottom) of the screen for positive-going (negative-going) impulses and at the horizontal center of the screen usually provides the least distortion. The horizontal position of the impulse peak relative to the start of the sweep is chosen to be at least 8τ, where τ is the charging time constant of the pulse-level-line generator. This ensures that the pulse level line deviates by less than 0.03% from the measured dc charging voltage.

The level lines are placed relatively near the position of the peak in order to improve the measurement accuracy, as seen from the calculation of the measurement error. Assuming a random error δV in the voltage and δh in the position measurements, the total error associated with the resultant peak measurement δV_s is given by

$$\begin{aligned}(\delta V_s)^2 &= (\delta V)^2[(h_2-h_p)^2-(h_p-h_1)^2]/(h_2-h_1)^2 + \\ &\quad (\delta h)^2[(h_2-h_1)^2+(h_2-h_p)^2+(h_p-h_1)^2](V_2-V_1)^2/(h_2-h_1)^4. \quad (25)\end{aligned}$$

Here, the term associated with the position measurement error (δh) increases as the voltage difference between the level lines increases. Usually the voltage measurement is relatively accurate and it is the position measurement error which constitutes the greatest contribution to the overall error. For example, a reasonable estimate of the random error of the position measurement is $\delta h = 0.051$ mm (0.002 inches). Values for the position measurements and dc voltage levels are of the order of $h_1 = 100$ mm, $h_2 = 110$ mm, $h_p = 105$ mm with $V_1 = 10\,V$, $V_2 = 11\,V$. Taking an exaggerated value of $\delta V = 1$ mV for the voltage level error, Eq. 24 yields $V_s = 10.5$ V with an error of $\delta V_s/V_s = 0.0006$ or 0.06% found from Eq. 25. If δV is taken to be as large as 10 mV, then $\delta V_s/V_s = 0.0009$ or 0.09%. Even if the position measurement error is taken to have the unrealistically large value of $\delta h = 0.127$ mm (0.005 inches, which is larger than the line width) the total relative error is only 0.0015 or 0.15%.

The circuit for supplying the pulse-level-lines is shown in Figure 41. A stable dc power supply provides the dc voltage to multiturn 5 kΩ potentiometers which permit the selection of voltage levels to sandwich the impulse peak. This circuit is designed for an oscilloscope having a 1 MΩ input impedance. A mercury-wetted relay provides the noiseless switching necessary for the level-line generation.

Because of gradual drifts in the oscilloscope circuitry stability which can cause a trace to slightly drift about the screen over periods of a few tens of seconds, it is important that all three traces be acquired as quickly as possible. Using a storage oscilloscope in the "normal" mode it is usually possible to do this within 5 to 10 s using the circuit

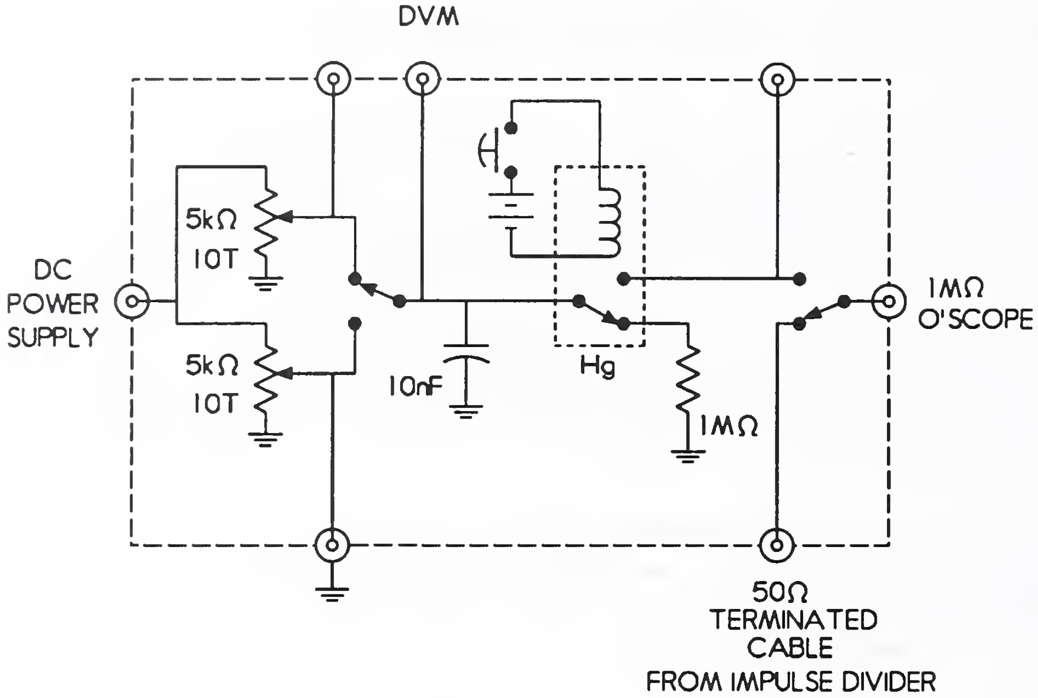

Figure 41. Circuit Diagram of Pulse-Level Line Generator. The circuit shows a switch at the input to the oscilloscope to permit measurement of the impulse voltage from the precision divider or the pulsed level lines. The digital voltmeter (DVM) used to measure the dc levels must be removed immediately before the trace acquisition if it affects the measurements by introducing significant noise on the level lines.

of Figure 41. The digital voltmeter (DVM) used to measure the dc levels must be removed immediately before the trace acquisition if it affects the measurements by introducing significant noise on the level lines.

As a check, this pulse-level-line method has been used to measure the height of a standard voltage step maintained by the Electricity Division of NIST [95]. It was a simple matter to measure the $5\,V$ step to well within 0.1% of its calibrated value (±0.02%). This method has also been successfully used with digital oscilloscopes. In using digital oscilloscopes, the three separate traces are obtained and stored as quickly as possible. The traces are then transferred to a computer and appropriately smoothed. The peak value can then be adjusted according to the values of the level lines. Such a method does not rely on the absolute calibration of the digital oscilloscope.

4.4 Conclusions

The techniques described in this report enable greater precision in high voltage impulse measurements. Improvements in the photodetector linearity made possible with the methods described here lead to more accurate determination of voltage with the Kerr measurement system. The techniques described here maximize linearity through optimal selection of the photodetector supply voltage and incident light intensity. The Pulse Level Line (PLL) technique gives greater precision in peak voltages measured with impulse voltage dividers; the method reduces oscilloscope measurement uncertainties to 0.1% or less. Although wide-bandwidth digital recorders in principle have vertical resolutions of about 0.1%, their resolution for fast transient measurements is much less due to digitization noise and the PLL method gives better resolution with analog oscilloscopes.

Improvements in pulse measurements that yield greater precision allow better measurement and equipment test standards to be developed to ensure and improve product quality. Additionally, the improved measurement techniques benefit basic insulation research, where more accurate knowledge of the voltage applied to the materials under study is important for evaluation of the physical mechanisms involved in the aging and breakdown processes. The end result is better electrical power equipment reliability.

4. REFERENCES

[1] M. Misakian, J. M. Silva, and R. S. Baishiki, "Measurements of Power Frequency Magnetic Fields Away From Power Lines," a report of the IEEE A.C. Fields Working Group. Submitted to the IEEE Transactions on Power Delivery.

[2] M. Misakian and W. T. Kaune, "An Optimum Experimental Design For In Vitro Studies Using ELF Magnetic Fields," submitted to Biolectromagnetics.

[3] V. P. Korobkova, Yu. A. Morozov, M. D. Stolarov, Yu. A. Yakub, "Influence of the Electric Field in 500 and 750 kV Switchyards on Maintenance Staff and Means For Its Protection," CIGRE Paper 23-06, 1972, Paris, France.

[4] L. B. Young, Power Over People, Oxford University Press, New York (1973).

[5] "Study in the USSR of Medical Effects of Electric Fields on Electric Power Systems," Translated from Russian by G. G. Knickerbocker, Special Publication No. 10, 78 CHO1020-7-PWR, IEEE Power Engineering Society, The Institute of Electrical and Electronics Engineers, Inc., New York (1975).

[6] ANSI/IEEE Std 644-1987 (Revision of ANSI/IEEE Std 644-1979). IEEE Standard Procedures for Measurement of Power Frequency Electric and Magnetic Fields from AC Power Lines, The Institute of Electrical and Electronics Engineers, Inc., New York (1987).

[7] M. Silva, N. Hummon, D. Rutter and C. Hooper, "Power Frequency Magnetic Fields in the Home," IEEE Transactions on Power Delivery, Vol. 4, pp. 465–477 (January, 1989).

[8] P. M. Fulcomer, "NBS Ambient Magnetic Field Meter for Measurement and Analysis of Low-level Power Frequency Magnetic Fields in Air," National Institute of Standards and Technology Report NBSIR 86–3330, prepared for Department of Energy (1985).

[9] W. Kaune, R. G. Stevens, N. J. Callahan, R. K. Severson, and D. B. Thomas, "Residential Magnetic and Electric Fields," Bioelectromagnetics, Vol. **8**, pp. 315–335 (1987).

[10] EPRI Electric and Magnetic Field Digital Exposure System Manuals, EPRI Report EN-6518, Vols. **1** and **2**, October 1989. Exposure meters with air core probes have also been developed.

[11] A. Hine, Magnetic Compasses and Magnetometers, (University of Toronto Press, Ontario, 1968) p. 51ff.

[12] See D. I. Gordon and R. E. Brown, "Recent Advances in Fluxgate Magnetometry," IEEE Trans. on Magnetics, Vol. **MAG-8**, pp. 76–82 (1972) and references therein.

[13] P. Beirsdorfer and E. J. Clothiaux, "High-frequency magnetic measurements using small inductive probes," Am. J. Phys., Vol. **51**, pp. 1031–1036 (1983).

[14] F. R. Kotter and M. Misakian, "AC Transmission Line Field Measurements," NBS report prepared for U.S. Department of Energy, Report No. HCP/T-6010/E1 (1977). Available from NTIS, Springfield, VA 22161.

[15] J. A. Stratten, Electromagnetic Theory (McGraw-Hill Book Company, New York, 1941) p. 258.

[16] C. Heck, Magnetic Materials and Their Applications, (Crane, Russak & Company, New York, 1974) pp. 67–70.

[17] P. Robert, Electrical and Magnetic Properties of Materials, (Artech House, Norwood, MA, 1988) p. 263ff.

[18] Reference 16, pp. 57–59.

[19] R. M. Bozorth, Ferromagnetism, D. Van Nostrand, New York (1951).

[20] Electrostatic and Electromagnetic Effects of Transmission Lines Working Group Paper, "Measurement of Electric and Magnetic Fields from Alternating Current Power Lines," IEEE Trans. Power Appar. and Systems, Vol. **PAS-97** (July/August, 1978), pp. 1104–1114.

[21] B. R. McLeod, A. A. Pilla, and W. Sampsel, "Electromagnetic fields induced by Helmholtz aiding coils inside saline-filled boundaries, Biolectromagnetics, Vol. **4**, pp. 357–370 (1983).

[22] D. Krause, private communication.

[23] M. M. Cohen, S. Schwartz, A. Kunska, J. Satish, and A. Hamburger, "The effect of tissue culture agar on chromosome breakage, sister-chromatid exchanges and clonogenicity in human cells," Mutation Research, Vol. **208**, pp. 201–205 (1988).

[24] J. K. Olthoff, R. J. Van Brunt, and I. Sauers, "Electron-Energy Dependence of the S_2F_{10} Mass Spectrum," J. Phys. D: Appl. Phys., Vol. **22**, pp. 1399–1401 (1989).

[25] I. Sauers, M. C. Siddagangappa, G. Harman, R. J. Van Brunt, and J. T. Herron, "Production and Stability of S_2F_{10} in SF_6 Corona Discharges," *Proc. Sixth Int'l. Symp. on High Voltage Engineering*, New Orleans (1989).

[26] J. T. Herron and R. J. Van Brunt, "Zonal Model for Corona Discharge-Induced Oxidation of SF_6 in $SF_6/O_2/H_2O$ Gas Mixtures," Proc. 9th Int'l Symp. on Plasma Chemistry, Pugnochiuso, Italy (1989).

[27] J. K. Olthoff, R. J. Van Brunt, J. T. Herron, I. Sauers, and G. Harman, "Catalytic Decomposition of S_2F_{10} and Its Implications on S_2F_{10} Production and Detection from SF_6-Insulated Equipment," *Conference Record for the 1990 IEEE Int'l Symp. on Elec. Insul.*, Toronto, June 1990 (in press).

[28] G. D. Griffin, M. G. Nolan, I. Sauers, K. Kurka, M. D. Morris, and P. C. Votaw, "Cytotoxic Activity of Disulfur Decafluoride (S_2F_{10}), A Decomposition Product of Electrically-Stressed SF_6," In Vitro, Vol. **25**, pp. 673–675 (1989).

[29] F. Y. Chu, I. Sauers, and G. D. Griffin, "A Review of the Formation of S_2F_{10} in Gas Insulated Equipment," *Conference Record of the 1988 IEEE Int'l Symp. on Elect. Insul.*, Cambridge, pp. 131–134 (1988).

[30] American Conference of Governmental and Industrial Hygienists, 5th Ed. (Am. Conf. Govt. & Indus Hyg. Assoc., Cincinnati, 1986).

[31] R. J. Van Brunt, "Production Rates for Oxyfluorides SOF_2, SO_2F_2, and SOF_4 in SF_6 Corona Discharges," J. Res. Nat. Bur. Stand.. Vol. **90**, pp. 229–253 (1985).

[32] W. Becher and J. Massonne, "Contribution to the Study of the Decomposition of SF_6 in Electrical Arcs and Sparks," ETZ-A, Vol. **91**, pp. 605–610 (1970).

[33] B. Bartakova, J. Krump, and V. Vosahlik,"Effect of Electrical Partial Discharge in SF_6," Electroteck. Obzor. (Prague), Vol. **67**, pp. 230–233 (1978).

[34] I. Sauers, P. C. Votaw, and G. D. Griffin, "Production of S_2F_{10} by Spark Discharges," *Proc. 9th Int'l Conf. on Gas Discharges and Their Applications*, Venice, pp. 592–594 (1988).

[35] I. Sauers, P. C. Votaw, and G. D. Griffin, "Production of S_2F_{10} in Sparked SF_6," J. Phys. D: Appl. Phys., Vol. **21**, pp. 1236–1238 (1988).

[36] J. A. J. Pettinga, "Full Scale High Current Model Tests on Busbar Constructions for GIS," Proc. of the CIGRE Symposium on High Current in Power Systems, pp. 506–511 (1985).

[37] F. J. J. G. Janssen, "Measurements at Sub-ppm Level of Sulfur-Fluoride Compounds Resulting From the Decomposition of SF_6 by Arc Discharges," Kema Sci. Tech. Reports, Vol. **2**, pp. 9–18 (1984).

[38] M. Farber, S. P. Cooper, and M. Khazei, "Mass Spectrometric Determination of S_2F_{10} Resulting from High-Voltage Arcing of SF_6," J. Phys. D: Appl. Phys., Vol. 22, pp. 233–234 (1989).

[39] I. Sauers, P. C. Votaw, G. D. Griffin, K. Kurka, and C. E. Easterly, *Conference Record of the 1988 IEEE Int'l Symp. on Elec. Insul.*, Cambridge, pp. 112–115 (1988). Pure S_2F_{10} was synthesized in a high-temperature reactor containing sulfur and fluorine by Dr. Darryl DesMarteau, Clemson University, Clemson, SC, USA. The identity of the sample was determined by IR absorption spectroscopy.

[40] V. H. Dibeler and R. M. Reese, "Selected Positive and Negative Ions in the Mass Spectra of Monohalomethanes," J. Res. Nat. Bur. of Stand., Vol. **54**, pp. 127–134 (1955).

[41] A. Cornu and R. Massot, *Compilation of Mass Spectral Data*, 2nd Edition, (Heyden and Sons, NY, 1975) p. 77A.

[42] B. Cohen, and A. G. MacDiarmid, Inorgan. Chem., Vol. **1**, pp. 754–756 (1962).

[43] R. E. Honig, J. Chem. Phys., Vol. **16**, pp. 105–112 (1948).

[44] B. P. Pullen, and J. A. D. Stockdale, Int'l J. Mass Spec. and Ion Phys., Vol. **19**, pp. 35–42 (1976).

[45] W. E. Reynolds, V. A. Bacon, J. C. Bridges, T. C. Coburn, B. Halpern, J. Lederberg, E. C. Levinthal, E. Steed, and R. B. Tucker, Anal. Chem., Vol. **42**, pp. 1122–1129 (1970).

[46] R. Gilbert, J. Castonguay, and A. Theoret, J. Appl. Poly. Sci., Vol. **24**, pp. 125–133 (1979).

[47] J. M. Hanrahan and A. R. Patterson, "Adsorption-Desorption Gas Chromatographic Infrared Determination of Trace Sulfur Decafluoride in Sulfur Hexafluoride," J. Chromat., Vol. **193**, pp. 265–275 (1980).

[48] Certain commercial materials are identified here in order to adequately specify the experimental procedure. In no case does this identification imply recommendation or endorsement by the National Institute of Standards and Technology, nor does it imply that the material is necessarily the best available for the purpose.

[49] R. J. Van Brunt and I. Sauers, "Gas-Phase Hydrolysis of SOF_2 and SOF_4," J. Chem. Phys., Vol. **85**, pp. 4377–4380 (1986).

[50] J. T. Herron, "A Critical Review of the Chemical Kinetics of SF_4, SF_5, and SF_2F_{10} in the Gas Phase," Int'l J. Chem. Kinet., Vol. **19**, pp. 129–142 (1987).

[51] W. R. Trost and R. L. McIntosh, "The Kinetics of the Thermal Decomposition of Disulfur Decafluoride," Can. J. Chem., Vol. **29**, pp. 508–525 (1952).

[52] *Gmelin Handbuch der Anorganischen Chemie*, (Springer Berlin, 1978), Bd. 2, p. 199.

[53] W. C. Gardinar, *Rates and Mechanisms of Chemical Reactions*, (W. A. Benjamin, Menlo Park, 1972) pp. 181–183.

[54] Each cylinder was flushed with SF_4 and evacuated before the preparation of the samples to remove as much surface moisture as possible.

[55] R. J. Van Brunt and M. C. Siddagangappa, "Identification of Corona Discharge-Induced SF_6 Oxidation Mechanisms Using $SF_6/^{18}O_2/H_2^{16}O$ and $SF_6/^{16}O_2/H_2^{18}O$ Gas Mixtures," Plasma Chem. Plasma Proc., Vol. **8**, pp. 207–223 (1988).

[56] R. J. Van Brunt, L. W. Sieck, I. Sauers, and M. C. Siddagangappa, "Transfer of F^- in the Reaction of SF_6^- with SOF_4: Implications for SOF_4 Production in Corona Discharge," Plasma Chem. Plasma Proc., Vol. **8**, pp. 225–246 (1988).

[57] M. C. Siddagangappa and R. J. Van Brunt, "Decomposition Products from Corona in SF_6/N_2 and SF_6/O_2 Mixtures," *Proc. 8th Int'l Conf. on Gas Discharges and Their Applications*, Leeds University Press, pp. 247–250 (1985),

[58] R. J. Van Brunt, T. C. Lazo, and W. E. Anderson, "Production Rates for Discharge Generated SOF_2, SO_2F_2, and SO_2 in SF_6 and SF_6/H_2O Mixtures," in *Gaseous Dielectric IV - Proc. Fourth Int'l Symp. on Gaseous Dielectrics*, ed. by L. G. Christophorou and M. O. Pace, Pergamon, New York, pp. 276–285 (1984).

[59] M. C. Siddagangappa, R. J. Van Brunt, and A. V. Phelps, "Influence of Oxygen on the Decomposition Rate of SF_6 in Corona," *Conference Record for the 1986 IEEE Int'l Symp. on Elec. Insul.*, IEEE, New York, pp. 225–229 (1986).

[60] R. Hergli, J. Casanovas, A. Derdouri, R. Grob, and J. Mathieu, "Study of the Decomposition of SF_6 in the Presence of Water, Subjected to Gamma Irradiation or Corona Discharges," IEEE Trans. Elec. Insul., Vol. **23**, p. 451 (1988).

[61] R. J. Van Brunt, J. T. Herron, and C. Fenimore, "Corona-Induced Decomposition of Gaseous Dielectrics," *Gaseous Dielectrics V - Proc. 5th Int'l Symp. on Gaseous Dielectrics*, Pergamon, New York, pp. 163–173 (1987).

[62] A. V. Phelps and R. J. Van Brunt, "Electron-Transport, Ionization, Attachment, and Dissociation Coefficients in SF_6 and Its Mixtures," J. Appl. Phys., Vol. **64**, pp. 4269–4277 (1988).

[63] L. Niemeyer, *Proc. 8th Int'l Conf. on Gas Discharges and Their Applications*, Leeds University Press, London, pp. 223–226 (1985).

[64] D. B. Ogle and G. A. Woolsey, J. Phys. D: Appl. Phys., Vol. **20**, p. 453 (1987).

[65] I. Sauers, J. L. Adcock, L. G. Christophorou, and H. W. Ellis, "Gas-Phase Hydrolysis of SF_4," J. Chem. Phys., Vol. **83**, p. 2618 (1985).

[66] I. C. Plumb and K. R. Ryan, "Gas-Phase Reactions of SF_2 SF_4, and SOF with $O(^3P)$: Their Significance in Plasma Processing," Plasma Chem. Plasma Proc., Vol. **6**, p. 247 (1986).

[67] L. W. Sieck and R. J. Van Brunt, "Rate Constants for F^- Transfer from SF_6^- to Fluorinated Gases and SO_2. Temperature Dependence and Implications for Electrical Discharges in SF_6," J. Phys. Chem., Vol. **92**, pp. 708–713 (1988).

[68] I. Sauers, "Sensitive Detection of Byproducts formed in Electrically Discharged SF_6," IEEE Trans. Elec. Insul., Vol. **EI-21**, p. 105 (1986).

[69] K. R. Ryan, Plasma Chem. Plasma Proc. (in press).

[70] K. R. Ryan and I. C. Plumb, "Gas-Phase Combination Reactions of SF_4 with F in Plasmas of SF_6," Plasma Chem. Plasma Proc., Vol. **8**, p. 281 (1988).

[71] W. Braun, J. T. Herron, and D. K. Kahaner, Int'l J. Chem. Kinetics, Vol. **20**, p. 51 (1988).

[72] R. d'Agustino and D. L. Flamn, "Plasma Etching of Si and SiO_2 in $SF_6 - O_2$ Mixtures," J. Appl. Phys., Vol. **52**, p. 162 (1981).

[73] R. Kattan, A. Denat, and O. Lesaint, "Generation, Growth, and Collapse of Vapor Bubbles in Hydrocarbon Liquids Under a High Divergent Electric Field," J. Appl. Phys., Vol. **66**, pp. 4062–4066 (1989).

[74] S. M. Korobejnikov and E. F. Yanshin, "Model of Prebreakdown Processes in Liquids Under Pulse Voltage," Ninth International Conf. on Conduction and Breakdown in Dielectric Liquids, Salford, UK, pp. 398–402, (1987).

[75] E. F. Kelley, M. Nehmadi, R. E. Hebner, M. O. Pace, A. L. Wintenberg, T. V. Blalock, and J. V. Foust, "Measurement of Partial Discharges in Hexane Under DC Voltages," IEEE Trans. Elec. Insul., Vol. **EI-24**, pp. 1109–1119, (1989).

[76] M. O. Pace, A. L. Wintenberg, T. V. Blalock, E. F. Kelley, G. J. FitzPatrick, C. Fenimore, and H. Yamashita, "Pressure Effects on Partial Discharges in Hexane Under DC Voltage," IEEE 1989 Annual Report on the Conference on Electrical Insulation and Dielectric Phenomena, pp. 87–92, (1989).

[77] E. F. Kelley, "An Image-Preserving Optical Delay for High-Speed Photography," Conference Record of the 42nd Annual Conference of the Society for Imaging Science and Technology (formerly SPSE), Boston, pp. 293-296 (May 1989). A more complete treatment is anticipated as E. F. Kelley and M. Nehmadi, "High-Speed Photography of Random Phenomena Using an Image-Preserving Optical Delay," Rev. Sci. Inst., in press.

[78] James R. Melcher, *Continuum Electromechanics*, (MIT Press, Cambridge, Mass., 1981) Sec. 8.9, Fig. 9.9.3b, p. 8.32.

[79] I. Alexeff, T. V. Blalock, A. L. Wittenberg, J. V. Foust and M. O. Pace, "Multipulse Prebreakdown Phenomena in Liquid Dielectrics," Proc. 14th IEEE International Conf. on Plasma Science, p. 55, (1987).

[80] P. K. Watson, W. G. Chadband, and W. Y. Mak, "Bubble Growth Following a Localized Electrical Discharge and its Relationship to the Breakdown of Triggered Spark Gaps in Liquids," IEEE Trans. Elec. Insul., Vol. **EI-20**, pp. 275–280 (1985).

[81] P. K. Watson, "EHD Instabilities in the Breakdown of Point-Plane Gaps in Insulating Liquids," IEEE 1981 Annual Report Conference on Electrical Insulation and Dielectric Phenomena, pp. 370–376 (1981).

[82] R. E. Tobazéon, "Streamers in liquids," in *The Liquid State and Its Electrical Properties*. Editors E. E. Kunhardt, L. G. Christophorou and L. H. Luessen, New York: Plenum Press, 1988, pp. 465–501.

[83] R. E. Hebner, "Measurement of electrical breakdown in liquids," in *The Liquid State and Its Electrical Properties*. Editors E. E. Kunhardt, L. G. Christophorou and L. H. Luessen, New York: Plenum Press, 1988, pp. 519–537.

[84] J. L. Blue, "B2DE - A program for solving systems of nonlinear elliptic partial differential equations in two dimensions," Nat. Bureau of Standards Report NBSIR-3411, 1986.

[85] H. Yamashita and H. Amano, "Prebreakdown phenomena in hydrocarbon liquids," IEEE Trans. Elect. Ins., Vol. **EI-23**, pp. 739–750 (1988).

[86] P. K. Watson and W. G. Chadband, "The dynamics of pre-breakdown cavities in viscous silicon fluids in negative point gaps," IEEE Trans. Elect. Ins., Vol. **EI-23**, pp. 729–738 (1988).

[87] E. F. Kelley and R. E. Hebner, "The electric field distribution associated prebreakdown phenomena in nitrobenzene," J. Appl. Phys., Vol. **52**, pp. 191–195 (1981).

[88] W. Feller, *Introduction to Probability Theory and Its Applications V1*, 1968, New York: Wiley, pp. 212–230.

[89] R. E. Hebner, E. F. Kelley, E. O. Forster and G. J. Fitzpatrick, "Observation of prebreakdown and breakdown phenomena in liquid hydrocarbons," J. Electrostatics, Vol. **12**, pp. 265–283 (1982).

[90] B. Whitney, H. Asgeirsson, "Lightning Detection and Storm Severity Display System," Paper No. **90** WM 059–6 PRWD, IEEE PES Winter Meeting, February 4–9, 1990, Atlanta, GA (1990).

[91] S. A. Boggs, F. Y. Chu, N. Fujimoto, *Gas-Insulated Substations. Technology and Practice.* Chapter 6. Experience, Pergamon Press (1986).

[92] S. Eckhouse, M. Markovits, and M. Coleman, "Pulse Quality Optimization on a Linear Induction Accelerator Test Stand," Digest of the 7th IEEE Pulse Power Conference, June 11–14, 1989, Monterey, CA (1989).

[93] G. L. Clark, "Dielectric Properties of Nitrobenzene in the Region of Anomolous Dispersion," J. Chem. Phys., Vol. **25**, pp. 215–219 (1956).

[94] R. E. Hebner, Jr., "Calibration of Kerr Systems Used to Measure High Voltage Pulses," NBSIR 75–774, U.S. Department of Commerce, 48 pages (Aug. 1975).

[95] H. K. Shoenwetter, D. R. Flach, T. M. Souders, and B. A. Bell, "A Precision Programmable Step Generator for Use in Automated Test Systems," NBS Technical Note 1230, U.S. Department of Commerce, 98 pages (Dec. 1986).

NIST-114A
(REV. 3-89)

U.S. DEPARTMENT OF COMMERCE
NATIONAL INSTITUTE OF STANDARDS AND TECHNOLOGY

BIBLIOGRAPHIC DATA SHEET

1. PUBLICATION OR REPORT NUMBER
NISTIR 4339

2. PERFORMING ORGANIZATION REPORT NUMBER

3. PUBLICATION DATE
JUNE 1990

4. TITLE AND SUBTITLE

Research for Electric Energy Systems - An Annual Report

5. AUTHOR(S)

Richard J. Van Brunt, Editor

6. PERFORMING ORGANIZATION (IF JOINT OR OTHER THAN NIST, SEE INSTRUCTIONS)

U.S. DEPARTMENT OF COMMERCE
NATIONAL INSTITUTE OF STANDARDS AND TECHNOLOGY
GAITHERSBURG, MD 20899

7. CONTRACT/GRANT NUMBER

8. TYPE OF REPORT AND PERIOD COVERED

9. SPONSORING ORGANIZATION NAME AND COMPLETE ADDRESS (STREET, CITY, STATE, ZIP)

Department of Energy
Division of Electric Energy Systems
1000 Independence Avenue, SW
Washington, DC 20585

10. SUPPLEMENTARY NOTES

☐ DOCUMENT DESCRIBES A COMPUTER PROGRAM; SF-185, FIPS SOFTWARE SUMMARY, IS ATTACHED.

11. ABSTRACT (A 200-WORD OR LESS FACTUAL SUMMARY OF MOST SIGNIFICANT INFORMATION. IF DOCUMENT INCLUDES A SIGNIFICANT BIBLIOGRAPHY OR LITERATURE SURVEY, MENTION IT HERE.)

This report documents the technical progress in four investigations which make up the project "Support of Research Projects for Electrical Energy Systems," funded by the U.S. Department of Energy and performed by the Electricity Division of the National Institute of Standards and Technology (NIST). Specifically these investigations include: 1) an evaluation and critique of techniques for measuring ambient magnetic fields in support of epidemiological and in vitro studies of biological field effects; 2) development of techniques for detecting the toxic gas S_2F_{10} in SF_6 and measuring its production rate from corona discharges in SF_6; 3) optical and electrical measurements of prebreakdown partial-discharge phenomena in dielectric liquids; and 4) development of improved electro-optical methods for measurement and characterization of fast, transient high-voltage impulses. The work discussed in this report is part of an ongoing research activity at NIST.

12. KEY WORDS (6 TO 12 ENTRIES; ALPHABETICAL ORDER; CAPITALIZE ONLY PROPER NAMES; AND SEPARATE KEY WORDS BY SEMICOLONS)

corona discharges; dielectric liquids; electrical insulation; electro-optical measurements; fast transients; gaseous dielectrics; magnetic-field measurements; magnetic field probes; partial discharges; prebreakdown phenomena; S_2F_{10}; sulfur hexafluoride

13. AVAILABILITY

☒ UNLIMITED
☐ FOR OFFICIAL DISTRIBUTION. DO NOT RELEASE TO NATIONAL TECHNICAL INFORMATION SERVICE (NTIS).
☐ ORDER FROM SUPERINTENDENT OF DOCUMENTS, U.S. GOVERNMENT PRINTING OFFICE, WASHINGTON, DC 20402.
☒ ORDER FROM NATIONAL TECHNICAL INFORMATION SERVICE (NTIS), SPRINGFIELD, VA 22161.

14. NUMBER OF PRINTED PAGES
91

15. PRICE
A05

ELECTRONIC FORM